University of Wollongong

Research Online

University of Wollongong Thesis Collection 1954-2016

University of Wollongong Thesis Collections

2005

Investigation of vortex dynamics of (T1,Pb)(Sr,Ba)2Ca2Cu3Oy and an alternative method for determination of the lock-in angle in twinned superconductors

Shokat Keshavarzi

University of Wollongong

Follow this and additional works at: https://ro.uow.edu.au/theses

University of Wollongong

Copyright Warning

You may print or download ONE copy of this document for the purpose of your own research or study. The University does not authorise you to copy, communicate or otherwise make available electronically to any other person any copyright material contained on this site.

You are reminded of the following: This work is copyright. Apart from any use permitted under the Copyright Act 1968, no part of this work may be reproduced by any process, nor may any other exclusive right be exercised, without the permission of the author. Copyright owners are entitled to take legal action against persons who infringe their copyright. A reproduction of material that is protected by copyright may be a copyright infringement. A court may impose penalties and award damages in relation to offences and infringements relating to copyright material. Higher penalties may apply, and higher damages may be awarded, for offences and infringements involving the conversion of material into digital or electronic form.

Unless otherwise indicated, the views expressed in this thesis are those of the author and do not necessarily represent the views of the University of Wollongong.

Recommended Citation

Keshavarzi, Shokat, Investigation of vortex dynamics of (T1,Pb)(Sr,Ba)2Ca2Cu3Oy and an alternative method for determination of the lock-in angle in twinned superconductors, PhD thesis, Institute for Superconducting and Electronic Materials, University of Wollongong, 2005. http://ro.uow.edu.au/theses/300

Research Online is the open access institutional repository for the University of Wollongong. For further information contact the UOW Library: research-pubs@uow.edu.au

INVESTIGATION OF VORTEX DYNAMICS OF $(Tl,Pb)(Sr,Ba)_2Ca_2Cu_3O_y$ AND AN ALTERNATIVE METHOD FOR DETERMINATION OF THE LOCK-IN ANGLE IN TWINNED SUPERCONDUCTORS

A thesis submitted in fulfilment of the requirements
for the award of the degree

Doctor of Philosophy

from the

University of Wollongong

by

SHOKAT KESHAVARZI, M.Sc., Physics.

INSTITUTE FOR SUPERCONDUCTING AND ELECTRONIC MATERIALS

&

FACULTY OF ENGINEERING

2005

Acknowledgment

I would like to express my most sincere appreciation and gratitude to my supervisors, Prof. S. X. Dou, Dr. J. Horvat and Dr. M. J. Qin, for their academic guidance and encouragement within the period of my study.

I would like to thank Dr. Alexey V. Pan, Dr. M. Ionescu, Dr. X. L. Wang, Prof. P. Munroe and Dr. T. M. Silver for their useful discussions and suggestions.

Thanks are also due to Dr. X. L. Wang and Dr. Xin Yao, Shanghai Jiao Tong University, China, for providing the single crystals.

Special thanks are given to Dr. T. M. Silver for providing help in proofreading my papers and this thesis.

Many thanks go to all my friends and all the members at the Institute for Superconducting & Electronic Materials, and all the technicians at the Faculty of Engineering. Thanks also go to Ms. B. M. Allen for her help in administrative matters.

Finally, I wish to thank my husband Mr. S. A. Fatemi and my beautiful daughter, Saba, for their support and patience in my daily long absences from home.

Table of content

Abstract:

Magnetic moment measurements performed on a single crystal sample of $(Tl,Pb)(Sr,Ba)_2Ca_2Cu_3O_y$ reveal an increase in magnetic moment at intermediate and high fields over a wide temperature range below H_{c2}. Magnetic hysteresis (*m-H*) loops were taken at different constant temperatures using either a MPMS-5T SQUID magnetometer or a PPMS-9T magnetometer and within the temperature range $0.1< T/T_c < 0.85$. The main objective of this thesis was to study the mechanisms involved in the emergence of the peak in the magnetic hysteresis loops in the two samples (the so-called *peak effect*). It is argued that point disorder in the form of oxygen vacancies or substitution is responsible for pinning at intermediate and high field. Vortex dynamics at fields below and above the peak in hysteresis loops for the sample are shown to be well explained by a quasi-lattice Bragg Glass state and elastic Collective and Plastic Vortex Creep, respectively. For this purpose, relaxation in magnetic moment was measured at different fields and temperatures. Following that, the field and temperature dependence of the normalized relaxation rate, *S*, the effective activation energy, *U*, and the critical exponent μ were calculated. Analysis of all these quantities in the material led to the conclusion that the transition from a highly ordered vortex lattice (Abrikosov lattice) to an amorphous vortex lattice is responsible for the rise in magnetic moment at low fields, and subsequently the crossover from this amorphous state to a plastically deformed vortex lattice, which is assisted by dislocations, is responsible for the suppression of the peak effect in *m-H* loops.

The investigation of flux pinning by twin planes has attracted considerable attention, since naturally-formed twin planes occur regularly in Y123 crystals. One of the characteristic properties of vortex pinning by twin planes is a cusp-like dependence of the

irreversibility field (H_{irr}) on the angle φ between the twin plane and the magnetic field. The cusp appears around φ = 0°, within the angular range φ_L. The angle φ_L is called the lock-in angle. The measurement of the angular dependence of H_{irr} has been the principal method used to study the locking of magnetic vortices by twin planes and the determination of φ_L. However, due to the high irreversibility field of 123 systems, such measurements could be conducted only at high temperatures, close to T_c, at which the irreversibility field is subject to a high degree of uncertainty. Further, H_{irr} is defined by an arbitrary value of magnetization, at which the ascending and descending branches of the magnetic hysteresis loop, or the zero-field cooled and field-cooled branches of the temperature dependence of the magnetization, are seen to merge. Because of this, it is highly desirable to develop an alternative method for obtaining φ_L, which relies on universal physical principles instead of arbitrary definitions. Such a method is presented in this work. This method was developed for an off-stoichiometric Sm123 single crystal. Due to the global behaviour of the hysteresis loop at high temperatures close to T_c for twinned superconductors this method is not restricted to this compound and can be used for all twinned superconductors irrespective of their microstructures or oxygen contents. This method for determining the lock-in angle φ_L for pinning of the vortices on extended defects, i.e. twin planes here, was employed without any pre-assumed criterion for defining φ_L. Appropriate scaling of the hysteresis loops for different angles close to the *c*-axis led to a clear discrimination between the two vortex dynamics regimes. From this scaling the lock-in angle was determined to be 6° ± 0.1°, which means that the uncertainty in determining the lock-in angle using this method is considerably less than with other existing methods.

List of Figures

List of Tables

CHAPTER ONE: INTRODUCTION

1. Introduction

One of the greatest revolutions in superconductivity was caused by the discovery of high-temperature superconductivity by Bednorz and Müller in 1986 [1]. The original explanation of this group of superconductors was proposed by Abrikosov [2] who introduced the mean-field version of the phase diagram in 1957. The phase diagram comprises a Meissner phase characterized by complete flux expulsion at low magnetic fields $H < H_{c1}$, and separated from the mixed phase at higher fields $H > H_{c1}$, where magnetic flux penetrates the superconductor in form of flux lines (vortices) containing one flux quantum $\Phi_0=hc/2e=2.07\times10^{-7}$ Oe cm^2, where h is Planck's constant, c is the speed of light and e is the elementary charge. Every flux line has a normal core with the radius on the order of ξ, the coherence length. The vortex current circulates within an area of radius ~λ, the penetration depth. With increasing field, the flux lines are squeezed together, so that on approaching the upper critical field, H_{c2}, the cores will begin to overlap and the entire bulk turn into the normal conducting state. However, the real situation in high temperature superconductors (HTS) which include static and dynamics disorder is more complicated, and further considerations associated with these types of disorder must be taken into account, so that vortex dynamics in the mixed phase would not be as simple as in the mean-field version. High temperature-range performance, the smallness of the coherence length (in compare to low T_c superconductors) and high anisotropy caused by the layered structure of the high temperature superconductors reinforces the complexity of the problem. In this case, the vortex lattice might have different behavior depending on the relative strength of the different kinds of disorders involved. Investigation of vortex dynamics of layered HTS such as Bi- and Tl-based and RE123 system (RE: rare earth) superconductors has been an attractive and interesting topic within the last two decades. Among them the Tl1223 and

Sm123 families with low anisotropy could be promising candidates in applications. However to optimize the characteristics of these materials, a profound knowledge of the mechanisms involved in the superconductivity and establishing the phase diagram of the material are essential prerequisites.

Since the discovery of superconductivity in general, intensive efforts have been devoted to the phenomenological aspect of superconductors, which have led to the invention of entities like the "superconducting electron" in the London theory [3,4], the "line vortex" and "pancake vortex" in the theory of Abrikosov [2] and his successors and the "Cooper pair" in the Bardeen, Cooper and Schrieffer (BCS) theory [5].

The analysis and interpretation of superconductivity begins with the London theory [3,4], which is based on the two-fluid model of Gorter and Casimir (1934). This model assumes that the electron liquid in a superconductor is comprised of two fluids: the "normal" and the "superconducting". Whereas the properties of the "normal" group are identical to those of the electron system in a normal metal, the "superconducting" group is responsible for the anomalous properties. According to this model, with decreasing temperature the "superconducting" fraction grows, while the density of the "normal" electrons decreases and finally vanishes at zero temperature. On approaching $T=T_c$ from zero temperature, the "superconducting" part decreases until it vanishes at $T=T_c$. The London equations provided a correct description of the anomalous diamagnetism of superconductors in a weak external field and of zero resistance to a dc current.

In 1950, Vitaly Ginzburg and Lev Landau [6] proposed a *phenomenological* theory, which is an alternative to the London theory. Ginzburg-Landau (GL) theory correctly describes the phase transition in zero field, but unlike the London theory, which is purely classical, it uses quantum mechanics to predict the effect of a magnetic field. Two

assumptions form the basis of GL theory. First, that the behavior of the superconducting electrons may be described by an "effective wave function" Ψ , which has the significance that $|\Psi|^2$ is equal to the density of superconducting electrons. It is then assumed that the free energy of the superconducting state differs from that of the normal state by an amount which can be written as a power series in $|\Psi|^2$ (section 2.1.3). Having applied the GL theory to superconducting alloys, Abrikosov developed a theory of the so-called type-II superconductors (1957).

In response to the application of an external current density j, which leads to the Lorentz force $\mathbf{F}_L=\boldsymbol{J}\times\mathbf{H}/c$, flux lines start moving. In a pinning-free system, this force can be counteracted by a viscous force. As a result of the motion under the dissipative viscous force, a finite electric field is built up, which is not a desired circumstance for dissipation-free current density flow in the superconductor. However, any static disorder affecting the superconducting order parameter can prevent the motion of vortices.

In addition to static disorder (e.g. quenched disorder) dynamical disorder (e.g. thermal fluctuations) might affect the vortex system, but in different way. Both of the above disorders have rigorous consequences for both the *H-T* phase diagram and the dynamical properties of the vortex system. Whereas quenched disorder can remove the translational long-range order of the Abrikosov vortex lattice, thermal disorder, through thermal fluctuations, can lead to melting of the vortex-solid system to the vortex-liquid phase.

The last kind of disorder that can complicate the mean-field version of the *H-T* phase diagram is quantum disorder. Since there are many similarities between thermal fluctuations and quantum fluctuations, the classical formalism of thermal fluctuations can be replaced by their quantum counterparts to obtain quantum disorder formalism.

Ultimately in a real superconductor, depending on the relative strength of the different kinds of disorders and in particular at very low temperatures, all types of disorder might have a contribution in determining the dynamics of the vortex system.

In HTSs, there are always interplays between quenched and thermal disorders. Since the analytical solution of a many-particle system with the above-mentioned disorders is an intricate task, finding some approximate solutions in limiting cases is desirable. For example, in GL theory, a superconductor is assumed to be a continuum and the free energy of the system is expanded about the critical temperature T_c, with the implication that this theory is valid only at temperatures close to T_c. In a HTS, as thermal fluctuations tend to weaken quenched disorder strength, one faces a system that comprises weak pinning sites so that they can be treated as a perturbation, which is the scenario in the melting theory [7]. However, in contrast to the melting theory, the vortex glass theory [8] considers the quenched disorder from the beginning. The vortex glass theory is based on establishment of infinite energy barriers due to collective effects, which leads to a zero linear flux flow resistance when J is vanishingly small. This collective effect-based theory was developed by Feigel'man et al. [9], and the collective creep theory is a consequence. From elasticity theory, they derived a power-law formalism for the effective activation energy when the electric current decays logarithmically in time. This activation energy stems from the competition between the elastic vortex-vortex interaction and the pinning potential.

One of features which has attracted great attention within last decade is the anomalous increase in magnetic moment of a superconductor with rising applied field, which is known as the anomalous "Peak Effect", or in some reports it is called the "Fishtail" due to its particular shape. Extensive efforts have been allocated to find the underlying mechanism in this interesting behavior, since it is an advantage for a

superconductor to show stronger pinning properties and consequently have higher critical current density. The more we know about the mechanisms involved in the appearance of this phenomenon, the more critical current density we can achieve by optimizing the superconductor under application. For example, it has now been well established that point disorder such as oxygen vacancies and substitutions can play a crucial role in enhancement of magnetic moment. On the other hand, the influence of the disorder depends on a few other factors, such as the strength of the magnetic field and the temperature. The condition is more or less the same for other types of disorder such as extended disorder. Then it is worthwhile to investigate the effect of the presence of static disorder and to find to which extent it can govern the vortex dynamics in a superconducting phase diagram. For example, one of the recent theories which seem to be the most convincing explanation of the peak effect is the theory of "order-disorder transition"[10-12]. According to this theory, for a field just above the lower critical field, the vortex lattice forms a highly ordered ensemble, and in this case the static disorder plays no significant role, while the elastic energy due to the interaction between vortices has the leading role. This phase, which is close to the ideal Abrikosov vortex lattice, is usually called the Bragg Glass, Disentangled or quasi lattice phase. With increasing field the role of static disorder becomes more significant so that within a certain range of field and temperature the pinning energy becomes comparable with the elastic energy of the vortex lattice, and further promotion of the field yields a transition from the Bragg Glass to the amorphous Vortex Glass which lacks long range order and sometime is also known as the Entangled phase. The extent of the Bragg Glass phase has been shown to depend on the quality and quantity of the static disorder[13]. Within the context of the vortex solid phase, attempts have been made to examine not only the so called order-disorder transition as the possible source of the peak effect, but also other type

of changes in the vortex lattice, such as the plastic shear deformations which were introduced by Geshkenbein et al.[14], are investigated in order to present a complete picture of the vortex phase diagram within the accessible range of applied field.

Additional new features are associated with the layered structure of the majority of HTSs. Whereas MgB_2, Tl(1223) and Y(123) compounds can be described within a continuum anisotropic model, presenting a discrete description of strongly layered Bi- and (other composition) Tl-based compounds, is inevitable. In this case, the discrete model of Lawrence and Doniach [15] is usually referred to. For a highly layered superconductor, a large portion of the *H-T* phase diagram is occupied by quasi-2D superconductivity, and the rectilinear vortex may have to be replaced by the two-dimensional entities called pancake vortices. This inherent anisotropy gives rise to new effects, such as the appearance of intrinsic pinning and creep and of dimensional crossover.

The vortex dynamics of the oxide superconductor Tl(2212) and Tl(2223) family and $YBa_2Cu_3O_y$ (whether twinned or twin-free) have been intensively investigated by many researchers since their discoveries. The interest in these materials is mainly due to their high critical temperature, higher than 90K (which is above the boiling point of liquid nitrogen), and their good superconducting properties.

However, among the Tl-based family of superconductors less attention has been paid to Tl(1223) compound, which could be a potential candidate not only for applications but also for vortex dynamics studies. Whereas the Tl(2212) and Tl(2223) family suffer from the high anisotropy factor (due to having a double Tl-O layer) this last member with low anisotropy has the merit of being suitable for investigations aimed at finding the possible mechanisms of pinning and the influence of applied magnetic field or temperature on those mechanisms. From this investigation, we can also compare the material's potential in

regard to its application in industry with other low anisotropic material such as the RE(123) systems, where RE: Y, Sm, Nd.

Further an alternative technique for determining the so-called lock-in angle in a twinned superconductor is developed. This technique is not necessarily limited to a specific twinned superconductor and could be potentially used for all twinned members of the RE(123) family, which is the best host of twin planes. Determination of the lock-in angle is usually conducted via angular dependence of the irreversibility field[16]. For a twinned superconductor, when the applied magnetic field is made more parallel to the c-axis, at a certain angle (about a few degrees) vortices start deforming, and the pinning strength is enhanced. The enhancement of the pinning appears as a cusp in the H_{irr} as a function of angle within a few degrees from the c-axis. However, this method is accompanied with some uncertainty; firstly, the determination of the irreversibility field is criterion dependent, and secondly, since the twin planes are mostly effective pinning sites at high temperatures, extraction of the irreversibility field at those temperatures, which involve severe thermal noise, is not an easy task. Therefore, in the new method, which does not rely on an arbitrary criterion and doesn't deal with the noisy part of the data is highly useful. Furthermore, this method could be more fundamental from the physics point of view.

The present thesis is outlined as follows:

Chapter Two: The second chapter constitutes the foundation upon which the discussions and the conclusion are built without losing the unification of concepts and interrelationships; following the London model and phenomenological theory of GL, it contains a review of the critical state model and of vortex system behavior. The London and GL equation are the bases for understanding the fundamental characteristics of a superconductor and its behavior towards any imposed changes from applied magnetic field

and temperature. With this context the definition of the superconducting coherence length and magnetic penetration depth, which are of overwhelming significance in the whole of the thesis, are understood.

Chapter Three: In chapter three all aspects of vortex dynamics, including collective vortex pinning and creep, vortex matter in HTSs, any possible vortex solid phase transition or crossover, such as elastic to plastic shear deformations are presented.

Chapter Four: The fourth chapter is devoted to methodology of the experiments, including the sample characterization method, and the magnetic measurements (such as *dc* magnetization).

Chapter Five: Chapter Five has been allocated to the experimental results in addition to the discussion of those results, which is set in the framework of the theories presented in prior chapters.

Chapter Six: Chapter Six is ultimately allocated to the concluding remarks and future work perspective.

References:

1 J. G. Bednorz and K. A. Müller, Zs. Phys. B **64,** 189 (1986).

2 A. A. Abrikosov, Sov. Phys. JETP **5,** 1174 (1957).

3 F. London and H. London, Proc. Roy. Soc. (London) **A149,** 71 (1935).

4 F. London and H. London, Physica **2,** 341 (1935).

5 J. Bardeen, L. N. Cooper, and J. R. Schrieffer, Phys. Rev. **108,** 1175 (1957).

6 V. L. Ginzburg and L. D. Landau, Zh. Eksp.Teor. Fiz **20,** 1064 (1950).

7 D. R. Nelson, Phys. Rev. Lett. **60,** 1973 (1988).

8 M. P. Fisher, Phys. Rev. Lett. **62,** 415 (1989).

9 M. V. Feigel'man, V. B. Geshkenbein, and A. I. Larkin, Phys. Rev. Lett. **63,** 2303 (1989).

10 T. Giamarchi and P. Le Doussal, Phys. Rev. Lett **72,** 1530 (1994).

11 D. Ertas and D. R. Nelson, Physica C **272,** 79 (1996).

12 V. M. Vinokur, B. Khaykovich, E. Zeldov, M. Konczykowaski, R. A. Doyle, and P. H. Kes, Physica C **295,** 209 (1998).

13 H. Küpfer, T. Wolf, R. Meier-Himer, and A. A. Zhukov, Physica C **332,** 80 (2000).

14 V. B. Geshkenbein, A. I. Larkin, M. V. Feigel'man, and V. M. Vinokur, Physica C **162,** 239 (1989).

15 W. E. Lawrence and S. Doniach, Kyoto, 1971 (Proceedings of the 12th International Conference on Low Temperature Physics, Academic Press of Japan, Kyoto), p. 361.

16 H. Küpfer, A. A. Zhukov, A. Will, W. Jahn, R. Meier-Himer, T. Wolf, V. I. Voronkova, M. Kläser, and K. Saito, Phys. Rev. B **54,** 644 (1996).

CHAPTER TWO: AN OVERVIEW OF THE FUNDAMENTALS OF SUPERCONDUCTIVITY

The goal of this chapter is to obtain some historical perspective on the evolution of models and theories, which make up the infrastructure of the physics of superconductors.

2.1 Elementary Phenomenological Theories

In the first part of this section the London model, which successfully describes the electrodynamics of superconductors, is presented. The second part of this section is devoted to Pippard theory followed by a presentation of the Ginzburg-Landau theory.

2.1.1 The London Model[1,2]

This model assumes that all free electrons of a superconductor with density n are divided into two groups: superconducting electrons of density n_s and normal electrons of density n_n, so that $n = n_s + n_n$, and $n_s(T_c) = 0$ and $n_s(T = 0) = n$. The classical equation of motion (Newton's second law) for superconducting electrons in an electric field **E** is

$$n_s m \frac{d}{dt} v = n_s e\mathbf{E} \Rightarrow \mathbf{E} = \frac{d}{dt}(m\boldsymbol{J}_s/n_s e^2); \qquad (2\text{-}1)$$

where $\boldsymbol{J}_s$, $\boldsymbol{v}$, m and e are the supercurrent density, superfluid velocity, electron mass and charge, respectively. In the above equation the relation $\boldsymbol{J}_s = n_s e \boldsymbol{v}$ between the supercurrent density and the superfluid velocity has been used. This equation is known as the *first London equation*. It turns out that in a steady state, that is, when $d\boldsymbol{J}_s/dt = 0$, there is no electric field inside the superconductor.

Now if we denote the true microscopic magnetic field at a given point of a superconductor by **H(r)**, taking into account the kinetic energy density of the superconducting electrons, the free energy of the superconductor takes the following form

$$\mathcal{F}_{sH} = \mathcal{F}_{s0} + \frac{1}{8\pi} \int [\, \mathbf{H}^2 + \lambda_L{}^2 (\nabla \times \mathbf{H})^2 \,] \, dV \qquad (2\text{-}2)$$

where

$$\lambda_L = \left(\frac{mc^2}{4\pi n_s e^2} \right)^{1/2}, \qquad (2\text{-}3)$$

while $\mathcal{F}_{s0}$ is the zero-magnetic-field free energy of the superconductor. The integration is carried out over the entire volume of the superconductor. The second and third terms in (2-2) are the energy associated with the magnetic field $\mathbf{H}(\mathbf{r})$ and the kinetic energy density of the supercurrent. In order to find the identity of $\mathbf{H}(\mathbf{r})$ corresponding to the minimum value of $\mathcal{F}_{sH}$, the variational method is used. After some mathematical manipulation the following equation, which is known as *the second London equation* is obtained

$$\mathbf{H} + \lambda_L{}^2 \nabla \times \nabla \times \mathbf{H} = 0. \qquad (2\text{-}4)$$

Using Maxwell's equation ($\nabla \times \mathbf{H} = 4\pi \boldsymbol{J}_s/c$) and the London gauge ($\nabla . \mathbf{A} = 0$), from the above equation we then obtain

$$\boldsymbol{J}_s = -\frac{c}{4\pi\lambda_L{}^2} \mathbf{A}. \qquad (2\text{-}5)$$

Now if we assume a superconductor settles in a semi-space ($x > 0$), so that its surface coincides with the plane $x = 0$, using equation (2-4) with application of an external magnetic field (H_o) along the z-axis, we encounter a one-dimensional problem, the solution of which, subject to the boundary conditions $H(0) = H_o$ and $H(\infty) = 0$, leads to

$$H = H_o \, e^{-x/\lambda_L}. \qquad (2\text{-}6)$$

It follows from this equation that the magnetic field exponentially falls off with increasing distance from the surface of the superconductor, and the characteristic length defined by (2-3) is the extent to which the magnetic field penetrates the superconductor and is called the

3 0009 03371622 1

London magnetic field penetration depth. The London penetration depth, λ_L, is strongly temperature dependent and can be described to a reasonable approximation by:

$$\lambda_L(T) = \frac{\lambda_L(0)}{[1-(T/T_c)^4]^{1/2}}. \qquad (2\text{-}7)$$

Substituting $T = T_c$ shows that $\lambda_L = \infty$ and it turns out that no flux is excluded at T_c. However, below T_c, λ_L decreases quickly, so that the exclusion of flux from the bulk of the sample occurs. This phenomenon is the *Meissner effect*. It must be noted that the above calculation is valid for weak applied fields. In higher fields it may become energetically more favourable to destroy superconductivity in some parts of the sample and to allow the flux lines to penetrate.

The London equations can be generalized to quantum electrodynamics. Since the constituents of the supercurrent are pairs of electrons (Cooper pairs), which are bosons, they obey the Bose-Einstein statistics. Therefore all pairs occupy the same energy level, or the same quantum state, i.e., they form a condensate. The wave function of a particle in the condensate can be written as $\Psi(\mathbf{r}) = (n_s/2)^{1/2} e^{i\varphi(\mathbf{r})}$, where φ is the phase of the wave function. In this case the momentum of a Cooper pair of mass $2m$ and charge $2e$ moving in a magnetic field is expressed by

$$\hbar \nabla\varphi = 2m\, v_s + \frac{2e}{c}\mathbf{A} \qquad (2\text{-}8)$$

where $\hbar$ is Planck's constant divided by 2π. Using the expression $J_s = n_s e\, v_s$ the generalized second London equation is obtained as

$$\mathbf{J}_s = \frac{c}{4\pi\lambda^2}\left(\frac{\Phi_o}{2\pi}\nabla\varphi - \mathbf{A}\right) \qquad (2\text{-}9)$$

where $\Phi_o = \pi\hbar c/e = 2.07 \times 10^{-7}$ Oe cm^2 is the magnetic flux quantum. Using relation (2-9), it is shown that magnetic flux in superconductors is a quantized quantity[3].

2.1.2 Pippard theory[4]

The London equations (2-1) and (2-4) have been shown to lead to an exponential decay in the penetration layer [equation (2-6)] with the characteristic penetration length λ_L defined in (2-3). It is unlikely that this length is position-independent near an external surface. In the superconducting state, the velocities of the two electrons (1) and (2) are correlated if the distance between them doesn't exceed a certain range, which is called the coherence length, and for pure metals this is expressed by ξ_o. Pippard's experiment (1953) shows deviation from strictly exponential decay and therefore departure from the London equations. The source of this problem is the locality of equation (2-5); i.e. the current at a point is related to the field at the same point or in other words, when the velocities have a negligible variation over a distance ~ξ_o. The derived London equation in the previous section holds only if $\lambda_L \gg \xi_o$. Therefore in simple (nontransition) metals in which this condition is unsatisfied, the London equation is not applicable, while equation (2-5) is definitely applicable in weak fields for transition metals and intermetallic compounds of the Nb_3Sn and V_3Ga type with large effective mass [5]. A. B. Pippard introduced the superconductor coherence length ξ by generalizing the London equation (2-5) to a nonlocal relationship [6]

$$\mathbf{J}(\mathbf{r}) = -\frac{3c}{16\pi^2 \xi_o \lambda_p^2(T)} \int d\mathbf{r}' \frac{(\mathbf{r}-\mathbf{r}')[(\mathbf{r}-\mathbf{r}').\mathbf{A}(\mathbf{r}')]}{|\mathbf{r}-\mathbf{r}'|^4} e^{-|\mathbf{r}-\mathbf{r}'|/\xi} \qquad (2\text{-}10)$$

In the presence of electron scattering with mean free path l, the Pippard penetration depth $\lambda_p = (\lambda_L^2 \xi_o / \xi)^{1/2}$ exceeds the London penetration depth λ_L of a pure material with coherence length ξ_0, since the effective coherence length ξ is increased by scattering, $\xi^{-1} \approx$

$\xi_0^{-1} + l^{-1}$ [6]. In the limit of small $\xi \ll \lambda_p$, equation (2-10) reduces to the local relation (2-5). In Fourier space Pippard's equation (2-10) reads as

$$\mathbf{J}(\boldsymbol{k}) = -c / 4\pi\, Q_p(k)\, \mathbf{A}(\boldsymbol{k})$$

where $Q_p(k) = \lambda_p^{-2}\, h(k\xi)$,

$$h(x) = \frac{3}{2x^3}\,[(1+x^2)\,\mathrm{atan}(x) - x], \quad h(0) = 1. \qquad (2\text{-}11)$$

The Pippard theory is useful mainly for superconductors with a small GL parameter κ (next section).

2.1.3 The Ginzburg-Landau theory[7]

The non-local version of the London equation, that is the Pippard equation, is restricted to the case where the applied magnetic field is small and can be treated as a perturbation, and the superconducting electron density $n_s(r)$ is nearly constant in space. Furthermore, this theory doesn't take into account quantum effects. The first quantum phenomenological theory of superconductivity is the Ginzburg-Landau (GL) theory. This theory is based on the second-order phase transitions developed by Landau [8,9], in which Landau introduced the important concept of the order parameter. In GL theory the order parameter is a complex quantity, namely the wave function $\Psi(\mathbf{r}) = |\Psi|e^{i\varphi(r)}$. The absolute value $|\Psi(\mathbf{r})|$ is connected with the local density of superconducting electrons, $|\Psi(\mathbf{r})|^2 = n_s(\mathbf{r})$. The phase φ of the order parameter is needed for describing supercurrents. The free-energy density f_{GL} is then expanded in powers of Ψ, assuming that Ψ and ∇Ψ are small (near T_c)

$$f_{GL}=f_n+\alpha(T)|\Psi|^2+\frac{\beta}{2}|\Psi|^4+\frac{1}{4m}|(\frac{\hbar}{i}\nabla-\frac{2e}{c}\mathbf{A})\Psi|^2+\frac{H^2}{8\pi}-\frac{\mathbf{H}.\mathbf{H}_o}{4\pi}. \qquad (2\text{-}12)$$

Here $\alpha(T) = \alpha_o (T- T_c)$ and β are coefficients of the GL theory; α_o and β are constants > 0 and f_n is the free energy density of a superconductor in the normal state. $\mathbf{H}_o$ is the external magnetic field. The last but one term represents the magnetic energy density, where **H** is the exact microscopic field at a given point of the superconductor. The fourth term is the kinetic energy density of the superconducting electrons with charge $2e$ moving in the field with vector potential **A**. The minimum energy is found from a variational method leading to a pair of coupled differential equations for $\Psi(\mathbf{r})$ and the vector potential $\mathbf{A}(\mathbf{r})$. Following a standard variational procedure outlined in any textbook, the two Ginzburg-Landau differential equations are found to be

$$\alpha(T)|\Psi|+\beta|\Psi|^2\Psi+\frac{1}{4m}(\frac{\hbar}{i}\nabla+\frac{2e}{c}\mathbf{A})^2\Psi=0 \qquad (2\text{-}13)$$

and

$$\mathbf{J}_s=\frac{e\hbar}{2mi}(\Psi^*\nabla\Psi-\Psi\nabla\Psi^*)-\frac{2e^2}{mc}|\Psi|^2\mathbf{A}. \qquad (2\text{-}14)$$

Equation (2-13) has the form of the Schrödinger equation with the eigenvalue $-\alpha$, with the term $\beta|\Psi|^2\Psi$ acting like a repulsive potential. Equation (2-14) represents the quantum-mechanical description of a superconducting current J_s. The two characteristic lengths, the coherence length $\xi(T) = \hbar/(4m|\alpha|)^{1/2}$ and the penetration depth $\lambda(T) = (mc^2/4\pi\, n_s e^2)^{1/2} = (mc^2\beta/8\pi e^2|\alpha|)^{1/2}$ can be derived from the GL theory. It is useful to introduce the GL parameter $\kappa = \lambda(T) / \xi(T)$. The parameter is very important; at $\kappa < 1/\sqrt{2}$ the wall energy of a normal-superconducting interface is positive and the superconductor is *type–I,* and at $\kappa > 1/\sqrt{2}$ the wall energy is negative and the superconductor is *type-II* [10].

The importance of the GL theory is that this theory can be derived from the more fundamental BCS microscopic theory, which will be described briefly in the next section.

2.1.4 The BCS theory

A systematic theory of superconductivity which explained the nature of this phenomenon was formulated in 1957 by Bardeen, Cooper, and Schrieffer (BCS theory) [11]. The theory begins with a net attractive interaction between electrons in the neighbourhood of the Fermi surface. Although the direct electrostatic interaction is repulsive, it is possible for the ionic motion to overscreen the Coulomb interaction, leading to a net attraction. Pairs of electrons can behave very differently from single electrons, which are fermions and must obey the Pauli exclusion principle. The pairs of electrons, known as *Cooper pair*, act more like bosons, which can condense into the same energy level. The electron pairs have a slightly lower energy and leave an *energy gap* above them on the order of 0.001 eV, which inhibits the kinds of collision interactions that lead to ordinary resistivity.

The microscopic BCS theory (in the Green function formulation of Gorkov) for weak magnetic fields yields a similar nonlocal relation $\boldsymbol{J}(\boldsymbol{k}) = -c/4\pi\ Q(k)\ \mathbf{A}(\boldsymbol{k})$ to that suggested by Pippard, replacing the Pippard kernel $Q_p(k)$ by the BCS kernel [12,13]

$$Q_{BCS}(k) = \lambda^{-2}(T) \sum_{n=1}^{\infty} \frac{h[k\xi_\kappa/(2n+1)]}{1.0518(2n+1)^3}. \qquad (2\text{-}15)$$

Here h(x) is defined in equation (2-11), $\lambda(T) = Q_{BCS}(0)^{-1/2} \approx \lambda(0)(1 - T^4 / T_c^4)^{-1/2}$ is the temperature dependent magnetic penetration depth, and $\xi_\kappa = \hbar v_F / (2\pi k_B T) \approx 0.844\lambda(T)\, T_c / (\kappa T)$ (where v_F is the Fermi velocity, κ is the GL parameter). The range of the BCS Gorkov kernel is of the order of the BCS coherence length $\xi_o = \hbar v_F / (\pi\Delta_o)$, where Δ_o is the BCS energy gap at $T = 0$.

Nonlocality in either the Pippard or the BCS equation leads to a magnetic field function H(r) for an isolated vortex line which is no longer monotonic as compared with the London field (discussed in the following section), but exhibits a field reversal with a negative minimum at large distances $r \gg \lambda_p$ from the vortex core. This field reversal of the vortex field is partly responsible for the attractive interaction between flux lines at large distances, which has been observed in clean Niobium at temperatures not too close to T_c and which follows from BCS theory at $T < T_c$ for pure superconductors with the GL parameter κ close to $1/\sqrt{2}$.

A few major equilibrium predictions of BCS theory are as follow[14]

1. In zero magnetic field, the superconducting transition temperature is given by

$$k_B T_c = 1.13\ \hbar\omega e^{-1/N_o V_o}, \qquad (2\text{-}16)$$

where N_0 is the density of electronic levels for a single spin population at the Fermi level, V_0 is the simplified attractive effective interaction between electrons near the Fermi energy and $\hbar\omega$ is the difference in electronic energies.

2. The zero-temperature energy gap is predicted to be:

$$\Delta_0 = 2\hbar\omega e^{-1/N_o V_o}. \qquad (2\text{-}17)$$

The ratio of (2-17) to (2-16) gives a fundamental formula independent of the phenomenological parameters ω and V_0:

$$\frac{\Delta_o}{k_B T_c} = 1.76,$$

From this theory the temperature dependence of the energy gap near the critical temperature (in zero field) is determined to be:

$$\frac{\Delta(T)}{\Delta_o} = 1.74\left(1-\frac{T}{T_c}\right)^{1/2}, \quad T \approx T_c, \qquad (2\text{-}18)$$

which means that on approaching the critical transition temperature the energy gap shrinks.

3. The temperature dependence of the critical field according to this theory at low temperature is $H_c(T)/H_c(0) \approx 1 - 1.06(T/T_c)^2$, while near T_c it is $H_c(T)/H_c(0) = 1.74$ [1-(T/T_c)] which shows deviation from the empirical law:

$$\frac{H_c(T)}{H_c(0)} \approx 1-\left(\frac{T}{T_c}\right)^2. \qquad (2\text{-}19)$$

The departure in most low temperature conventional superconductors is small, but for strong-coupling superconductors like lead and mercury it is considerable.

4. At $T_c(H_o=0)$ the elementary BCS theory predicts a discontinuity in the specific heat which is independent of V_o and N_o

$$\frac{c_s - c_n}{c_n}\Big|_{T_c} = 1.43. \qquad (2\text{-}20)$$

2.2 The vortex system and its behaviour

According to their magnetic properties, superconductors are divided into type-I superconductors and type-II superconductors. In type-I superconductors an external magnetic field cannot penetrate into the bulk of the sample deeper than λ_L without destroying the superconductivity. Type-II superconductors (which are the main target of this work), of which high-T_c superconductors (HTS) are prominent members, preserve superconductivity over a range of fields H in the range $H_{c1} < H < H_{c2}$. At the lower critical field H_{c1}, which is mainly determined by the London penetration depth λ, the first magnetic flux starts to enter the bulk of the superconductor. The field does not penetrate the bulk in a homogenous way but as quantised vortex filaments. Every vortex has a normal core with a radius of order ξ, the coherence length. The direction of the supercurrent circulating around

the normal core is such that the direction of the magnetic field generated by it coincides with that of the external field and is parallel to the normal core. The vortex current circulates within an area of radius ~ λ_L, the London penetration depth [Figure (2.1)]. This current screens the bulk of the sample from the field in the vortex core. The screening is similar to the Meissner current, however, in a vortex the screening is from an internal field rather than an external field (as in the Meissner effect). Superconductivity is maintained up to the so-called upper critical field H_{c2} which is determined by the coherence length ξ via $H_{c2}=\Phi_o/2\pi\xi^2$. The state of the superconductor in between H_{c1} and H_{c2} is referred to as the mixed state because of spatial in-homogeneity in the local magnetic induction and the local density of superconducting electrons.

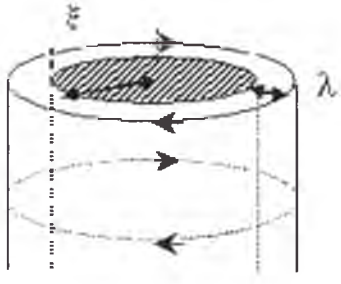

Figure 2- 1 A superconducting vortex comprises a normal core with radius ξ, the coherence length, and a screening current which circulates within an area of radius ~ λ_L, the penetration depth.

Vortices in superconductors have a well-defined mutual interaction. The range of the interaction is the magnetic penetration length, which is set by the material parameters. Since the density of vortices is determined by the applied magnetic field, one can continuously tune the system from weakly to strongly interacting. In order to investigate the vortex dynamics of a superconductor we need to know first about the configuration and the electromagnetic behaviour of the individual vortices as the constituents of a vortex lattice. This state can well describe a dilute vortex system at a very low field range.

Subsequently, on increasing the density of vortices through increasing the applied magnetic field, the electromagnetic interaction between them is established. For a bulk sample in an applied magnetic field H_o, vortices form continuous lines that thread the system parallel to the applied field. In a pure sample at low temperatures and magnetic fields, these vortex lines crystallize into a solid state known as the *Abrikosov vortex line lattice*. The original prediction of Abrikosov (via solving the GL equations) was a square vortex lattice system as the most favourable energy state[15]. However, subsequent solutions of the GL equations for magnetic fields just below the upper critical field $H_{c2}(T)$, have convincingly shown that a periodic triangular array of vortex lines has the lowest free energy of all possible periodic solutions, and hence is the most stable configuration[10,16]. Decoration experiments which utilize small iron particles to make the vortices visible through an electron microscope have provided the best confirmation of the triangular arrangement[17].

2.2.1 Field of a single vortex line

Because of the rigours of the GL solution, these equations can only be solved numerically for arbitrary values of κ. In the extreme type-II limit $\kappa \gg 1$ (where the hard core has an insignificant contribution to the energy), however, the solution becomes simple. If the external magnetic field is very small, there will be few vortex lines, i.e. the vortex lines will be well separated. In this case the interaction between the vortex lines can be neglected. This approximation reduces the problem to a study of the properties of a single vortex line. The line energy can then be calculated via the (2-2) expression, for a distance $\lambda \gg \xi$,

$$\mathcal{F} = \frac{1}{8\pi} \int_{\infty}^{r} [\mathbf{H}^2 + \lambda_L^2 (\nabla \times \mathbf{H})^2] \, dV \qquad (2\text{-}21)$$

where the integration is carried out over all space outside the core ($r > \xi$). For a pure superconductor, the penetration depth λ has the London value, $\lambda = \lambda_L$. However, for a superconducting alloy, with $\lambda \gg \xi$, equation (2-21) still applies, but λ is proportional to the square root of the impurity concentration, $l^{1/2}$ [5]. Using the same variational method employed above for equation (2-21) we reach

$$\mathbf{H}^2 + \lambda_L^2 (\nabla \times \mathbf{H})^2 = 0 \qquad |r| > \xi . \qquad (2\text{-}22)$$

When taking the vortex singularity into account in the interior of the core, the above equation is replaced by

$$\mathbf{H} + \lambda_L^2 \nabla \times \nabla \times \mathbf{H} = \Phi_o \, \delta(\mathbf{r}) \, \mathbf{e}_v . \qquad (2\text{-}23)$$

The δ-function represents the effect of the core, regarded as a line source. The two-dimensional equation (2-23) has the solution[18]

$$H = \frac{\Phi_o}{2\pi\lambda_L^2} K_o (r / \lambda_L) \qquad (2\text{-}24)$$

where K_o is the MacDonald function, and takes the asymptotic form[10]

$$H \approx \frac{\Phi_o}{2\pi\lambda_L^2} \ln(\lambda_L / r) \qquad \text{for } \xi \ll r \ll \lambda \qquad (2\text{-}25)$$

$$H \approx \frac{\Phi_o}{2\pi\lambda_L^2} \sqrt{\frac{\pi\lambda_L}{2r}} e^{-r/\lambda} \qquad \text{for } r \gg \lambda . \qquad (2\text{-}26)$$

As the (2-25) expression doesn't hold in the vicinity of the normal core (of radius ~ ξ) the field at the centre of the vortex can be obtained to logarithmic accuracy by setting a cut-off at $r = \xi$:

$$H(0) = \frac{\Phi_0}{2\pi\lambda_L^2} \ln \kappa. \qquad (2\text{-}27)$$

A more accurate solution of the GL equations by numerical integration [18] leads to

$$H(0) = \frac{\Phi_0}{2\pi\lambda_L^2} (\ln \kappa - 0.18). \qquad (2\text{-}28)$$

However this correction is not essential since all the calculations are carried out on the assumption that $\kappa \gg 1$. Using expression (2-27) the line energy, or free energy per unit length of a vortex, e_l is obtained as[3]

$$e_l = (\frac{\Phi_0}{4\pi\lambda_L})^2 \ln \kappa = \varepsilon_0 \ln \kappa. \qquad (2\text{-}29)$$

A vortex can generally be considered as an elastic string which, compared with a point-like object, exhibits additional interesting static and dynamic properties due to its one-dimensional extended nature.

2.2.2 Interaction between vortices

In a superconductor with $\kappa \gg 1$, when the distance between two vortices becomes less than λ, the core of one vortex moves into the area where the supercurrents of the other vortex circulate. This overlap leads to a repulsive force between the two parallel vortices. This force is exerted only on the vortex core. This force can be derived from the free energy density of a system comprising two vortices located at $\mathbf{r}_1$ and $\mathbf{r}_2$. Applying equation (2-23) for a two-vortex system we obtain[3,19]

$$\mathbf{H} + \lambda_L^2 \nabla\times\nabla\times \mathbf{H} = \Phi_0 [\, \delta(\mathbf{r} - \mathbf{r}_1) + \delta(\mathbf{r} - \mathbf{r}_2)\,]\mathbf{e}_v. \qquad (2\text{-}30)$$

Here $\mathbf{H}$ is the total magnetic field generated by the two vortices. From the London free energy density (2-2) we have

$$\mathcal{F} = \frac{1}{8\pi} \int [\mathbf{H}^2 + \lambda_L^2 (\nabla \times \mathbf{H})^2] \, dV. \qquad (2\text{-}31)$$

After a series of mathematical manipulations

$$\mathcal{F} = \frac{\Phi_o}{8\pi} [H (\mathbf{r}_1) + H (\mathbf{r}_2)]. \qquad (2\text{-}32)$$

Here $H(\mathbf{r}_i)$ (i =1, 2) is the resultant field due to both vortices at the centre of the vortex located at $\mathbf{r}_i$. Therefore if the self-energy and mutual energy are separated, (2-32) becomes

$$\mathcal{F} = 2e_l + \frac{\Phi_o}{8\pi} 2 H_{12}(r) \qquad r = |\mathbf{r}_1 - \mathbf{r}_2| \qquad (2\text{-}33)$$

where e_l is the energy of an isolated vortex defined by (2-29), and $H_{12} = H_1(\mathbf{r}_2) = H_2(\mathbf{r}_1)$. The second term is the interaction energy F_{12}

$$F_{12} = \frac{\Phi_o}{4\pi} H_1 (r_2) = \frac{\Phi^2_o}{8\pi^2 \lambda_L^2} K_o (r / \lambda_L) = 2\varepsilon_o K_o (r / \lambda_L) . \qquad (2\text{-}34)$$

The interaction force associated with this energy is the derivative of F_{12}. For example, using the Maxwell equation: $\nabla \times \mathbf{H} = 4 \pi \mathbf{J} / c$, the force on vortex 2 in the x direction is

$$f_{2x} = -\frac{\partial F_{12}}{\partial x_2} = -\frac{\Phi_o}{4\pi} \frac{\partial H_1(\mathbf{r}_2)}{\partial x_2} = \frac{\Phi_o}{c} J_{1y}(r_2) \qquad (2\text{-}35)$$

where $J_{1y}(r_2)$ is the current density induced by the first vortex at the centre of the second vortex. The generalized expression for the interaction force for an arbitrary array is

$$\mathbf{f} = \boldsymbol{J} \times \frac{\Phi_o}{c} \qquad (2\text{-}36)$$

where $\boldsymbol{J}$ denotes the total supercurrent density due to all other vortices (even including any net transport current) at the location of the core of the vortex in question. The lowest energy configuration that leads to static equilibrium is associated with a triangular vortex array. However, even the triangular array will feel a force transverse to any transport current, so that the vortices will move unless *pinned* in place by in-homogeneities in the medium. The

vortex lattice is subject to a force density per unit volume (*Lorentz force*) that can be obtain from (2-36)

$$\mathbf{F} = \boldsymbol{J} \times \mathrm{n}\,\frac{\Phi_o}{c} = \boldsymbol{J} \times \frac{\mathbf{H}}{c} \qquad (2\text{-}37)$$

where $H = \Phi_o n$ is the average field at a given location, that is, the average magnetic induction in a region of dimensions much larger than the distance between the vortices; n is the average vortex density.

2.2.3 Magnetization Curves

Using the calculations in the previous sections for a single vortex and the interaction energy between two vortices, the magnetization curves can be studied from the first flux penetration up to the vicinity of H_{c2}. Now the Gibbs function per unit volume can be expressed as[6,19]

$$\mathrm{G} = n\varepsilon_l + \sum_{ij} F_{ij} - \frac{HH_o}{4\pi} \qquad (2\text{-}38)$$

where the first term represents the individual energies of the vortex lines. The second term describes the repulsive interactions between vortices, which are given by (2-34). Finally, the last term gives the effect of the applied field H_o that determines the density of vortices. From the minimization of the above equation for different applied fields three regimes between H_{c1} and H_{c2} can be distinguished [6]:

1. Very near H_{c1}, $\Phi_o / H \gg \lambda^2$, and vortices are separated by more than λ. In this case, only a few nearest neighbours are important. In this case, from summation of the mutual interaction energy of (nearest) vortices (equation (2-34)) and minimizing the Gibbs energy relative to the induction for a triangular array of vortices we would end up with[6]

$$H = \frac{2\Phi_o}{\sqrt{3}\lambda^2}\left\{\ln\left[\frac{3\Phi_o}{4\pi\lambda^2(H_o - H_{c1})}\right]\right\}^{-2} . \qquad (2\text{-}39)$$

2. For moderate values of H such that $\Phi_o / \lambda^2 \leq H \ll \Phi_o / \xi^2$, which corresponds to $H_{c1} \leq H \ll H_{c2}$, many vortices are within interaction range of any given one, so that elaborate summing procedures are required. However, it is still a good approximation to neglect details of the core. Using the modified London equation (equation (2-30)) and including the interaction of many neighbours, the calculation in Fourier space of the local flux density in a plane perpendicular to the field then leads to[6]

$$H_o = H + H_{c1}\frac{\ln(H_{c1}/H)}{\ln\kappa} \qquad (2\text{-}40)$$

which is a reasonable description of the data well above H_{c1}.

3. Near H_{c2}, $\xi^2 \approx \Phi_o / H$, so that the cores are almost overlapping and the order parameter is reduced everywhere. This requires more detailed treatment of the core. The simple superposition of the two previous parts is no longer accurate, and the Abrikosov solution to the linearized GL equation at H_{c2} is a helpful approximation. The resultant magnetization from this calculation for a triangular lattice (the Abrikosov Lattice) is [6]

$$-4\pi M = \frac{H_{c2} - H}{1.16(2\kappa^2 - 1)} . \qquad (2\text{-}41)$$

For a given temperature, the magnetization vanishes at H_{c2} as a linear function of the applied magnetic field. Measurements of the slope of the magnetization vs. magnetic field close to H_{c2} enable one to determine κ. This represents one of the few direct measurements of the Ginzburg-Landau parameter $\kappa = \lambda/\xi$, which is one of the fundamental quantities that characterize a given superconductor. An important feature of (2-41) is the presence of a

factor $(2\kappa^2-1)$ in the denominator. M goes to infinity at $\kappa = 1/\sqrt{2}$, which is exactly the criterion for distinguishing type-I and type-II superconductors.

2.3 Disorder

2.3.1 Quenched Disorder

The study of quenched disorder is an unavoidable topic in superconductivity, and in particular in high-T_c superconductors. It appears that the current densities that can be sustained in high-T_c superconductors are much smaller than in conventional superconducting materials. Part of the reason for this inability - besides the smallness of their coherence lengths and large structural and electronic anisotropy- can be assigned to the lack of quenched disorder as a source of pinning centres for vortices. On the other hand, the Meissner phase in type-II superconductors in general is bounded by the lower critical field H_{c1}, which has the approximate value of a few hundred gauss. Hence most of the phase diagram is dominated by the presence of vortices. In a homogenous (defect-free) superconductor, application of even an infinitely small transport current (via the Lorentz force in equation (2-37)) leads to the dissipative motion of vortices. However, by the presence of quenched disorder (including local and correlated defects, such as inclusions, oxygen non-stoichiometry, twin boundaries, screw dislocations, artificial columnar defects, stacking faults, etc.), properties of superconducting materials are altered locally. A vortex encompassing or adjacent to such disorder in the material has its energy altered, and its free motion through the superconductor is inhibited. Quenched disorder therefore could be a prerequisite for obtaining the fundamental property of dissipation-free flow.

In contrast to the situation with homogenous superconductors, a finite transport current is required to set the vortices moving. The current density corresponding to the

initiation of vortex tear-off from the pinning centres is called *the critical current density*, J_c. In equilibrium, the average density of the pinning force denoted by F_p is balanced by the Lorentz force, and the critical current density then satisfies the following equation [Bean critical model (section 2.4)]

$$\frac{1}{c} J_c H = F_p \,. \qquad (2\text{-}42)$$

A few points must be borne in mind: firstly, that only an elastic vortex system can exploit the advantage of pinning centres; secondly, that not every defect can interact with vortices effectively. For example, whereas in classic superconductors with large coherence lengths, point defects are not efficient, in HTS with coherence lengths comparable to the defect size they are desirable. The pinning problem in high-T_c oxide superconductors will be discussed in Chapter 3.

One of the main consequences of introducing quenched disorder to the vortex system is the occurrence of an irreversible behaviour in the magnetization curve $M(H_o)$ when the applied magnetic field $H_o = H - 4\pi M$ is cycled (sec. 2.4).

In the following sections a few types of quenched disorder that can play a role in the observed results in chapter 5 are briefly reviewed.

Point defect

In-homogeneities or any other factor that can suppress the order parameter locally can lead to vortex pinning. For example, a void or a hole or an off-stoichiometry compound even at a single atomic site can act as a pinning site. Oxygen vacancies are good practical candidates for vortex pinning in high-temperature superconductors. Furthermore, particle doping can enhance pinning which yields growth in current density [20,21].

Twin Planes and Other Extended Defects

Twin planes are the predominant source of defects in superconductors which have orthorhombic crystal structures [22,23]. In this case, the *a* and *b* directions in the plane are not exactly equivalent. These planes are parallel to the (110) and $(1\bar{1}0)$ planes. Due to accumulation of point defects and impurities along these planes and to the depression of the order parameter, they are attractive sites for vortices. Moreover, because of its extended planar structure, the pinning acts in a coherent rather than a random way on a flux line lying in the plane, making the pinning effective. From the angular dependence of the resistivity Kwok [24,25] revealed the importance of these planes.

Among the extended defects, stacking faults are another source of pinning in high-temperature superconductors, which originate from intergrowth of other crystal phases with additional or fewer Cu-O planes per unit cell.

Screw dislocations [26] are the third well-known group of extended defects, which are aligned in the direction of growth and form in a spiral staircase environment.

Artificial Defects

A very recent technology for producing defects is the irradiation of the material with high-energy ions [27,28]. The linear tracks of damaged material then introduce strongly correlated disorder into the aligned vortex system. At low magnetic fields such that the vortex lattice parameter a_0 is much larger than the mean distance between the tracks, each vortex is individually pinned by a columnar defect.

Via melt-process melt-quench heat-treatment a high density of inclusions of off-stoichiometric second phases can be introduced into high-temperature superconductors [29].

2.3.2 Thermal Disorder

In the traditional mean-field version, the vortices in the mixed state are under the influence of only the Lorentz and pinning forces (which originate from quenched disorder). Due to the balance between these two forces for currents less than the so-called critical current density no vortex motion, and consequently, no dissipation occurs. However going beyond the mean-field picture, an alternative type of disorder that might affect the vortex system (specifically in HTS) is thermal disorder. While the former type of disorder is static, the latter one is dynamical. The inclusion of thermal fluctuations affects the dynamical behaviour of type-II superconductors in various ways. Thermal activation of vortices makes them jump over the pinning barrier even at current densities below the critical current density, leading to the well-known creep phenomenon in type-II superconductors. Creep, which is a directed snail-like motion of vortices, is a dissipative process. Following the classical ideas of Anderson [30] and Anderson and Kim [31], it is found that thermal fluctuation induces inter-valley hops of vortex segments and of vortex bundles so that the whole vortex system is driven by an external current density J to move with a finite creep velocity $v \simeq 2v_o\exp(-U_o / k_BT)\sinh[(U_o /k_BT)(J / J_o)]$, where U_o is the pinning barrier. In the limiting case where $J \rightarrow 0$ expansion of this relation leads to $v \propto J$, which shows that the system has an ohmic behaviour with a resistance $\rho(T) \propto \rho_n\exp (-U_o /k_BT)$. Depending on the relative values of U_o and T, a few different possibilities exist. If $U_o \ll k_BT$, the vortex motion is essentially unaffected by the quenched disorder and can flow freely under the action of a driving force. The resistivity ρ is then given by the flux flow resistivity $\rho \approx \rho_{ff} \simeq \rho_n (H / H_{c2})$. This flux flow (FF) behaviour is the dynamic response of the unpinned vortex liquid at high temperatures near the $H_{c2} (T)$ line. For another extreme case of $U_o \gg k_BT$ the

resistivity becomes exponentially small, $\rho(T) \simeq (\rho_{ff}/A) \exp(-U_o/k_BT)$, where $A \ll 1$. This activated behaviour is the dynamic response of the pinned vortex liquid at high temperatures near the melting line $H_m(T)$. This regime is now well known as the TAFF regime for thermally assisted flux flow [32]. This regime, which could be modelled as a very viscous liquid, crosses over to the FF regime with increased temperature.

2.4 The Bean critical state model

In an absolutely homogenous (defect-free) superconductor the vortices would start moving at an infinitely small transport current density via the Lorentz force, (2-37). In the extreme case of strong pinning where substantial vortex motion and associated electrical resistance are prevented, a finite transport current is required to set the vortices moving. The threshold current density for detaching the vortices from the pinning centres, J_c, must satisfy equation (2-42).

In this case, Bean [33,34] has established a relationship between the measured irreversible magnetization M_{irr} and the bulk supercurrent density J_c. This so-called Bean critical state model is based on two simple assumptions, namely that the supercurrent density is given by the critical current density J_c, that is, any effect due to thermal or quantum creep is ignored, and that any changes in the flux distribution are introduced at the sample surface. The specific relationship of M_{irr} and J_c depends on the sample geometry and has been extensively reviewed for different configurations by Campbell and Evetts [35]. Appendix A is a list of the geometrical factors for different configurations. For example, for the commonly used rectangular shaped samples the factor is, when the applied field is along the c-axis, $20/[a(1-a/3b)]$, where a and b are the lateral dimensions of the sample, a<b. The calculation

of this geometrical factor for an infinite slab with thickness L subjected from both sides to a parallel applied field H_o has been illustrated below.

Starting from point 1 in Figure (2-2)(a), flux penetrates from the surfaces, with a gradient $(4\pi/c)$ J given by the Maxwell's equation $\nabla \times \mathbf{H} = (4\pi/c)\mathbf{J}$. The flux fronts (at point 1) penetrate a distance $cH_o/4\pi J_c$ into the infinite slab. From electromagnetism, $H = 4\pi M + H_o$, so that the magnetization is now

$4\pi M = H - H_o = cH_o^2 / 4\pi J_c L - H_o$.

At $H_{ful} = 2\pi J_c L/c$ (called the full penetration field hereafter), the field penetrates into the centre of the sample with the profile given in Figure (2-2)(b). In this state the magnetization reaches its maximum diamagnetic value of $M = - J_c L/4c$. If the applied field is now reduced from far above H_{ful} the situation illustrated in Figure (2-2)(c) is obtained. The trapped flux inside the sample is often called "remanent" magnetization.

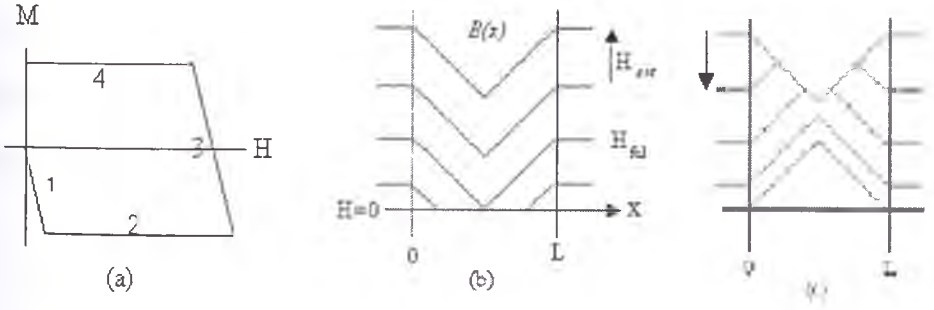

Figure 2- 2 (a) Half hysteresis loop and internal flux density profiles in a slab subjected to (b) increasing and (c) decreasing external field. H_{ful} is the maximum field that can be screened at the mid-plane (full penetration field).

2.5 Elasticity of the vortex lattice

As mentioned in section 2.3.1 only a spatially flexible vortex can exploit the advantage of a pinning site. That is, a vortex is pictured as elastic string and therefore, like every

elastic object, it has its own elasticity constant. Whereas in investigation of the vortex system as an elastic medium the starting point in the single-vortex case is the elastic string, the starting point at higher fields [when the vortex lattice parameter (a_o) is less than the penetration depth (λ)] is the elastic vortex lattice with its well-defined compression (C_{11}), shear (C_{66}), and tilt (C_{44}) properties. A perfectly rigid and periodic flux-line lattice (FLL) could not be effectively pinned by any random collection of pinning sites. This is because, for any position of the FLL relative to the material, an equal number of random pinning sites would exert an equal force in all directions, so that the average energy of the flux lines is spatially invariant. However, the paths of individual flux lines can deviate from the ideal periodic arrangement of the Abrikosov lattice to lower their energy by accommodating an optimal low-energy pinning site, but at the expense of increasing the elastic energy of the FLL by deforming it.

The flux-line distortion caused by pinning forces and by thermal fluctuation has been extensively calculated by Brandt[13] using the elasticity theory of the flux line lattice with the three modes of distortion of the triangular flux line lattice: shear, uniaxial compression and tilt as follow:

$$C_{11}(k) = \frac{H^2}{4\pi(1+k^2\lambda^2)}, \qquad C_{66} = \frac{H\,\Phi_o}{(8\pi\lambda)^2},$$

$$C_{44}(k) \approx C_{11}(k) + 2C_{66}\ln\frac{k^2}{1+k_z^2\lambda^2}. \qquad (2\text{-}43)$$

The GL theory yields an additional factor $(1 - H/H_{c2})^2$ in C_{66}, i.e., $C_{66} \propto H(H - H_{c2})^2$, and replaces λ in $C_{11}(k)$ by $\lambda' = \lambda/(1 - H/H_{c2})^{1/2}$ [36].

2.6 Irreversibility Line

A key feature not found in conventional bulk superconductors is an "irreversibility" line, where magnetic irreversibility sets in. In order for a sample to show a reversible magnetization curve the vortex lines must be able to move freely through the sample so as to come into equilibrium at every point on the magnetization curve. Conversely, whenever there is any agent in the sample that prevents the vortex lines from moving, the magnetization curve shows some irreversibility. The irreversibility line [$H_{irr}(T)$] in the H-T plane separates the finite critical current density below from the zero one above. The properties of the flux matter in real systems which possess pinning centres are determined by the relationship between four energies: the elastic energy (E_{el}) due to interaction between vortices, the pinning energy (E_{pin}) from interaction between vortices and pinning centres, the coupling energy between the superconducting Cu-O planes in cuprate superconductors, and the thermal energy (E_{th}=) k_BT [37,38]. Whereas the competition between thermal energy and pinning energy leads to the so-called depinning line, the melting line results from the competition between thermal energy and elastic energy where the shear modulus of the lattice becomes zero (section 2.5). Provided that the concentration of pinning sites is small, the lower of either the melting or the depinning line is the origin of H_{irr}. Flux lines below this line are well trapped, so that with a circulation of the magnetic hysteresis loop from zero field to a field above H_{c1} and back to zero field we would end up with a remanent magnetic moment. There are several factors that could affect the irreversibility line. In cuprate HTS, for instance, it has been shown that the line depends on the inter-plane or plane-chain separation [39]. Thermodynamic fluctuations also play a

striking role in the determination of this line [40]. In addition, the irreversibility line depends on the vortex and defect dimensionality and the defect density [37].

The irreversibility line is practically measured either via the merging point of the " zero field cooled " (ZFC) and " field cooled " (FC) curves or by a particular criterion from the merging point of the upper and lower branches of the hysteresis loop. It must be noted that the irreversibility line strongly depends on the sample preparation and annealing conditions.

2.7 High-Temperature Superconductors (HTS)

The era of high-temperature superconductivity initiates from 1986 with the discovery of superconductivity in the Ba-La-Cu-O system with T_c ~ 30 K by J. G. Bednorz and K. A. Müller [41]. Soon after the Ba-La-Cu-O system, the yttrium barium system was discovered, which becomes superconducting at 90 – 95 K [42]. Another year passed before the bismuth and thallium systems raised transition temperatures into the triple-digit range [43-48]. These layered materials dominated by copper oxide planes have low electron densities compared to conventional metals, which leads to a low Fermi velocity. Dissipation due to a) operation at high temperature, b) short coherence length stemming from high T_c and the low electron density, and c) the anisotropy induced by the weak interlayer coupling puts severe restrictions on the vortex pinning efficiency of these materials. Despite extensive work on the entire HTS family, there is a shortage of comprehensive investigations on some members of each family. In this work concentration is on the Tl-1223 structure. A new technique for the lock-in angle measurement is also examined on a twinned Sm123 structure. To properly understand the mechanisms involved in superconductivity and the effect of magnetic field and temperature on vortex dynamics it is necessary to know the crystal structures of the compounds under study and similar compounds.

2.7.1 YBCO

The YBaCuO compounds can be obtained from the pervoskite structure in two crystalline forms, tetragonal or orthorhombic [Figures (2.3)(a) and (2.3)(b)]. The superconducting structure is generated by a phase transition from the tetragonal structure, which is stable at high temperatures above 700°C, to the orthorhombic. The transition is of the order-disorder type, with preferential occupancy of some oxygen sites in the orthorhombic structure accompanied by a small distortion from tetragonal to orthorhombic. Whereas in the tetragonal phase the chemical formula would be $YBa_2Cu_3O_{8-x}$, in the orthorhombic one (superconducting phase) it is $YBa_2Cu_3O_{6+x}$ with $0.5 < x < 0.9$. Quenching rapidly from 900°C, the tetragonal phase is preserved and is found not to be superconducting. In the system $YBa_2Cu_3O_{6+x}$ the absence of oxygen atoms plays an important role in the electronic properties of the system. For $x = 1$, the vacancies are due to the absence of oxygen atoms from the yttrium plane which separates the adjoining CuO_2 layers, and also from half of the oxygen sites in the CuO_2 conducting plane located between the Ba-O layers, which leads to the formation of the Cu-O chain. When x decreases from 1 to 0, oxygen atoms in the chain layer are removed, and some of the oxygen atoms are moved to empty sites, which eventually leads to the orthorhombic to tetragonal transformation. The superconducting transition temperature is highly dependent on the oxygen vacancy concentration [49]. For $0.8 \leq x \leq 1.0$, T_c is around 90 K; for x between 0.5 and 0.8, T_c decreases sharply to 60 K. Beyond $x = 0.5$, T_c drops sharply, and antiferromagnetic order has been observed near $x = 0.3$, 0.15 and 0 [50,51].

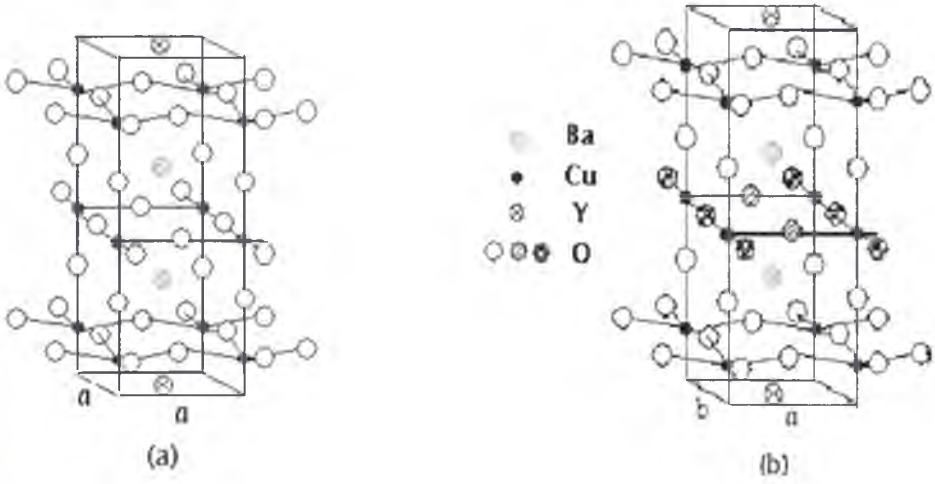

Figure 2- 3 Structure of YBCO. (a) The high-temperature tetragonal structure. The oxygen sites ○ are occupied at random. (b) The orthorhombic superconducting phase. Compared with the tetragonal structure, the oxygen sites ⊘ in the middle plane are occupied preferentially compared with ◒ sites, and there is a slight distortion from tetragonal to orthorhombic.

In the orthorhombic structure the lattice parameters a and b are 3.83Å and 3.88Å, respectively [52]. During the growth process, the a and b directions tend to interchange occasionally, so the direction in which the atoms are closest together (3.83Å) becomes the direction in which they are furthest apart (3.88Å), and vice versa. The resulting crystal is said to be twinned. Many boundaries between these two types of growth regions act as pinning centers to impede flux motion and prevent its flow. The higher T_c superconductors BiSrCuO, TlBaCuO, and also HgBaCuO, are all tetragonal with $a = b$, so they lack twinning planes and therefore have fewer pinning centers.

2.7.2 Sm123

After superconductivity above 90K was firmly established, yttrium was replaced by other rare earth elements to examine the role of Y in high-T_c superconductivity [53-58]. The role of the rare earth element in $REBa_2Cu_3O_y$ compounds is found to be the stabilization of the so-called three-layer structure, which sustains the 90 K superconductivity between the

RE-layers. Superconductivity is confined to CuO_2 planes sandwiched between the RE-layers [59]. As in YBCO, twin boundaries could be a source of flux pinning in this group. A phase separation due to spinodal decomposition of an unstable solid solution such as $Nd_{1+x}Ba_{2-x}Cu_3O_y$ causes spatially periodic variation in the cation ratio [60]. Regions where Nd substitutes into the Ba site, showing a lower T_c, alternate with ones with zero Nd substitution, having higher T_c. As the magnitude of the applied magnetic field increases, the regions with the lower T_c become non-superconducting and would then contribute to flux pinning [61]. In cation-stoichiometric Sm123 it was found that local oxygen deficiency is another source of flux pinning in rare-earth superconductors [62,63].

2.7.3 $TlBa_2Ca_2Cu_3O$

The TlBaCaCuO system crystallizes in the tetragonal structure and contains two important groups, $Tl_2Ba_2Ca_{n-1}Cu_nO_{2n+4}$ and $Tl_1Ba_2Ca_{n-1}Cu_nO_{2n+3}$ for n = 1, 2, 3, which have been listed in Table (2-1)[64-67]. Tl and Ba can be replaced by Pb and Sr, respectively.

Table 2- 1 T_c values for different compounds of Tl-based superconductors [64-67].

Compound	T_c (K)
$Tl_2Ba_2Ca_{n-1}Cu_nO_{2n+4}$	
$n = 1$	80-90
$n = 2$	100-110
$n = 3$	125-127
$Tl_1Ba_2Ca_{n-1}Cu_nO_{2n+3}$	
$n = 2$	75
$n = 3$	105-115

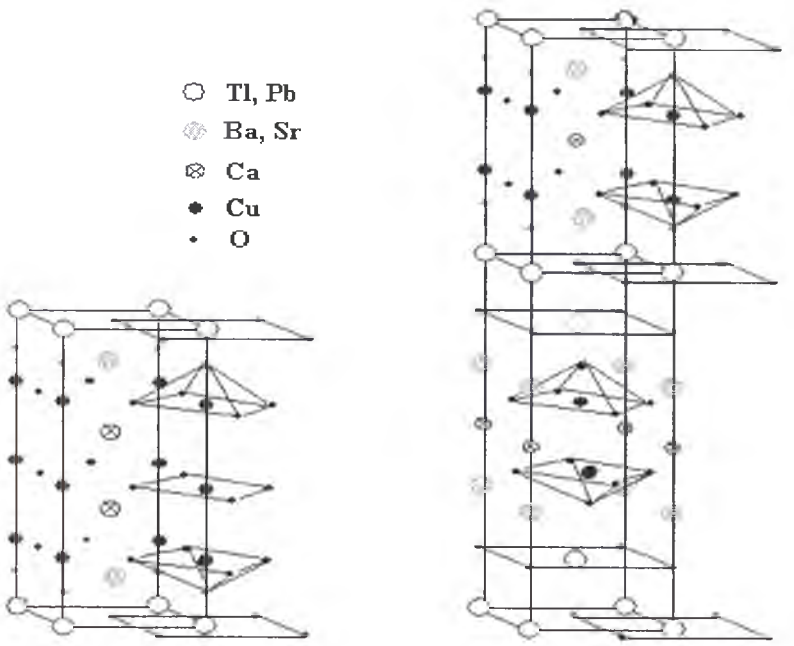

Figure 2- 4 Unit cells of $Tl_1Ba_2Ca_2Cu_3O_9$ and $Tl_2Ba_2Ca_1Cu_2O_8$. The compounds are tetragonal (or nearly tetragonal) with $a \approx 0.385$ nm. For the former compound c = 1.587 nm, and for the latter one c = 3.588 nm [65,66].

These two families have either 1 or 2 Tl-O blocking insulating layers, which separate the conducting Cu-O planes from each other [Figure (2.4)]. The magnetic coupling between adjacent Cu-O conducting planes depends upon the thickness of the insulating layer, i.e. upon the number of Tl-O layers.

The superconducting properties of the Tl-based group, namely those of the Tl2212, Tl2223 and Tl1223 phases, are, in the $H_{irr}(T)$ representation, superior to those of Bi2212 and Bi2223 at higher operating temperatures close to 77 K, independent of the phase system used. However, for all double layer systems of BSCCO and Tl-based groups, J_c decreases drastically in the presence of a magnetic field applied perpendicular to the Cu-O plane (hereafter called the crystal cell ab-plane).

Among the materials in the Tl-based compound family the best position of the irreversibility line belongs to the Tl1223 phase. As an explanation, it is accepted that stronger coupling between conducting Cu-O planes separated by a single-layer insulating Tl-O plane (with the thickness of the Tl-O bilayer and the single Tl-O layer 11.4 and 9.2Å, respectively [68]) is responsible for the improved properties of this kind of material in higher magnetic fields [69]. For investigating the effect of the Cu-O layer spacing on the superconducting properties, variant Tl-based superconductors (such as the Tl1223 and Tl1212 phases with a single Tl-O layer) have been synthesized [70,71]. The reported experimental results show that Tl1223 samples have higher critical current density, higher irreversibility field, and less anisotropy than Tl2223 samples owing to the stronger Josephson coupling of the Cu-O layers, affecting both the flux pinning energy and the properties of the vortex lattice [69,72-74].

It has been found that the substitution of Pb for Tl helps to stabilize the crystal structure and to promote the occurrence of bulk superconductivity in the Tl-Sr-Ca-Cu-O system [75]. The Pb substituted materials are isostructural with $TlBa_2Ca_2Cu_3O_y$. Due to the presence of Pb^{+4} at Tl^{+3} sites, the average copper-oxidation state is lowered, and the structure is stabilized [76,77]. It has also been shown that Pb substitution leads to a higher irreversibility line [78].

2.7.4 Anisotropy

One of the characteristic properties of oxide superconductors with high critical temperatures is a significant anisotropy originating from their crystal structures. That is, while the electrical conductivity in the CuO_2 plane is very high, that in the normal direction to the CuO_2 plane is very poor due to semiconducting or insulating blocking layers between

the planes. Thus, the type-II superconductors have two-dimensional properties. One of these properties is the anisotropy of the upper critical field. That is, whereas the upper critical field parallel to the CuO_2 plane or the ab-plane is very high, that perpendicular to the plane or along the c-axis is fairly low. The anisotropy depends on the electrical properties of the blocking layer. The extreme cases of anisotropy are $YBa_2Cu_3O_7$ with the smallest anisotropy and $Bi_2Sr_2CaCu_2O_8$ with the largest anisotropy. The anisotropy in the upper critical field is closely correlated to the anisotropy in the coherence length. That is, if the coherence length in the ab-plane is expressed by ξ_{ab}, and that along the c-axis as ξ_c, the upper critical fields parallel and normal to the ab-plane are respectively given by

$$H_{c2}^{ab} \simeq \frac{\Phi_o}{2\pi\xi_{ab}\xi_c}, \qquad H_{c2}^{c} \simeq \frac{\Phi_o}{2\pi\xi_{ab}^2}. \tag{2- 44}$$

The ratio of the above fields is $H_{c2}^{ab} / H_{c2}^{c} = \xi_{ab} / \xi_c$. Due to the high T_c, the majority of high-temperature superconductors generally have very short coherence lengths, particularly along the c-axis, so ξ_c is shorter than the lattice constant in this direction, a_c. This tendency is pronounced for $Bi_2Sr_2CaCu_2O_8$ with its highly two-dimensional structure. The anisotropy constant, defined as $\Gamma^{-1} = (\xi_{ab} / \xi_c)^2$, is ≈ 50-200 for highly anisotropic Bi- and Tl-based HTS, and a thermally activated crossover from the lower anisotropy (3D) to the higher anisotropy (2D) plays an important role in the macro-electromagnetic properties of these type-II superconductors, which are intrinsic to the material and occur when k_BT exceeds the Josephson coupling energy of the Cu-O layers.

Structure determinations, magnetometry, Raman spectroscopy [79] and studies of transport properties of thin films [80] have employed single crystals. However, most past scientific work has been carried out with polycrystalline or amorphous specimens, so the

measurements involve averages over the directionally dependent properties. In these systems, weak links put severe restrictions on practical applications of HTS.

References:

1 F. London and H. London, Proc. Roy. Soc. (London) **A149,** 71 (1935).

2 F. London and H. London, Physica **2,** 341 (1935).

3 V. V. Schmidt, P. Müller, and A. V. Ustinov, *The Physics of Superconductors* (Springer, New York, 1997).

4 A. B. Pippard, Proc. Roy. Soc. **A216,** 547 (1953).

5 P. G. de Gennes, *Superconductivity of Metals and Alloys*, 3rd ed. (Perseus Books Publishing, L. L. C., 1999).

6 M. Tinkham, *Introduction to Superconductivity*, Second ed. (McGraw-Hill, New York, 1996).

7 V. L. Ginzburg and L. D. Landau, Zh. Eksp.Teor. Fiz **20,** 1064 (1950).

8 L. D. Landau, Zh. Eksp.Teor. Fiz **7,** 371 (1937).

9 L. D. Landau and E. M. Lifshitz, *Statistical Physics*, Vol. 1, 3rd ed. (Nauka, Moscow, 1976).

10 R. P. Huebener, *Magnetic Flux Structures in Superconductors* (Springer-Verlag,, 1979).

11 J. Bardeen, L. N. Cooper, and J. R. Schrieffer, Phys. Rev. **108,** 1175 (1957).

12 E. H. Brandt, Rep. Progr. Phys. **58,** 1465 (1995).

13 E. H. Brandt, Physica C **369,** 10 (2002).

14 N. W. Ashcroft and N. D. Mermin, *Solid State Physics* (Holt, Rinehart and Winston,, 1976).

15 W. R. Hudson, *The Mixed State of Superconductors* (National Aeronautics and Space Adminstration, 1970).

16 W. H. Kleiner, L. M. Roth, and S. H. Autler, Phys. Rev. **133,** A1226 (1964).

17 P. L. Gammel, D. J. Bishop, G. J. Dolan, J. R. Kwo, C. A. Murray, L. F. Schneemeyer, and J. V. Waszczak, Phys. Rev. Lett **59,** 2592 (1987).

18 A. A. Abrikosov, Sov. Phys. JETP **5,** 1174 (1957).

19 P. G. De Gennes, (Perseus Books, 1999).

20 S. X. Dou, W. K. Yeoh, J. Horvat, and M. Ionescu, Appl. Phys. Lett. **83,** 4996-4998 (2003).

21 S. X. Dou, A. V. Pan, S. Zhou, M. Ionescu, X. L. Wang, J. Horvat, and P. R. Munroe, J. Appl. Phys. **94,** 1850 (2003).

22 H. Kupfer, T. Wolf, A. A. Zhukov, and R. Meier-Himer, Phys. Rev. B **60,** 7631 (1999).

23 J. Figueras, T. Puig, and X. Obradors, Phys. Rev. B **67,** 014503 (2003).

24 W. K. Kwok, U. Welp, G. W. Crabtree, K. G. Vandervoort, R. Hulscher, and J. Z. Liu, Phys. Rev. Lett **64,** 966 (1990).

25 W. K. Kwok, U. Welp, V. M. Vinokur, J. Fleshler, J. Downey, and G. W. Crabtree, Phys. Rev. Lett **67,** 390 (1991).

26 B. Dam, J. M. Huijbregtse, F. C. Klaassen, R. C. F. van der Geest, G. Doornbos, J. H. Rector, A. M. Testa, S. Freisem, J. C. Martinez, B. Stauble-Pumpin, and R. Griessen, Nature **399,** 439 (1999).

27 S. Tyagi and Y. Y. Goldschmidt, Phys. Rev. B **67,** 214501 (2003).

28 L. Civale, Supercond. Sci. Technol. **10,** A11 (1997).

29 M. Murakami, M. Morita, K. Doe, and K. Miyamoto, Jpn. J. Appl. Phys. **28,** 1189 (1989).

30 P. W. Anderson, Phys. Rev. Lett. **9,** 309 (1962).

[31] P. W. Anderson and Y. B. Kim, Rev. Mod. Phys. **36,** 39 (1964).

[32] P. H. Kes, J. Aarts, J. van den Berg, C. J. van der Beek, and J. A. Mydosh, Supercond. Sci. Technol. **1,** 242 (1989).

[33] C. P. Bean, Phys. Rev. Lett. **8,** 250 (1962).

[34] C. P. Bean, Rev. Mod. Phys. **36,** 31 (1964).

[35] A. M. Campbell and J. E. Evetts, Adv. Phys. **21,** 199 (1972).

[36] E. H. Brandt, Phys. Status Solidi B **77,** 709 (1976).

[37] G. Blatter, M. V. Feigel'man, V. B. Geshkenbein, A. I. Larkin, and V. M. Vinokur, Rev. Mod. Phys. **66,** 1125 (1994).

[38] G. W. Crabtree and D. R. Nelson, Phys. Today **50,** 38 (1997).

[39] J. L. Tallon, Singapore, 1994 (World Scientific), p. 52.

[40] J. R. Cooper, L. J.W., J. D. Johnson, P. Monod, H. Enriquez, H. J., and C. Changkang, Phys. Rev. Lett. **79,** 1730 (1997).

[41] J. G. Bednorz and K. A. Müller, Zs. Phys. B **64,** 189 (1986).

[42] M. K. Wu, J. R. Ashburn, C. J. Torng, P. H. Hor, R. L. Meng, L. Goa, Z. J. Huang, Y. Q. Wang, and C. W. Chu, Phys. Rev. Lett **58,** 908 (1987).

[43] C. W. Chu, J. Bechtold, L. Gao, P. H. Hor, J. Huang, R. L. Meng, Y. Y. Sun, Y. Q. Wang, and Y. Y. Xue, Phys. Rev. Lett. **60,** 941 (1988).

[44] H. Maeda, Y. Tanaka, M. Fukutomi, and T. Asano, Jpn. J. Appl. Phys. Lett. **27,** L209 (1988).

[45] L. Gao, Z. J. Huang, R. L. Meng, P. H. Hor, J. Bechtold, Y. Y. Sun, C. W. Chu, Z. Z. Sheng, and A. M. Hermann, Nature **332,** 623 (1988).

[46] R. M. Hazen, L. W. Finger, R. J. Angel, C. T. Prewitt, R. L. Ross, C. G. Hadidiacos, P. J. Heaney, D. R. Veblen, Z. Z. Sheng, A. E. Ali, and A. M. Herman, Phys. Rev. Lett **60,** 1657 (1988).

[47] Z. Z. Sheng, A. M. Herman, A. E. Ali, C. Almasan, J. Estrada, T. Datta, and R. J. Matson, Phys. Rev. Lett **60,** 937 (1988).

[48] Z. Z. Sheng and A. M. Herman, Nature **55,** 332 (1988).

[49] R. J. Cava, B. Batlogg, C. H. Chen, E. A. Rietman, S. M. Zahurak, and D. Werber, Nature **329,** 423 (1987).

[50] J. W. Lynn, W. H. Li, H. A. Mook, B. C. Sales, and Z. Fisk, Phys. Rev. Lett **60,** 2781 (1988).

[51] J. M. Tranquada, D. E. Cox, W. Kunnmann, H. Moudden, G. Shirane, M. Suenaga, P. Xolliker, D. Vaknin, S. K. Sinha, M. S. Alvarez, A. J. Jacobson, and D. C. Johnston, Phys. Rev. Lett **60,** 156 (1988).

[52] M. M. Oleksienko, N. N. Matyushenko, L. F. Verkhorobin, V. V. Derevyanko, V. N. Golovin, and S. D. Lavarinenko, Castle of Mauterndorf, Salzburg, Austria, 1988 (Plenum Press), p. 107.

[53] N. Hari Babu, D. A. Cardwell, W. Lo, and A. M. Campbell, Phys. Rev. B **61,** 735 (2000).

[54] M. R. Koblischka, A. J. J. Van Dalen, T. Higuchi, S. I. Yoo, and M. Murakami, Phys. Rev. B **58,** 2863 (1998).

[55] A. K. Pradhan, K. Kuroda, B. Chen, and N. Koshizuka, Phys. Rev. B **58,** 9498 (1998).

[56] T. Wolf, A.-C. Bornarel, H. Küpfer, R. Meier-Himer, and B. Obst, Phys. Rev. B **56,** 6308 (1997).

[57] T. Goto, K. Watanabe, and E. Ban, Physica C **388,** 409 (2003).

[58] K. Inoue, N. Sakai, K. Waki, and M. Murakami, Physica C **378,** 503 (2002).

[59] J. Yu, A. J. Freeman, and S. Massida, in *Novel Superconductivity*, edited by S. A. a. K. Wolf, V. Z. (Plenum Press, New York, 1987), p. 367.

[60] M. Nakamura, Y. Yamada, T. Hirayama, Y. Ikuhara, Y. Shiohara, and S. Tanaka, Physica C **259,** 295 (1996).

[61] S. I. Yoo, M. Murakami, and N. Sakai, Jpn. J. Appl. Phys. **33,** 1000 (1994).

[62] M. Kawano, H. Suematsu, T. Onda, M. Hayakawa, H. Ogiwara, M. Karppinen, and H. Yamauchi, Appl. Supercon. **5,** 119 (1998).

[63] H. Suematsu, M. Kawano, T. Onda, T. Akao, M. Hayakawa, H. Ogiwara, M. Karppinen, and H. Yamauchi, Physica C **324,** 161 (1999).

[64] S. S. P. Parkin, V. Y. Lee, E. M. Engler, A. I. Nazzal, T. C. Huang, G. Gorman, R. Savoy, and R. Beyers, Phys. Rev. Lett. **60,** 2539 (1988).

[65] S. S. P. Parkin, V. Y. Lee, A. I. Nazzal, R. Savoy, R. Beyers, and S. J. Placa, Phys. Rev. Lett. **61,** 750 (1988).

[66] C. C. Toradi, M. A. Subramanian, J. C. Calabrese, J. Gopalakrishnan, K. J. Morrissey, T. R. Askew, R. B. Flippen, U. Chowhdry, and A. W. Sleight, Science **240,** 631 (1988).

[67] M. Jergel, A. C. Gallardo, C. F. Guajardo, and V. Strbik, Supercond. Sci. Technol. **9,** 427 (1996).

[68] T. Nabatame, Y. Saito, T. Doi, K. Aihara, T. Kamo, and S. Matsuda, Physica C **190,** 114 (1991).

[69] D. N. Zheng, T. Doi, M. Okada, and K. Higashyama, J. Appl. Phys. **77,** 5287 (1995).

[70] Z. Z. Sheng and A. M. Herman, Nature **332,** 138 (1988).

[71] A. Soeta, T. Suzuki, S. Takeuchi, T. Kamo, K. Usami, and S. P. Matsuda, Jpn. J. Appl. Phys. **28,** L1186 (1989).

[72] R. S. Liu, D. N. Zheng, J. W. Loram, K. A. Mirza, and A. M. Campbell, Appl. Phys. Lett. **60,** 1019 (1992).

[73] D. H. Kim, K. E. Gray, R. T. Kampwirth, and J. C. Smith, Physica C **177,** 431 (1991).

[74] D. E. Peterson, P. G. Wahlbeck, M. P. Maley, J. O. Willis, P. J. Kung, J. Y. Coulter, K. V. Salazar, D. S. Phillips, J. F. Bingert, e. E. J., and W. L. Hults, Physica C **199,** 161 (1992).

[75] M. A. Subramanian, C. C. Toradi, J. Gopalakrishnan, P. L. Gai, J. C. Calabrese, T. R. Askew, R. B. Flippen, and A. W. Sleight, Science **242,** 249 (1988).

[76] J. B. Parise, P. L. Gai, M. A. Subramanian, J. Gopalakrishnan, and A. W. Sleight, Physica C **159,** 245 (1989).

[77] D. B. Kang, D. Jung, and M. H. Whangbo, Inorg. Chem. **29,** 257 (1990).

[78] Y. C. Kim, J. R. Thompson, D. K. Christen, M. Paranthaman, and E. D. Specht, Physica C **253,** 357 (1995).

[79] R. J. Hemley and H. K. Mao, Phys. Rev. Lett **58,** 2340 (1987).

[80] M. Suzuki and T. Murakami, Jpn. J. Appl. Phys. **26,** L524 (1987).

CHAPTER THREE: VORTEX DYNAMICS IN HIGH-T_c SUPERCONDUCTORS

High-temperature copper oxide superconductors exhibit an unusual magnetic field-temperature (H -T) phase diagram that differs from that of conventional superconductors [1,2]. The mean-field H-T phase diagram of conventional superconductors simply comprises a Meissner phase at low magnetic fields $H < H_{c1}$, separated from the mixed phase at higher fields $H > H_{c1}$ up to H_{c2}. However, HTSs show complex H-T phase diagrams, due to thermal fluctuation of vortices combined with static effects, anisotropy and short coherence lengths.

The basic framework for the phenomenological description of high-temperature superconductivity, where the superconductor anisotropy is taken into account, is given by the generalized Ginzburg-Landau (GL) free-energy density functional

$$f_{GL}=f_n+\alpha(T)|\Psi|^2+\frac{\beta}{2}|\Psi|^4+\sum_{q=1}^{3}\frac{1}{2m_q}\left|\left(\frac{\hbar}{i}\frac{d}{dx_q}-\frac{2e}{c}\mathbf{A}_q\right)\Psi\right|^2+\frac{H^2}{8\pi}-\frac{H.H_o}{4\pi} \qquad (3\text{-}1)$$

with the same factors which were defined in equation (2-12). Furthermore, the parameters m_q, q = 1, 2, 3, denote the effective masses along the main axes of the crystal, which has an implication of anisotropy in HTS. In this way the penetration depths $\lambda_q = \lambda\sqrt{m_q}$ describe the exponential decay of components of the supercurrent pointing along the principal directions, and the corresponding coherence lengths $\xi_q = \xi\sqrt{m_q}$ characterize the spatial variation of the order parameter along these directions. In new HTS, one encounters either the isotropic case ($m_q = m$, q = 1, 2, 3) or the uniaxially anisotropic, that is, $m_x = m_y = m$ and $m_z = M$. In this way, the mass anisotropy is defined as

$$\Gamma^2 = m / M < 1. \qquad (3\text{-}2)$$

Commonly the ratio of two experimentally accessible upper critical fields (section 2.7.4) is used to quantify the mass anisotropy[2]. This quantity for a highly anisotropic superconductor

like Bi2212 takes the value $\Gamma^{-1} \simeq 150$ [3], and for superconductors with low anisotropy properties, typical values are $6 < \Gamma^{-1} < 8$ [4,5] for YBCO and $2 < \Gamma^{-1} < 5$ [6,7] for MgB_2.

In this chapter, after introducing the vortex structure in HTS we step forward beyond the mean-field phase diagram and discuss the dynamic properties of the vortex system in the presence of quenched and thermal disorder, as much as is needed for the discussion of the observed behaviours for the samples under investigation.

3.1 Vortices in Layered HTSs

A commonly adopted picture of the vortex system in layered superconductors is that of 2D vortices in each layer, which are called pancake vortices [8]. These 2D vortices in neighbouring layers are connected to each other via their magnetic interaction and the Josephson coupling. The latter interaction drives tunnelling currents when two vortex segments are displaced relative to each other. Depending on the strength of the electromagnetic attraction between the layers, the superconductor can behave as a 3D continuum or a discrete array of Cu-O planes separated by buffer layers of charge reservoir. For a low anisotropy material, a description in terms of the anisotropic Ginzburg-Landau equation, equation (3- 1), or the London theory is applicable. For a strongly anisotropic superconductor, the discrete Lawrence-Doniach (LD) [9] model can provide a reliable description. The usual criterion for selection of either an isotropic continuum or a 2D discrete description of a superconductor is the ratio of the coherence length along the c-axis ξ_c to the layer spacing d, $\tau_{cr} = 2\xi_c^2(0)/d^2$. This ratio characterizes the crossover from quasi-2D layered to continuous 3D anisotropic behaviour. Therefore, for superconductors with a large coherence length $\xi_c(0)$, i.e. $\tau_{cr} \gg 1$, the continuous description is appropriate.

Conventional superconductors and MgB_2 with a large coherence length[10] are good candidates for the continuous description. On the contrary, Bi- and Tl_2-based superconductors with small coherence lengths are well described by the discrete Lawrence-Doniach (*LD*) model. Meanwhile, as a result of temperature or field application, a crossover between 2D⇌3D is possible [11]. In what follows, the *LD* model and its consequences are briefly explained, and in particular the pancake vortex structure is introduced.

Since a layered superconductor can be visualized as a discrete set of superconducting layers with order parameter Ψ_n separated by a distance d and coupled together by a Josephson term, the Gibbs free energy in this case is written as[2]

$$f[\Psi_n,\mathbf{A}]=\int d^2R\left\{d\sum_n\left(\alpha|\Psi_n|^2+\frac{\beta}{2}|\Psi_n|^4+\frac{\hbar^2}{2m}\left|\left[\frac{\nabla^{(2)}}{i}+\frac{2\pi}{\Phi_0}\mathbf{A}^{(2)}\right]\Psi_n\right|^2\right.\right.$$

$$\left.\left.+\frac{\hbar^2}{2Md^2}\left|\Psi_{n+1}\exp\left[\frac{2\pi i}{\Phi_0}\int_{nd}^{(n+1)d}dzA_z\right]-\Psi_n\right|^2\right)+\int dz\left[\frac{H^2}{8\pi}-\frac{\mathbf{H}.\mathbf{H}_0}{4\pi}\right]\right\}. \qquad (3\text{-}3)$$

In fact the above formula is a discrete version of the continuous anisotropic GL functional (3- 1). Using a London-type approximation by assuming a constant modulus Ψ_n within the planes and allowing only for phase degrees of freedom (currents) we derive[2]

$$f[\varphi_n,\mathbf{A}]=\int d^2R\frac{\hbar^2|\Psi_n|^2d}{2m}\left\{\sum_n\left(\nabla^{(2)}\varphi_n+\frac{2\pi}{\Phi_0}\mathbf{A}^{(2)}\right)^2+\right.$$

$$\left.\frac{2m}{Md^2}\left[1-\cos\left(\varphi_{n+1}-\varphi_n+\frac{2\pi}{\Phi_0}\int_{nd}^{(n+1)d}dzA_z\right)\right]\right\}+\int d^3r\left[\frac{H^2}{8\pi}-\frac{\mathbf{H}.\mathbf{H}_0}{4\pi}\right] \qquad (3\text{-}4)$$

Using a similar variational method to that which was applied in Chapter 2 for the *GL* and the London equations with respect to the vector potential $\mathbf{A}$ and the phases φ_n for equation

(3- 4), we would end up with planar and z-axis differential equations for **A** and a single differential equation for $\varphi_n{}^2$. From these equations the Josephson-coupling current density between the layers is obtained as

$$J_J = \frac{c\Phi_0\Gamma^2}{8\pi^2\lambda_L^2 d} = \frac{c\Phi_0\Gamma}{8\pi^2\lambda_L^2\Lambda}, \qquad (3\text{- }5)$$

where $\Lambda = d/\Gamma$.

3.1.1 Josephson Vortices

An interesting result from the above-mentioned differential equations relates to the case in which a magnetic field is applied parallel to the *ab* plane. As a result, vortices appear, which are known as Josephson vortices and are characterized by two length scales, $\Lambda = d/\Gamma$ and $\lambda_c = \lambda_L/\Gamma$. This type of vortex includes a core region with dimensions Λ and d, while outside it the discreteness is irrelevant. However, inside this region the gauge-invariant phase difference is large and changes rapidly; the current density reaches its maximum value J_J, defined in (3-5), and the order parameter in the adjacent layers is weakly suppressed. This circulating vortex current tunnels across the isolating space between the layers[2].

3.1.2 Pancake Vortices

The starting point for the study of a layered superconductor is the vortex in an isolated thin layer[12]. A superposition of these thin layers into a stack can provide the real configuration of the vortex system in a layered superconductor. In this case, one could face two different situation, that is, either a layered superconductor with $J_J = 0$ [8,13,14] or with $J_J > 0$ [15,16]. This section is restricted to the former case where the coupling between layers is

purely electromagnetic and the field of a single pancake vortex located at $r = 0$ is confined to a layer of thickness $\approx 2\lambda_{ab}$. The z-component and in-plane radial components of the magnetic field are as follows[17]:

$$B_z(r) = \frac{\Phi_o}{4\pi\lambda_L^2}\frac{d}{r}e^{-r/\lambda},$$

$$B^{ab}(r) = \frac{\Phi_o}{4\pi\lambda_L^2}\frac{zd}{r_\perp}\left[e^{-|z|/\lambda} - \frac{|z|}{r}e^{-r/\lambda}\right] \qquad (3\text{-}6)$$

where $r_\perp = (x ; y)$ and $r = (x ; y ; z)$. The shape of the magnetic field distribution is quite different from the problem of an individual isolated monopole-like pancake, which was originally solved by Pearl [12]. That is, due to the screening effects of the adjacent layers the field is compressed into a narrow strip of size λ along the z-axis, and the magnetic field extends parallel to the layers rather than spreading out uniformly over the entire solid angle. Although the pancake vortices in the same layer exert repulsive force on each other, those in different layers attract each other.

3.2 Vortex Pinning and Vortex Creep

3.2.1 Surface and Geometrical Barriers

It has been shown that the Bean-Livingston [18] surface barrier plays an important role in vortex dynamics in HTS [19]. This barrier arises from the competition between repulsion of a vortex from the surface due to its interaction with the shielding currents and the attraction of the vortex to its mirror image. The irreversible component of the magnetic moment could be a superposition from both surface barriers and bulk pinning. Their relative contributions depend on the quality of the sample surface and vary with temperature and field. In samples with very smooth interfaces, this barrier leads to

irreversible field-dependent magnetization loops *M(H)* and finite critical currents even in the absence of inhomogeneities. The most typical method that can monitor the surface barrier is a hysteresis loop measurement, where the descending branch of the loop touches $M = 0$ [20]. Nevertheless, defects in the interface may cause the local destruction of the surface barrier, opening leaks to vortex entry. Of course the surface barrier, as a source of irreversible magnetization, leads to different flux creep rates for flux entry and exit [21,22]. In a twinned sample, due to the presence of the twin planes as weak spots for flux entry at the surface, surface barriers are absent [19].

A geometrical barrier arises from a competition between the elongation energy of a vortex penetrating into the sample through the corners of the sample and the Lorentz force [23,24]. The geometrical barrier is observed in type-II superconducting [23-27] non-ellipsoidal samples (slabs, films) with a high demagnetising factor, when they are placed in a perpendicular magnetic field. The barrier was first observed in type-I superconductors [28], which demonstrate an irreversible behaviour of the magnetic flux penetration inside the sample. The geometrical barrier was shown to be responsible for a visible magnetization hysteresis, which is exclusively caused by the shape of the near-the-edges cross-section of a sample. Furthermore, it has been shown that this barrier has higher strength at elevated temperature [29].

3.2.2 Classical Creep

At extremely low temperatures (≈ 0K) vortices can be de-pinned from their pinning site by the action of the Lorentz forces from the driving current density $J \geq J_c$ (irrespective of quantum tunnelling phenomena). At finite temperatures, however, thermal energy may allow vortex lines to jump from one pinning point to another in response to the driving

force of the current and the flux density gradient for $J \ll J_c$. This vortex gradient is related via Maxwell's equation $\nabla \times \mathbf{H} = (4\pi/c)\boldsymbol{J}$ to the macroscopic screening or transport current density of the superconductor. Due to thermally activated motion of the vortices, a sample carrying either of these currents would be in a thermodynamically metastable state. Flux creep, in fact, is a directed motion of fluxes toward thermodynamic equilibrium through changing the spatial arrangement of fluxes. As a result of the rearrangement of microscopic current loops, magnetic moment changes with elapsed time. The flux density gradient gradually decreases and the magnetic moment (or the screening currents) subsequently decays. The concept of flux creep was originally introduced by Anderson and Kim [30,31]. The resulting flux creep can be quantified using Blatter et al.'s approach[2] as follows. For simplicity, we consider a slab geometry with width $2d$ located parallel to the zy-plane between $x = -d$ and $x = +d$, with vortex lines aligned along the z-axis and moving along the x-axis. With the assumption that the induction is large compared to the magnetization, i.e., $H \simeq H_o$, the above Maxwell's equation becomes

$$\frac{\partial H_z}{\partial x} = -\frac{4\pi}{c} J_y . \qquad (3\text{-}7)$$

The basic equation governing the decay of the current density J can be derived from the Maxwell's equation $\partial E / \partial x = -(1/c)\, \partial H / \partial t$ and the equation relating the electric field to the flux motion $E = (1/c)\, H\, v$, where v is the velocity of the fluxes in a direction parallel to the Lorentz force, i.e., the x direction. For the sake of simplicity the subscript y and z have been omitted. These considerations lead to the equation of continuity for the flux-line density [32]

$$\frac{\partial H}{\partial t} = -\frac{\partial}{\partial x}(vH). \qquad (3\text{-}8)$$

From equation (3-7) the corresponding dynamic equation for the current density J is obtained to be

$$\frac{\partial J}{\partial t} = \frac{c}{4\pi}\frac{\partial^2}{\partial x^2}(vH)\,. \qquad (3\text{-}9)$$

Thermal activation of fluxes over the pinning barrier $U(J)$ leads to the velocity v [expressed in equations (3-8) and (3-9)] which follows the equation

$$v = v_o e^{-U(J)/k_BT} \qquad (3\text{-}10)$$

where the pre-exponential factor is given by $v_o = x_o\, \omega_m\, J/J_c$, with x_o being the hopping distance, while ω_m is the microscopic attempt frequency, and the factor J/J_c is introduced to provide a gradual crossover to the flux flow regime in which $v \propto J$ at $k_BT \gg U$ [33,34]. Using two boundary conditions: i) $vH = 0$ at the center, due to the motion of the same amount of flux in opposite directions, and ii) $H\ (x = \pm d) = H_o$, where H_o is the applied field and independent of time, integration of (3-9) between the center and the edge of the slab yields

$$\frac{\partial J}{\partial t} \approx -\frac{cv_oH_o}{2\pi d^2}e^{-U(J)/k_BT}, \qquad (3\text{-}11)$$

where U is the activation energy at the surface of the slab. Using the mathematical chain rule in (3-11) leads to

$$\frac{dU}{dt} \approx -\frac{cv_oH_o}{2\pi d^2}\frac{dU}{dJ}e^{-U(J)/k_BT}. \qquad (3\text{-}12)$$

Solving the above equation with logarithmic accuracy [35] yields

$$U(J) = k_BT\ln(t/t_o), \qquad (3\text{-}13)$$

where $t_o = 2\pi k_B T d^2/(c v_o H_o |\, dU/dJ\,|)$ is a macroscopic quantity depending on the sample size d. Via the above equation for t_o, the time dependence of the screening current density can be obtained provided that the $U(J)$ function is known.

In the simplest possible model of pinning, Anderson and Kim [30,31] assumed a linear dependence of U on current density as

$$U = U_o - \frac{1}{c} JH\, x_o V, \tag{3- 14}$$

where V is the jumping flux bundle volume and x_o is the hopping distance. In this equation the second term is the work done by the Lorentz force in moving the flux bundle over the distance x_o. In this model V and x_o are assumed to be J and H independent, and therefore relation (3-14) becomes

$$U = U_o (1 - J/J_{co}). \tag{3- 15}$$

$J_{co} = cU_o / H\, x_o V$ is the critical current density corresponding to $U = 0$, which is J_c defined from the equivalence between the Lorentz force and the pinning force (equation 2-42). From equations (3-13) and (3-15), the logarithmic time dependence of the current density is obtained

$$J = J_{co}\left[1 - \frac{k_B T}{U_o} \ln\left(\frac{t}{t_o}\right)\right]. \tag{3- 16}$$

In order for the above expression to be applicable at $t = 0$, it is usually written as

$$J = J_{co}\left[1 - \frac{k_B T}{U_o} \ln\left(1 + \frac{t}{t_o}\right)\right]. \tag{3- 17}$$

The normalized relaxation from this model can be derived as:

$$S = \frac{1}{M}\frac{dM}{d\ln t} = \frac{d\ln M}{d\ln t} = \frac{d\ln J}{d\ln t} = \frac{-k_B T}{U_o - k_B T \ln(t/t_o)}. \qquad (3\text{-}18)$$

For low-temperature superconductors in which $U_o \gg k_B T \ln(t/t_o)$, S reduces to $-k_B T/U_o$. In fact, the relaxation rate is controlled by an activation energy that results from the interaction between the defects and the vortex system. The fast relaxation and the large decrease of the persistent currents with temperature in HTSs are direct consequences of their small activation energies.

Since $E \propto vH$ and v is related to barrier energy via (3-10), a close relation is established between flux creep and the *I-V* (or *E-J*) characteristics as

$$E \propto H \exp\left[-\frac{U_o}{k_B T}\left(1 - \frac{J}{J_{co}}\right)\right]. \qquad (3\text{-}19)$$

In practice, the Anderson-Kim model can provide a fair description of conventional superconductors in which U_o (~100-1000K) $\gg k_B T$ [36,37] and therefore the persistent current is in vicinity of the critical current density. However, due to the giant flux creep in HTS [36,37] and thus relaxation of the current density far below the critical current density, this model is not able to describe them properly. In fact, the large logarithmic decay rates in HTS are the result of various factors, such as the high temperatures available in an experiment, the small pinning energies U_o, which in turn are a consequence of the small coherence length, ξ, and the large anisotropy of the oxides. It follows that in order to investigate the vortex dynamic in HTS, studying the circumstances in which $J \ll J_c$ is required.

3.2.3 Collective Pinning Theory

Due to the perovskite nature of the high-temperature superconductors, one important candidate vortex pinning centre is represented by oxygen vacancies in the superconducting CuO_2 layers. However, no random distribution of pinning centres can lead to an effective pinning in a rigid vortex lattice. Since for any position of a vortex line, the same number of random pinning sites would be encountered by the vortex line, the energy of the vortex line is the same everywhere in the superconductor. Therefore the vortex line is not pinned down. An elastic vortex line, on the other hand, will be able to adjust itself to the random pinning forces and thereby lowers its energy by passing through the favourable pinning sites. However, this energy reduction is offset by an increase in the elastic energy of the vortex line. The equilibrium vortex-line configuration corresponds to the situation where the sum of these two energies is at a minimum. This concept was originally developed by Larkin and Ovchinnikov (*LO*) and is known as *LO Collective Pinning* (*CP*)[38,39]. The concept of collective pinning comes from the collective action of many weak pinning centres where the local distortion of the vortices is smaller than the coherence length. According to this theory, for a vortex lattice under the influence of a random array of pinning centres with a short-range pinning potential [39]

$$\left\langle U_{pin}(\mathbf{u},\mathbf{r})U_{pin}(\mathbf{u}',\mathbf{r}')\right\rangle = K(|\mathbf{u}-\mathbf{u}'|,|\mathbf{r}-\mathbf{r}'|) \qquad (3\text{-}20)$$

where **u** and **r** represent the displacement and position vectors, and K(x, y) is a severely decreasing function of x and y beyond a characteristic length r_p, where the long-range order of the lattice is lost. For the case where the defect size is smaller than the coherence length we have $r_p \simeq \xi$, which is used hereafter. That is, in spite of large-scale distortion in the vortex system, the macroscopic sample volume can be divided into correlation volumes V_c

within which the vortex line lattice is reasonably undistorted. The transverse and longitudinal dimensions of this volume relative to the field direction, which optimise the trade-off between the elastic and pinning energies, are $R_c \simeq r_p^2(C_{44}C_{66}^3)^{1/2}/\gamma$ and $L_c \simeq (C_{44}/C_{66})^{1/2}R_c$, respectively. C_{44} and C_{66} are elastic moduli of the vortex lattice (section 2.5). γ relates to the elementary pinning force exerted by a pinning centre on the vortex line[39]

$$\gamma = \int d^3r \left[\frac{\partial^2 K(u,r)}{\partial u^2} \right]_{u=\xi} . \qquad (3\text{-}21)$$

In the literature sometimes γ is called the disorder parameter. The critical current density for 3D pinning from the *LO* theory is predicted to be[38]

$$J_c H \simeq C_{66} r_p / R_c^3 \simeq \gamma^2 / (2 r_p^3 C_{66}^2 C_{44}). \qquad (3\text{-}22)$$

That is, critical current density could be connected to R_c and L_c. This can be investigated by finding the current dependence of the pinning potential, $U(J)$, because the pinning potential is experimentally accessible (to be discussed in later sections). To introduce this, two interesting and practical cases are usually considered: i) $J \sim J_c$, which is applicable to conventional superconductors with strong pinning potential and low transition temperature, which leads to insignificant vortex creep, and ii) $J \ll J_c$ for HTS superconductors with high critical temperature (originating in their small coherence length) and weak pinning potential. In this case one faces considerable vortex creep and therefore a current density that has relaxed to a much smaller value than the critical one. In what follows, the two above-mentioned cases are briefly reviewed.

Case $J \sim J_c$: For the simplest state of $H \sim H_{c1}$ for an isotropic medium where all the elastic constants have the same order of magnitude, say C, the activation energy is calculated to be

$$U_c \sim C\,(\xi / R_c)^2\, V_c. \qquad (3\text{-}23)$$

To obtain the above expression it is assumed that the flux hopping distance for accommodating a low-lying energy state is $\sim \xi$.

For the case $H \gg H_{c1}$, where $C_{11} = C_{44} \gg C_{66}$, and therefore R_c, L_c and J_c are more dependent on the shear and tilt constants rather than on C_{11}, it can be shown that:

$$U_c \sim C_{66}\,(\xi / R_c)^2\, R_c\, L_c^2 \sim (C_{66}\, C_{11})^{3/2} \xi^4 / \gamma \qquad (3\text{-}24)$$

The ratio of the two expressions (3-23) and (3-24) is simply calculated to be $\sim (C_{11}/C_{66})^{1\,2}$. This means that the second activation energy is larger than the first one by this factor. The reason is believed to be the formation of large-sized vortex bundles, comprising some independent sub-bundles of volume V_c, with size of the order of $\sim (C_{11}/C_{66})^{1,2}$, and thus bigger than the sub-bundles[39] (note $C_{11} \gg C_{66}$) . This means that vortices tend to hop in larger groups rather than in individual sub-bundles.

Case $J \ll J_c$: In this regime it is proved that the bundle size grows even beyond even that of the aforementioned vortex bundle with decay of the current density[39]. Due to the smallness of the current density leading to a weak Lorentz force, the hopping distance of the vortex bundle should be much larger than in the previous case to be able to find the low-lying energy states. Within this theory the hopping distance, $u_{hop}(J)$, is determined to be

$$JH\, u_{hop}(J) \sim C_{66}\, u_{hop}^2(J) / R_\perp^2(J) \qquad (3\text{-}25)$$

where $R_\perp(J)$ is the bundle size in the plane perpendicular to the plane formed by the applied field and the hopping vectors. Finding the function $u_{hop}(J)$ is impossible unless we have some additional relationship between $u_{hop}(J)$ and $R_\perp(J)$. It was shown by

Feigel'man et al [39] that fluctuations of the displacement field u in an interacting elastic medium with random potential grows as

$$u(R) = \left\langle | \mathbf{u}(\mathbf{r}) - \mathbf{u}(\mathbf{r}+\mathbf{R}) |^2 \right\rangle^{1/2} \propto R^{\zeta} . \qquad (3\text{-}26)$$

On substituting (3-26) into (3-25), one arrives at

$$u(J) \propto J^{-\zeta/(2-\zeta)}, \qquad R_{\perp}(J) \propto J^{-1/(2-\zeta)},$$

$$R_{\parallel} \simeq L \simeq (C_{11}/C_{66})^{1/2} R_{\perp}, \qquad U(J) \propto J^{-\alpha} \qquad (3\text{-}27)$$

where $\alpha = (d-2+2\zeta)/(2-\zeta)$ and d is the dimensionality of the flux medium (e.g., for a single vortex line its value is d=1). From the equality between fluctuation of the random pinning energy ΔE_{pin} and the fluctuation of the elastic energy ΔE_{el} the exponent ζ - known as the wandering exponent- has been determined to be[40]

$$\zeta_{d,n} = 2(4-d)/(8+n) \qquad (3\text{-}28)$$

where n is the dimensionality of the displacement vector $\mathbf{u}(\mathbf{r})$. The main assumption in deriving the above expression for the wandering exponent is that ΔE_{pin} does not depend on the elastic modulus, but depends on V (the fluctuating volume), the displacement u, and γ and ξ. Since going through the details of the calculations, which needs some rigorous statistical averaging to be taken over the dynamical variables and over the quenched variables describing the disorder[2,39], is beyond the scope of the present work, some results of this theory for different fields and current densities are outlined. For instance, J_c of a high temperature superconductor at low field is independent of the applied field. From the *CP* theory point of view this means that in a dilute vortex system R_c is smaller than the vortex lattice parameter $a_o \simeq (\Phi_o/H)^{1/2}$ and therefore the collective pinning of the individual vortex lines leads to the field independence of J_c. The pinning is accordingly just

characterized by the longitudinal collective length, L_c, which is field-independent[39]. In this single vortex regime, which corresponds to $\xi < L_c < a_o$, the collective energy and the critical current density are

$$U_c \sim H_c^2 \xi^3 (\xi / L_c), \quad J_c \sim H_c \lambda_L^{-1} (\xi / L_c).$$

In the theoretical treatment of collective pinning Feigel'man et al predicted the existence of three different regimes of current density J. For example, for the current range $J_c > J > J_1 \sim J_c (L_c / a_o)^{2-\zeta_{1,2}} = J_c (L_c / a_o)^{7/5}$, the vortex bundle would be a portion of vortex line with length within the range $L_c < L < a_o$. Inserting all this information into relations (3-27), (3-28) and (3-13) in addition to $d = 1$ we arrive at the following expressions for the vortex creep energy and the decay of the current density:

$$U(J) \sim U_c \left(\frac{J_c}{J} \right)^{1/7}, \quad J(t) \sim J_c \left[\frac{U_c}{k_B T \ln(t/t_o)} \right]^7. \tag{3-29}$$

In the second region with lower J where $J_1 > J > J_2 = J_1 (a_o / \lambda)^{2/3}$, the hopping bundle has a transverse size of about λ. This region is characterized by a severely dispersive behavior in the elastic constants. In this case we have

$$U(J) \sim U_1 \left(\frac{J_1}{J} \right)^{5/2}, \quad J(t) \sim J_1 \left[\frac{U_1}{k_B T \ln(t/t_o)} \right]^{2/5}, \quad U_1 \simeq U_c (a_o / L_c)^{1/5}. \tag{3-30}$$

As for the third region with even lower current density it would end up with

$$U(J) \sim U_2 \left(\frac{J_2}{J} \right)^{7/9}, \quad J(t) \sim J_2 \left[\frac{U_2}{k_B T \ln(t/t_o)} \right]^{9/7}, \quad U_2 \simeq U_1 (\lambda / a_o)^3. \tag{3-31}$$

Thus the set of $J(t)$s for different regimes predict that current density is a decreasing function of temperature and time, and these results could be exploited for discussion of any observed behaviour in the decay of the current density (or equivalently the magnetic

moment) to reveal the size and dynamics of vortex bundles. All the above results including those of Anderson-Kim (3-15) could be unified and expressed in the so-called interpolation formula, which is

$$U(J) \sim U_c \left[\left(\frac{J_c}{J} \right)^{\mu} - 1 \right], \quad J(t) \sim J_c \left[1 + \frac{\mu k_B T}{U_c} \ln\left(\frac{t}{t_o} \right) \right]^{-1/\mu}, \tag{3-32}$$

where the exponent μ is connected to the dimensionality of the vortex matter which was determined for the three regimes, (where for the Anderson-Kim model it takes the value μ = -1). The experimentally observed logarithmic dependence of the activation barrier on the current density J is close to the power law (3-32) with $\mu \ll 1$, which is expected to describe single-vortex creep [41,42]. It has been shown that in the case of collective vortex creep a differentiation between small, medium, and large bundle pinning leads to μ = 7/4, 13/16, and 1/2, respectively [43]. For highly anisotropic material for which the creep is two-dimensional, μ = 9/8 and 1/2 for single vortex and collective vortex creep, respectively. These results are valid for hopping distances much shorter than the Abrikosov lattice constant.

Applying the normalized relaxation rate definition in (3-18) to (3-32), we will end up with

$$S = \frac{k_B T}{U_c + \mu k_B T \ln(t/t_o)}, \tag{3-33}$$

which is different from the Anderson-Kim predictions of equation (3-18). Two striking results from the last equation are: S is a decreasing function of time, and at elevated temperatures, the second term in the denominator dominates U_c, and then S saturates to [44,45]

$S = 1/\mu \ln(t/t_o)$. (3- 34)

This means, unless either μ or t_o is dependent on T, S will have a plateau, which has been observed experimentally [44].

A similar activation barrier is obtained from the Vortex-Glass model[44,46](which is a thermodynamic model equivalent to the Collective Vortex Creep theory of Feigel'man), except that this model predicts μ to be less than one.

3.2.6 Vortex Solid-Solid transition/crossover; Elastic-Plastic crossover and Order-Disorder transition

Due to the proportionality of the vortex bundle volume to $1/J$ [38,39,47] in Feigel'man's Collective Vortex Creep theory (previous section), we face diverging energy barriers [39,48]. That is, with vanishing current density ($J \rightarrow 0$) in particular at high temperatures, the vortex bundle volume that will have to move coherently increases. One difficulty with collective pinning is that tearing of the lattice is not taken into account in estimating J_c: i.e., the lattice de-pins elastically, not plastically. Plastic deformation of the vortex lattice may allow us to break the vortex bundle volume up into smaller fractions, which can be moved by a finite-energy source. However, as soon as the energy barrier associated with this volume exceeds the plastic barrier the increase in the energy barrier with decreasing J is cut off at a certain scaling current [49]. In Collective Vortex Creep theory only the elastic deformation of the vortex lattice by defects is considered. This theory's main result (equation (3-32)) clearly puts a limit on any vortex-displacement mechanism based on elastic vortex creep. Therefore, considering an alternative to elastic creep of vortex bundles is necessary[13,49-51]. The pioneering experimental investigation of the existence of plastic creep relied on transport measurements in the vicinity of the melting line, where the vortex lattice starts

softening and the entanglement of vortices increases[52-54]. At temperatures above the irreversibility line up to the liquid phase in the vicinity of the melting line, the vortex system is akin to a highly viscous liquid. The energy barrier in this regime is associated with the thermally activated plastic motion of the vortex structure. The size of the characteristic plastic barriers has been estimated by Geshkenbein *et al.* based on the assumption that these barriers involve the excitations of deformations of the vortex system on the scale of the vortex lattice spacing, a_o[50]

$$U_{pl} \simeq \Gamma \varepsilon_o a_o \propto (T_c - T)/\sqrt{H} \qquad (3\text{-}35)$$

where Γ is the anisotropy parameter, defined in (3-2), and ε_o is the vortex line tension, defined in expression (2-29) as $\varepsilon_o = (\Phi_o/4\pi\lambda)^2$.

However, within the last decade, numerous experimental results show that plastic deformation does not necessarily occurs as a pre-melting stage, and such deformations might invade a considerable portion of the solid vortex lattice state far below the melting line in the *H-T* phase diagram [55-58]. Furthermore, these deformations are mainly believed to be due to dislocation mediated plastic creep, similar to the diffusion of dislocations in atomic solids [39,50,59]. From the dislocation theory of atomic solids the current dependence of the activation energy is calculated to be as

$$U(J) = U_{pl}(1 - \sqrt{J/J_{pl}}) \qquad (3\text{-}36)$$

where U_{pl} is the field dependence of the activation energy and J_{pl} is the plastic critical current density. In this way a finite pinning barrier (rather than the diverging pinning barrier of Collective Pinning theory) governs the vortex system. Since the diffusion coefficient is exponentially small, plastic vortex creep is negligible at low temperatures. The low-energy barrier U_c associated with elastic creep in the critical state can then explain

the rapid decay with time of non-equilibrium magnetization. Generally speaking, despite the presence of both elastic and plastic barriers, the lower barrier controls the vortex dynamics. To clarify which barrier governs the vortex system in a superconductor, the field dependence of the pinning energy, U_{pl}, could be a leading pointer. For example, several approaches have shown that in the collective creep theory the pinning energy is an increasing function of magnetic field[60,61], whereas in plastic vortex creep according to (3-35) the dependence must be decreasing.

In a numerical study by Schönenberger *et al.* plastic deformation of a 3D vortex lattice driven through a disorder potential with mutually distant, strong pinning centres has been generated dynamically[62]. In this approach the pinning centres are considered to have a tubelike shape with a transverse size of the order of the coherence length ξ and a variable longitudinal size within the range l_p from ξ to fa_o (that is, a few lattice constants) along the field direction. This approach can be applied to both correlated disorder (such as columnar defects created by irradiation and embedded carbon nanotubes within a sample matrix) and point disorder. For instance, the point-like and correlated pinning centres are described by $l_p = 3\xi$ and $l_p \leq 7a_o$, respectively. A dynamically produced defects study of Schönenberger *et al.*[62] in a 3D vortex lattice a finite pinning barrier and the field dependence of the critical current density as

$$U(J) = U_c \left(\frac{J_c - J}{J_c} \right)^{\beta} , \qquad (3\text{-}37)$$

$J_c \propto H^{-1}$ for point pinning,

$J_c \propto H^{-0.7 \pm 0.1}$ for correlated pinning (3- 38)

were obtained for both strong point pinning and correlated pinning, with $\beta \approx 1.97$ and 2 for point and correlated pinning, respectively.

Besides the plastic vortex creep regime there are a few other interesting features in the vortex solid phase which are worthy of study, and they have attracted massive attention within the last few years[58,63-68] especially for the interpretation of the *Peak Effect*. In what follows an attempt is made to review the latest theories and the models that deal with the mixed state in the *H-T* phase diagram. Now it is time to have a broader insight into the entire solid phase in the *H-T* phase diagram. In order to have a quantified insight on plastic deformation and creep that allows comparison with elastic deformation, the theory of *Dislocation Mediated Plastic Vortex Creep* (DMPVC) is briefly reviewed[69,70]. Since the theory involves rigorous advanced calculations, the review is restricted to its main hallmarks, which are necessary for the discussion in Chapter six. Experimental observations could have been the source of inspiration for this theory:

A vortex lattice close to the ideal Abrikosov vortex lattice has been observed in clean BiSCCO systems at small fields of less than 100 Oe by decorations, neutron diffraction, and Lorentz microscopy [71-73]. At higher field, however, this perfect ordered quasi-lattice has never been seen. Muon-spin-resonance experiments give experimental evidence for the existence of two vortex solid phases with different positional correlations [74]. The reason is that at elevated magnetic fields the action of disorder, which destroys the vortex lattice, is promoted. It has been shown that in the presence of rather weak disorder the vortex line lattice retains a quasi-long-range order resulting in a new phase, which is known as the

Bragg Glass phase[75]. However, with an increase in random pinning strength or magnetic field a transition to a strongly disordered entangled vortex phase (Amorphous Vortex Glass phase) is predicted.

In DMPVC theory a unified description of the vortex lattice phase in terms of the (disorder induced) proliferation of dislocations in vortex lattice is considered as the leading mechanism for all phase transitions between vortex lattice phases [69,70]. In this picture, the phase diagram comprises the following phases: There exists a dislocation-free phase with long-range translational order at low fields known as the (quasi-lattice) Bragg Glass. This phase undergoes a first-order melting transition at high temperatures and fields lower than the field corresponding to the so-called *endpoint* or *multi-critical point* (see Figure 3-1). For fields above the endpoint the vortex system proceeds through a weak first-order transition [76] to the Amorphous Vortex Glass phase where the translational order is maintained only locally. This transition is due to the proliferation of dislocations (topological defects) in the vortex lattice. A further increase in the magnetic field leads to the intense proliferation of dislocations, so that the vortex lattice is saturated by their presence and therefore the vortex system ends in the liquid phase below the upper critical field H_{c2}. In other words, every phase is assigned to a specific value of density (or spacing) of dislocations.

For instance, in the 3D Bragg Glass phase (in contrast to the 2D case), which is shown to be stable with respect to dislocation formation [77,78] and therefore is dislocation-free, the dislocation spacing is $R_d = \infty$, for the liquid phase $R_d = a_o$ and for the amorphous vortex glass phase $R_d = R_a$ where R_a is called positional correlation length corresponding to the vortex line displacement $u \simeq a_o$ (known as the *Random Manifold* regime). In this approach then, a free energy for an ensemble of directed dislocations in the presence of the quenched

and thermal disorder is derived, and all subsequent local minima of this function would correspond to the above-mentioned phases.

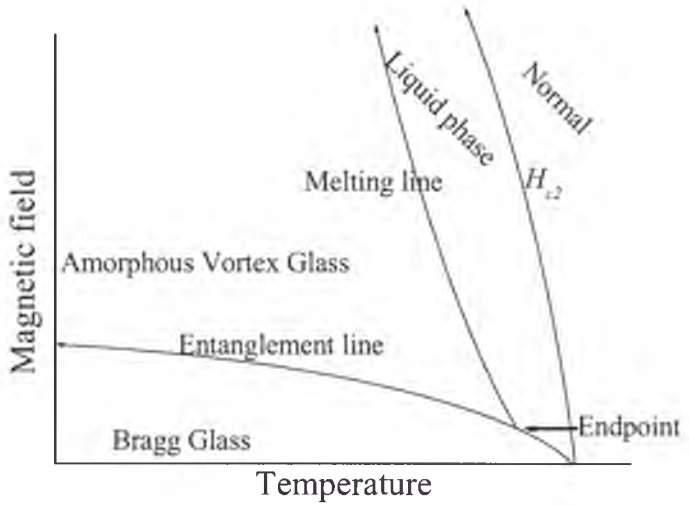

Figure 3- 1 A Schematic phase diagram including the Bragg Glass phase, which undergoes a first order melting at high temperature below the endpoint, and an Amorphous Vortex Glass phase in addition to the liquid and normal phases (not to scale).

Theoretical investigation of plastic vortex creep in this topologically disordered system has been done by Kierfeld *et al.*[70]. An interesting point is that the same diverging potential barrier form as the collective vortex creep barrier (equation (3-32)) is obtained from their calculations. However, there are some differences. In this approach, in contrast to elastic vortex creep theory, current density is a decreasing function of magnetic field. Furthermore, the *critical plastic current* J_{pl} in the single dislocation regime is smaller than the single vortex depinning current J_c (section 3.2.3), which means that despite having pinned vortices, the plastic motion of dislocations is possible, and at sufficient currents it could dominate transport in the dislocated amorphous vortex glass state. The other difference is that the creep rates in plastic vortex creep in different regimes are lower than their counterpart in collective vortex creep theory. For example, the critical exponents in the

Random Manifold and Bragg Glass regimes are $\mu_{pl} = 17/11$ and 1, respectively, which both are larger than the elastic single vortex creep regime with an exponent of 1/7. At higher field where we encounter an ensemble of interacting dislocations (dislocation bundle) the exponents obtained are $\mu_{pl} = 10/21$ and 2/5 for the random manifold and Bragg Glass regimes, respectively. When the dislocation spacing is of the same order as the vortex lattice spacing, $R_d = a_o$, a crossover from single dislocations to bundle dislocations may happen at currents $J < J_{pl}$ [70].

In a phenomenological approach taken by Ertas *et al.*[79] and Vinokur *et al.*[80] the vortex solid phase in the presence of random weak disorder is divided into an almost "ordered phase" at low fields (that is, at fields smaller than the "decoupling field" in layered superconductors, but high enough that the vortex lattice spacing $a_o \leq \lambda$) and an "entangled-solid phase". In this approach the interaction of a vortex with a neighbouring vortex is approximated by a quadratic simple harmonic potential well. Following that, the Lindemann criterion is employed to obtain all the phases in Figure (3-1). According to the Lindemann criterion in this context, when the transverse displacement of a vortex becomes equal to a certain fraction of the vortex lattice spacing, $u \sim c a_o$ (where $c \approx 0.1$-0.2), a phase transition occurs. That is, in this approach the Lindemann criterion comprises a broader meaning than what was thought before. This criterion not only represents the increase in thermal entanglement of a vortex system, but it also represents the increase in mechanical entanglement in the vortex system. Thus, the melting and entanglement (or order-disorder) transition lines in this approach can be found by the criterion of equality between pairs of energies, with the pairs selected among elastic energy, E_{el}, pinning energy, E_{pin}, and thermal energy, E_{th}. For example, melting would be the result of equality between thermal energy

and elastic energy. That is, when the thermal fluctuation energy become equal to the elastic energy barriers which keep vortices in their equilibrium position in the ordered phase, $E_{th}=E_{el}$, the vortex system starts melting. Likewise, the entanglement line is the result of competition between pinning and elastic energy, $E_{pin}=E_{el}$, and the melting line from entangled-solid phase emerges from competition between pinning energy and thermal energy, $E_{pin}=E_{th}$.

A single vortex with length L, as an elastic object under the action of random point disorder, follows a rough path which is determined by taking some statistical mechanic averages over the thermal and quenched disorder[2]

$$u(L)=\left\langle|\mathbf{u}(L)-\mathbf{u}(0)|^2\right\rangle^{1/2}\approx\xi(L/L_c)^{\zeta}, \qquad (3\text{-}39)$$

where the roughness (or wandering) exponent ζ=3/5 for this regime and $L_c=(\Gamma^4\varepsilon_o^2\xi^2/\gamma)^{1/3}$ is the collective pinning length. As before, Γ is the anisotropy parameter, ε_o is the vortex line tension and γ is the disorder parameter. The characteristic pinning energy for the single vortex regime is

$$E_{pin}(L)=U_c(L/L_c)^{2\zeta-1}, \qquad \text{for } L>L_c \qquad (3\text{-}40)$$

where $U_c=(\gamma\Gamma^2\varepsilon_o\xi^2)^{1/3}$ is the collective pinning energy.

Using the simple harmonic potential well approximation the elastic energy is obtained to be

$$E_{el}=C_{66}u^2L+\Gamma^2\varepsilon_o(u^2/L), \qquad (3\text{-}41)$$

where u and L are the transverse and longitudinal sizes of the vortex distortion, respectively, and $C_{66}=\varepsilon_o/4a_o^2$ is the vortex lattice shear modulus. Indeed, with the above-mentioned approximation we confine a vortex within a cell or "cage". The characteristic

longitudinal size of this cell can be calculated by minimizing the elastic energy with respect to L. As a result we obtain the length as

$$L_o=(\Gamma^2\varepsilon_o/C_{66})^{1/2}\simeq 2\Gamma a_o \,. \qquad (3\text{-}42)$$

This is the size of an independent distorted cell. The elastic energy corresponding to this length is $E_{el}=\Gamma\varepsilon_o u^2/a_o$. Near the order-disorder transition line we expect $u^2=c^2a_o^2$, and hence

$$E_{el}=\Gamma\varepsilon_o c^2 a_o \,. \qquad (3\text{-}43)$$

For the case where $L_c < L_o$ the solid entanglement line is obtained by equating two expressions for pinning and elastic energy in equations (3-40) and (3-43), giving the result that[80]

$$H_{en}=H_o(U_o/U_c)^{2\zeta/(1-\zeta)} \,, \qquad (3\text{-}44)$$

provided that $d < L_c < L_o$, where d is the interlayer spacing. Furthermore, $H_o=c^2\Phi_o/\xi^2$, $U_o=c\Gamma\varepsilon_o\xi/2$.

3.2.7 Peak Effect

We saw in previous section that the phase diagram of a high-temperature superconductor is very rich and complicated, having different phases that must be explained on the basis of the interplay between three basic energy scales, the vortex elastic energy (E_{el}), thermal fluctuation energy (E_{th}), and pinning energy (E_{pin}). One long standing topic in the vortex dynamics of high-temperature superconductors is the physical mechanism underlying the anomalous increase of magnetization with increasing magnetic field applied parallel to the c axis above the lower critical field H_{c1}, the so called peak effect or fishtail effect. This effect is characterized by a rising J_c with H at onset field H_{on} far above the lower critical field H_{c1}. Contrary to the peak effect observed in conventional

low-T_c superconductors, which occurs in the vicinity of the upper critical field H_{c2}, the peak effect of high-T_c superconductors occurs well below H_{c2}. Over the last decade overwhelming efforts have be dedicated to finding the mechanism involved in the appearance of the peak effect in high-T_c superconductors, and many models have been proposed to explain this phenomenon. For example, in one model the authors propose that the matching effect is responsible for the appearance of the peak effect[81]. That is, when the vortex lattice matches the impurity structure, we would have maximum pinning. At low fields, when the pinning centres are denser than the vortices, the vortices have more freedom to move, and more energetically desirable positions are available to accommodate them. However, at higher field the vortex spacing equals the mean distance between the pinning centres, and the number of available positions for the vortices is less than in the low-field case, which leads to enhanced pinning.

In other experimental research[82], the formation of a percolation-like reversible network associated with suppression of the order parameter with increasing field in oxygen deficient sites (and therefore variation of oxygen deficiency) has been found to be the leading source for the formation of the peak effect and to determine its location.

An alternative source of the peak effect is believed to be dimensional crossover from 3D to 2D in vortex systems[83]. Such a change should appear if the elastic shear energy within the planes becomes equal to the tilt energy between the planes. In that case theory[11] predicts $H_{cr} \sim \phi_0 \Gamma^2 / d^2$ for the crossover field, where Γ is the anisotropy parameter and d is is the distance between CuO planes.

A transition from disorder-induced Bragg Glass at low field to the highly entangled Amorphous Vortex Glass[84-86] phase has been recently widely accepted as a strong source

of the peak effect. Starting from the low-field and low-temperature part of the phase diagram, according to this approach the rate of decay in elastic energy is faster than in pinning energy with increasing field[80], so that on approaching the entanglement line, the pinning energy become comparable with the elastic energy. A further increase in the magnetic field promotes the effectiveness of the pinning sites and consequently magnetization (or current density) increases. Any further increase of magnetic field beyond this point yields the entanglement of vortices, and permutation of vortices takes place. As a result dislocation pairs and distorted elastic cells (mentioned in the previous section) will form. On progressively increasing the applied field the density of dislocations would become denser and vortices cross each other at a larger angle, which makes the vortex cutting process easier, causing the critical current density to start dropping. Several experiments have been already reported that imply the existence of a crossover from the elastic vortex glass phase to plastically deformed vortex creep across the peak effect[55,58,87-89].

In an experimentally-based model[90], the coexistence of two distinctive phases of vortex matter with different pinning strengths on a macroscopic scale is believed to be responsible for the occurrence of the peak effect. That is, the peak effect originates from the transformation from one phase to another phase with temperature or field variation[90]. This transition can be called the "weak to strong pinning crossover"[91] and originates from the reduction of the elasticity of vortex lattice with increasing field. That is, at low field, while a vortex lattice with large elasticity can exploit the collective attraction of many weak pinning disorders, at high field with smaller elasticity it can be pinned by the action of a few strong pinning disorders[91].

3.3 Correlated disorder: Lock-in angle determination in a twinned single crystal

Whereas in the previous sections we dealt with the phenomena that originate from weak point-like pins (uncorrelated disorder), this section is dedicated to the pinning properties of extended defects, and in particular twin planes. Whereas in the presence of randomly distributed point defects a transition from a vortex fluid to a vortex glass is expected with decreasing temperature, in the case of extended defects the low temperature phase is expected to be a Bose-glass phase [92]. Although all real materials contain point disorder, their effects can be overshadowed in some circumstances by the effects of extended disorder. The main reason is that the pinning forces of random point pins are superposed incoherently, whereas the extended pinning sites exert forces on vortices coherently. One can then expect that current density grows when flux lines lie in extended defects. The drop in resistivity in a twinned YBCO single crystal [93-95] when flux lines are aligned with the twin plane is experimental evidence for the coherent action of extended pinning defects. However, in the presence of strong point disorder, extended defects may become irrelevant, and therefore the low temperature phase will be dominated by point defects [96] (vortex-glass phase).

Experimental studies of vortex dynamics and critical current measurements in crystals with twin planes directly show their significant contribution to the Abrikosov vortex pinning. Depending on the strength of point pinning sites and the concentration of twin planes, each of these pinning sources can mask the influence of the other one. Twin boundaries are an example of planar disorder that is generally present in superconducting $REBa_2Cu_3O_{7-x}$ (where RE = Y, Sm, Nd, Eu) [97-100] systems, where they are needed to

accommodate the strains produced by a crystallographic tetragonal-to-orthorhombic transition. Twins most often occur in two orthogonal families of lamellas that form a mosaic. In fact, the influence of a twin plane is two-fold, with the influences having an opposite impact on the significant pinning issues. On the one hand, due to settlement of the order parameter along the twin plane and therefore elongation of the coherence length, pinning is reduced[101]. However, due to entrapment of the vortex line within the twin potential well the dimension of thermal fluctuation decreases from 3D to 2D, which is in favour of pinning enhancement[102,103]. Since correlated disorder promotes vortex line delocalisation (for magnetic field along the disorder), and point disorder promotes vortex line wandering, the dominant defect structure can be identified by changing the angle between the applied field and the correlated disorder. The theory [2,104] predicts that at a small tilting angle, known as the *lock-in* angle φ_L (around a few degree for twins), vortices are locked into the twin planes. In this range shielding currents should be independent of angle φ.

In the presence of correlated disorder, the vortex glass transition into the vortex liquid is modified and shifted towards higher field in the phase diagram. In this case, a Bose glass transition or a two-dimensional melting with cusp-like dependence of the irreversibility line at H parallel to the c-axis is predicted. Therefore, the angular dependence of the irreversibility line and of the current is one of the most useful tools to discriminate between different pinning mechanisms. Isotropic uncorrelated disorder like oxygen vacancies produces a current density with a smooth angular dependence connected with the intrinsic anisotropy of the superconductor [105], whereas a very sharp variation in the angular dependence of the irreversible field is expected from the correlation disorder produced by

twin planes. This sharp angular dependence of H_{irr} has been the principal method used to study the locking of magnetic vortices by twin planes and the determination of φ_L. However, due to the high irreversibility field of RE(123) systems, such measurements could be conducted only at high temperatures, close to T_c, at which the irreversibility field is subject to a high degree of uncertainty. Further, H_{irr} is defined by an arbitrary value of magnetization, at which the ascending and descending branches of the magnetic hysteresis loop, or the zero-field cooled and field-cooled branches of the temperature dependence of the magnetization, are seen to merge. Because of this, it is highly desirable to develop a new method for obtaining φ_L that relies on universal physical principles instead of arbitrary definitions. Such a method is presented in this thesis. This method was developed for an off-stoichiometric Sm123 single crystal, and it is based on the scaling of hysteresis loops measured at different angles with respect to the crystalline c-axis.

Since the investigation of vortex dynamics of twinned HTSs such as RE(123) systems is always complicated by some intrinsic anisotropic properties related to their layered structure, the treatment of these systems must be conducted with care. In order that these intrinsic properties not interfere with the effects of twin planes, their effect must be taken into account. For this purpose, the Blatter's [106] approach (section 3.5) is usually employed.

3.4 Experimental Determination of U(J)

The decay or relaxation of magnetization in HTSs can be mapped onto potential barriers, which can describe the type and the strength of pinning mechanisms. It must be noted that this decay just comes from the irreversible component of the magnetization M_{irr} in the superconductor. Magnetic relaxation can be revealed in both dc and ac

measurements. For example, in dc measurements, the sweep-rate dependence of the width of the hysteresis loop and the time dependence of the magnetic moment during relaxation hold the same type of information [107,108], and from both measurements the activation energy can be extracted [109-112]. As well as from dc measurements, the activation energy can be determined from the frequency dependence of the imaginary part of the ac-susceptibility [49,113]. Since in this work the so-called Maley method developed by Maley et al. [114] and McHenry et al. [114,115] on dc magnetization relaxation data is applied, it is briefly explained. The Maley method is based on the following expression for $U_{eff}(J)$

$$U_{eff}(J) = -k_B T \ln\left|\frac{dM_{irr}}{dt}\right| + k_B T \ln\left(\frac{Hx_o\omega}{d\pi}\right), \qquad (3\text{-}45)$$

where l is the thickness of the sample, x_o is the flux bundle hopping distance and ω is the attempt frequency. In this approach, first $T \ln|dM_{irr}/dt|$ at a given field is calculated. Then this data can be plotted against M_{irr} at different temperatures. Finally, by adjusting the constant $C = \ln(Hx_o\omega/l\pi)$ all data can be made to form an almost smooth curve. Further temperature scaling leads to a perfect smoothness of the curve [112,116,117], and in this way U–M_{irr} (or equivalently U–J), as well as the U–T relation, are obtained. However, the Maley method is based on assumptions about the temperature dependence of the characteristic current and energy scales.

3.5 Anisotropy of magnetic moment in HTSs

High-temperature superconductors are highly anisotropic and show a rich variety of behaviours in their magnetic and electric properties. Magnetic moment (or critical current density), for instance, has a strong dependence on the orientation of the magnetic field with respect to the crystal axis. The anisotropy is mainly introduced in the form of mass

anisotropy in equation (3-1). In order to determine a superconductor's properties such as the elastic properties of the vortex lattice, vortex lattice melting or depinning, and the investigation of pinning and creep, this equation must be solved. Whereas an analytical solution of this equation is a very difficult task, Blatter's scaling rule [106] maps the uniaxial anisotropic problem onto an isotropic problem which has been already solved to a broad extent. In this way the isotropic results are generalized to the anisotropic case. As a result of this scaling approach, for instance, the single vortex collective pinning length, L_c^{iso}, and pinning energy, U_c^{iso}, for the isotropic situation [both defined in section (3.2.3)] are modified into

$$L_c(\varphi) \simeq \left[\frac{\varepsilon_o^2 \xi^2 \Gamma^4}{\gamma}\right]^{1/3} / \varepsilon(\varphi) = \Gamma^{4/3} L_c^{iso} / \varepsilon(\varphi), \qquad (3\text{-}46)$$

$$U_c \simeq \Gamma^{2/3} U_c^{iso}, \qquad (3\text{-}47)$$

where $\varepsilon(\varphi) = (\Gamma^2 \sin^2\varphi + \cos^2\varphi)^{1/2}$ is a temperature-independent scaling parameter and φ is the angle between the magnetic field and the crystallographic *c*-axis. This approach is applicable to layered superconductors, provided that there is no concern about decoupling the layers. For a highly anisotropic superconductor, such as Bi2212, taking the Lawrence and Doniach (LD) approach (section 3.2.1) is more reliable. Furthermore, this approach is restricted to the single vortex and small bundle regimes.

For both the continuous anisotropic GL and discrete LD models, the main idea is that the anisotropy-dependent observables, such as critical current density, are scaled in the tilted magnetic field (for samples without twin planes and for angles outside the trapping angle of CuO planes) by the scaling parameter $\varepsilon(\varphi)$ with respect to their measured parallel

counterparts (i.e. $\varphi = 0°$). This may not be the case for samples with strong twinning planes. This is because for angles within the lock-in angle range, twin planes have the major contribution in determining the screening current density, which hasn't been considered in the above-mentioned scaling approach. For example, for a de-twinned YBCO crystal, Klein et al. show that the angular dependence of Δm ($\propto J$) is determined by the *c*-axis component[105]. However, Küpfer et al. show that this dependency does not occur in an Y(123) crystal with twinning planes due to the effect of the correlated disorder.

Although in Blatter's scaling approach only isotropic disorder is taken into account, the scaling of Δm ($\propto J$) according to their approach could provide us with some information about the angular extent of the efficiency of correlated disorder within the *H-T* phase diagram. That is, the effect of correlated disorder can be identified through a deviation from the scaling behavior for isotropic scaling. As a consequence of this approach, for instance, the irreversibility line is written as [106,118,119]

$$H_{irr}(T, \varphi) = H_{irr}(T, \varphi = 0)/\varepsilon(\varphi) . \qquad (3\text{-}48)$$

For a highly anisotropic system like Bi2212 with $\Gamma^{-1} \simeq 150$ [3], where $\varepsilon(\varphi) \approx \cos\varphi$, the above equation is approximated by $H_{irr}(T, \varphi) = H_{irr}(T, \varphi = 0)/\cos\varphi$.

Thus, the scaled magnetic moment $m/\cos\varphi$ when plotted against the normal component of the applied field, i.e. $H\cos\varphi$, should scale onto a single curve irrespective of the presence of any peak-effect (except for φ very close to 0° or 90°).

References:

1 D. J. Bishop, P. L. Gammel, D. A. Huse, and C. A. Murray, Science **255,** 165 (1992).

2 G. Blatter, M. V. Feigel'man, V. B. Geshkenbein, A. I. Larkin, and V. M. Vinokur, Rev. Mod. Phys. **66,** 1125 (1994).

3 J. C. Martinez, S. H. Brongersma, A. E. Koshelev, B. Ivlev, P. H. Kes, R. P. Griessen, D. G. Groot, Z. Tarnawski, and A. A. Menovsky, Phys. Rev. Lett. **69,** 2276 (1992).

4 U. Welp, W. K. Kwok, G. W. Crabtree, K. G. Vandervoort, and J. Z. Liu, Phys. Rev. Lett **62,** 1908 (1989).

5 D. E. Farrell, C. M. Williams, S. A. Wolf, N. P. Bansal, and V. G. Kogan, Phys. Rev. Lett **61,** 2805 (1988).

6 M. Xu, H. Kitazawa, Y. Takano, J. Ye, K. Nishida, H. Abe, A. Matsushita, and N. Tsuji, Phys. Rev. Lett **79,** 2779 (2001).

7 L. Lyard, P. Samuely, P. Szabo, T. Klein, C. Marcenat, L. Paulius, K. H. P. Kim, C. U. Jung, H.-S. Lee, and B. Kang, Phys. Rev. B **66,** 180502-1 (2002).

8 J. R. Clem, Phys. Rev. B **43,** 7837 (1991).

9 W. E. Lawrence and S. Doniach, Kyoto, 1971 (Proceedings of the 12th International Conference on Low Temperature Physics, Academic Press of Japan, Kyoto), p. 361.

10 A. Dulcic, M. Pozek, D. Paar, E. M. Choi, H. J. Kim, W. N. Kang, and S. I. Lee, Physica C **408,** 662 (2004).

11 L. I. Glazman and A. E. Koshelev, Phys. Rev. B **43,** 2835 (1991).

12 J. Pearl, Appl. Phys. Lett. **5,** 65 (1964).

13 M. V. Feigel'man, V. B. Geshkenbein, and V. M. Vinokur, JETP. Lett. **52,** 546 (1990).

14 J. R. Clem, M. W. Coffey, and Z. Hao, Phys. Rev. B **44,** 2732 (1991).

15 M. V. Feigel'man, V. B. Geshkenbein, and V. M. Vinokur, Physica C **167,** 177 (1990).

16 L. N. Bulaevskii, M. Ledvij, and V. G. Kogan, Phys. Rev. B **46,** 366 (1992).

17 E. H. Brandt, Rep. Progr. Phys. **58,** 1465 (1995).

18 C. P. Bean and J. D. Livingston, Phys. Rev. Lett **12,** 14 (1964).

19 M. Xu, D. K. Finnemore, G. W. Crabtree, V. M. Vinokur, B. Dabrowski, D. G. Hinks, and K. Zhang, Phys. Rev. B **48,** 10630 (1993).

20 A. M. Campbell and J. E. Evetts, Adv. Phys. **21,** 199 (1972).

21 L. Burlachkov, Phys. Rev. B **47,** 8056 (1993).

22 L. Burlachkov, Physica C **209,** 203 (1993).

23 N. Morozov, E. Zeldov, M. Konczykowaski, and R. A. Doyle, Physica C **291,** 113 (1997).

24 R. A. Doyle, S. F. W. R. Rycroft, C. D. Dewhurst, E. Zeldov, I. Tsabba, S. Reich, T. B. Doyle, T. Tamegai, and S. Ooi, Physica C **308,** 123 (1998).

25 E. Zeldov, A. I. Larkin, V. B. Geshkenbein, M. Konczykowaski, D. Majer, B. Khaykovich, V. M. Vinokur, and H. Shtrikman, Phys. Rev. Lett **73,** 1428 (1994).

26 A. A. Elistratov, O. A. Bobrikov, and I. L. Maksimov, Mod. Phys. Lett. B **18,** 19 (2004).

27 Z. W. Lin, G. D. Gu, and G. J. Russell, Supercond. Sci. Technol. **13,** 1170 (2000).

28 A. Fortini and E. Paumier, Phys. Rev. B **14,** 55 (1976).

[29] L. Cabral, R. E., C. C. de Souza, E. H. Brandt, and J. Albino Aguiar, Physica C **369,** 196 (2002).

[30] P. W. Anderson, Phys. Rev. Lett. **9,** 309 (1962).

[31] P. W. Anderson and Y. B. Kim, Rev. Mod. Phys. **36,** 39 (1964).

[32] M. R. Beasley, R. Labusch, and W. W. Webb, Phys. Rev. **181,** 682 (1969).

[33] M. V. Feigel'man, V. B. Geshkenbein, and V. M. Vinokur, Phys. Rev. B **43,** 6263 (1991).

[34] V. M. Vinokur, M. V. Feigel'man, and V. B. Geshkenbein, Phys. Rev. Lett **67,** 915 (1991).

[35] V. B. Geshkenbein and A. I. Larkin, Sov. Phys. JETP **68,** 639 (1989).

[36] Y. Yeshurun and A. P. Malozemoff, Phys. Rev. Lett. **60,** 2202 (1988).

[37] Y. Yeshurun, A. P. Malozemoff, F. H. Holtzberg, and T. R. Dinger, Phys. Rev. B **38,** 11 828 (1988).

[38] A. I. Larkin and Y. N. Ovchinnikov, J. Low Temp. Phys. **34,** 409 (1979).

[39] M. V. Feigel'man, V. B. Geshkenbein, A. I. Larkin, and V. M. Vinokur, Phys. Rev. Lett. **63,** 2303 (1989).

[40] T. Halpin-Healy, Phys. Rev. Lett **62,** 442 (1989).

[41] E. Zeldov, N. M. Amer, G. Koren, A. Gupta, R. J. Gambino, and M. W. McElfresh, Phys. Rev. Lett **62,** 3093 (1989).

[42] R. Hergt and R. Hiergeist, Phys. Rev. B **47,** 5405 (1993).

[43] V. M. Vinokur, P. H. Kes, and A. E. Koshelev, Physica C **248,** 179 (1995).

[44] A. P. Malozemoff and M. Fisher, P.A., Phys. Rev. B **42,** 6784 (1990).

[45] T. Nattermann, Phys. Rev. Lett **64,** 2454 (1990).

[46] M. Fisher, P.A., Phys. Rev. Lett **62,** 1415 (1989).

[47] L. F. Cohen and H. J. Jensen, Rep. Prog. Phys. **60,** 1581 (1997).

[48] D. S. Fisher, M. Fisher, P.A., and D. A. Huse, Phys. Rev. B **43,** 130 (1991).

[49] C. J. van der Beek and P. H. Kes, Phys. Rev. B **43,** 13032 (1991).

[50] V. B. Geshkenbein, A. I. Larkin, M. V. Feigel'man, and V. M. Vinokur, Physica C **162,** 239 (1989).

[51] V. M. Vinokur, P. H. Kes, and A. E. Koshelev, Physica (Amsterdam) **168C,** 29 (1990).

[52] S. Bhattacharya and M. J. Higgins, Phys. Rev. B **41,** 6394 (1994).

[53] H. Safar, P. L. Gammeg, D. A. Huse, G. B. Alers, D. J. Bishop, W. C. Lee, J. Giapintzakis, and D. M. Ginsberg, Phys. Rev. B **52** (1995).

[54] W. K. Kwok and J. A. Fendrich, Phys. Rev. Lett. **73,** 2614 (1994).

[55] Y. Abulafia, A. Shaulov, Y. Wolfus, R. Prozorov, L. Burlachkov, Y. Yeshurun, E. Zeldov, V. M. Vinokur, J. L. Peng, and R. L. Greene, Phys. Rev. Lett. **77,** 1596 (1996).

[56] Y. P. Sun, W. H. Song, J. J. Du, and H. C. Ku, Phys. Rev. B **66,** 104520 (2002).

[57] P. Chowdhury, H. J. Kim, W. N. Kang, D. J. Zang, S. I. Lee, and D. H. Kim, Phys. Rev. B **68,** 134413 (2003).

[58] D. Giller, A. Shaulov, R. Prozorov, Y. Abulafia, Y. Wolfus, L. Burlachkov, Y. Yeshurun, E. Zeldov, V. M. Vinokur, J. L. Peng, and R. L. Greene, Phys. Rev. Lett **79,** 2542 (1997).

[59] J. P. Hirth and J. Lothe, *Theory of Dislocations* (John Wiley & Sons, New York, 1982).

[60] G. K. Perkins and F. Cohen, Phy. Rev. B **51,** 8513 (1995).

[61] A. A. Zhukov, H. Küpfer, G. Perkins, L. F. Cohen, A. D. Caplin, S. A. Klestov, H. Claus, V. I. Voronkova, T. Wolf, and H. Wühl, Phys. Rev. B **51,** 12704 (1995).

[62] A. Schönenberger, A. Larkin, E. Heeb, V. Geshkenbein, and G. Blatter, Phys. Rev. Lett **77,** 4636 (1996).

[63] T. Giamarchi and P. Le Doussal, Phys. Rev. Lett **72,** 1530 (1994).

[64] D. S. Fisher, Phys. Rev. Lett **78,** 1964 (1997).

[65] M. Baziljevich, D. Giller, M. McElfresh, Y. Abulafia, Y. Radzyner, T. Schneck, T. H. Johansen, and Y. Yeshurun, Phys. Rev. B **62,** 4058 (2000).

[66] H. Küpfer, T. Wolf, R. Meier-Himer, and A. A. Zhukov, Physica C **332,** 80 (2000).

[67] V. F. Correa, J. A. Herbsommer, E. E. Kaul, F. de la Cruz, and G. Nieva, Phys. Rev. B **63,** 92502-1 (2001).

[68] S. R. Park, S. M. Choi, D. C. Dender, J. W. Lynn, and X. S. Ling, Phys. Rev. Lett. **91,** 167003-1 (2003).

[69] J. Kierfeld and V. M. Vinokur, Phys. Rev. B **61,** R14928 (2000).

[70] J. Kierfeld, H. Nordborg, and V. M. Vinokur, Phys. Rev. Lett. **85,** 4948 (2000).

[71] R. N. Kleiman, P. L. Gammel, L. F. Schneemeyer, J. V. Waszczak, and D. J. Bishop, Phys. Rev. Lett **62,** 2331 (1989).

[72] R. Cubitt, E. M. Forgan, G.-W. Yang, S. L. Lee, D. M. Paul, H. A. Mook, M. Yethiraj, P. H. Kes, T. W. Li, A. A. Menovsky, Z. Tarnawski, and K. Mortensen, Nature (London) **365,** 407 (1993).

[73] K. Harada, T. Matsuda, H. Kasai, J. E. Bonevich, T. Yoshida, U. Kawabe, and A. Tonomura, Phys. Rev. Lett. **71,** 3371 (1993).

74 S. L. Lee, P. Zimmermann, H. Keller, M. Warden, I. M. Savic, R. Schauwecker, D. Zech, R. Cubitt, E. M. Forgan, P. H. Kes, T. N. Li, A. A. Menovsky, and Z. Tarnawski, Phys. Rev. Lett **71,** 3862 (1993).

75 T. Giamarchi and P. Le Doussal, Phys. Rev. B **52,** 1242 (1995).

76 C. J. van der Beek, S. Colson, M. V. Indenbom, and M. Konczykowaski, Phys. Rev. Lett **84,** 4196 (2000).

77 J. Kierfeld, T. Nattermann, and T. Hwa, Phys. Rev. B **55,** 626 (1997).

78 D. S. Fisher, Phys. Rev. Lett. **78,** 1964 (1997).

79 D. Ertas and D. R. Nelson, Physica C **272,** 79 (1996).

80 V. M. Vinokur, B. Khaykovich, E. Zeldov, M. Konczykowaski, R. A. Doyle, and P. H. Kes, Physica C **295,** 209 (1998).

81 G. Yang, P. Shang, S. D. Sutton, I. P. Jones, J. S. Abell, and C. E. Gough, Phys. Rev. B **48,** 4054 (1993).

82 M. Däumling, J. M. Seuntjens, and D. C. Larbalestier, Nature **346,** 332 (1990).

83 A. K. Pradhan, S. B. Roy, P. Chaddah, C. Chen, and B. M. Wanklyn, Phys. Rev. B **49,** 12984 (1994).

84 B. Khaykovich, M. Konczykowaski, E. Zeldov, R. A. Doyle, D. Majer, P. H. Kes, and T. W. Li, Phys. Rev. B **56,** R517 (1997).

85 T. Klein, I. Joumard, S. Blanchard, J. Marcus, R. Cubitt, T. Giamarchi, and P. Le Doussal, Nature **413,** 404 (2001).

86 U. Divakar, A. J. Drew, S. L. Lee, R. Gilardi, J. Mesot, F. Y. Ogrin, D. Charalambous, E. M. Forgan, G. I. Menon, N. Momono, M. Oda, C. D. Dewhurst, and C. Baines, Phys. Rev. Lett. **92,** 237004-1 (2004).

87 T. Aouaroun, V. Hardy, and C. Simon, Physica C **294,** 42 (1998).

88 S. Kokkaliaris, A. A. Zhukov, P. A. J. de Groot, R. Gagnon, L. Taillefer, and T. Wolf, Phys. Rev. B **61,** 3655 (2000).

89 L. Miu, T. Noji, Y. Koike, E. Cimpoiasu, T. Stein, and C. C. Almasan, Phys. Rev. B **62,** 15172 (2000).

90 M. Marchevsky, M. J. Higgins, and S. Bhattacharya, Phys. Rev. Lett **88,** 087002-1 (2002).

91 G. Blatter, V. B. Geshkenbein, and J. A. G. Koopmann, Phys. Rev. Lett **92,** 7009 (2004).

92 D. R. Nelson and V. M. Vinokur, Phys. Rev. B **48,** 13060 (1993).

93 W. K. Kwok, U. Welp, G. W. Crabtree, K. G. Vandervoort, R. Hulscher, and J. Z. Liu, Phys. Rev. Lett **64,** 966 (1990).

94 W. K. Kwok, U. Welp, V. M. Vinokur, J. Fleshler, J. Downey, and G. W. Crabtree, Phys. Rev. Lett **67,** 390 (1991).

95 J. Figueras, T. Puig, and X. Obradors, Phys. Rev. B **67,** 014503 (2003).

96 T. Hwa, D. R. Nelson, and V. M. Vinokur, Phys. Rev. B **48,** 1167 (1993).

97 H. Kupfer, A. A. Zhukov, A. Will, W. Jahn, R. Meier-Himer, T. Wolf, V. I. Voronkova, M. Klaser, and K. Saito, Phys. Rev. B **54,** 644 (1996).

98 H. Kupfer, T. Wolf, A. A. Zhukov, and R. Meier-Himer, Phys. Rev. B **60,** 7631 (1999).

99 M. Murakami, M. Morita, K. Doe, and K. Miyamoto, Jpn. J. Appl. Phys. **28,** 1189 (1989).

100 M. Nakamura, Y. Yamada, T. Hirayama, Y. Ikuhara, Y. Shiohara, and S. Tanaka, Physica C **259,** 295 (1996).

101 A. Gurevich, Phys. Rev. B **46,** 3187 (1992).

[102] H. Küpfer, A. A. Zhukov, A. Will, W. Jahn, R. Meier-Himer, T. Wolf, V. I. Voronkova, M. Klaser, and K. Saito, Phys. Rev. B **54,** 644 (1996).

[103] A. K. Pradhan, K. Kuroda, B. Chen, and N. Koshizuka, Phys. Rev. B **58,** 9498 (1998).

[104] G. Blatter, J. Rhyner, and V. M. Vinokur, Phys. Rev. B **43,** 7826 (1991).

[105] L. Klein, E. R. Yacoby, Y. Yeshurun, A. Erb, G. Müller–Vogt, V. Breit, and H. Wühl, Phys. Rev. B **49,** 4403 (1994).

[106] G. Blatter, V. B. Geshkenbein, and A. I. Larkin, Phys. Rev. Lett. **68,** 875 (1992).

[107] A. D. Caplin, G. K. Perkins, and L. F. Cohen, Supercond. Sci. Technol. **8,** 1 (1995).

[108] G. K. Perkins, L. F. Cohen, A. A. Zhukov, and A. D. Caplin, Phys. Rev. B **51,** 8513 (1995).

[109] H. G. Schnack and R. Griessen, Phy. Rev. B **48,** 13178 (1993).

[110] H. H. Wen, H. G. Schnack, R. Griessen, B. Dam, and J. Rector, Physica C **241,** 353 (1995).

[111] J. R. Thompson, L. Krusin-Elbaum, L. Civale, G. Blatter, and C. Feild, Phys. Rev. Lett. **78,** 3181 (1997).

[112] S. Keshavarzi, M. J. Qin, S. Soltanian, H. K. Liu, and S. X. Dou, Physica C **408,** 601 (2004).

[113] M. J. Qin, X. L. Wang, S. Soltanian, A. H. Li, H. K. Liu, and S. X. Dou, Phys. Rev. B **64,** 060505 (2001).

[114] M. P. Maley, J. O. Willis, H. Lessure, and M. E. McHenry, Phys. Rev. B **42,** 2639 (1990).

[115] M. E. McHenry, S. Simizu, H. Lessure, M. P. Maley, J. Y. Coulter, I. Tanaka, and H. Kojima, Phys. Rev. B **44,** 7614 (1991).

[116] C. J. van der Beek, P. H. Kes, M. P. Maley, M. J. V. Menken, and A. A. Menovsky, Physica C **195,** 307 (1992).

[117] D. Marinaro, J. Horvat, S. X. Dou, R. Weinstein, and A. Gandini, Phys. Rev. B **68,** 064518 (2003).

[118] D. Zech, S. L. Lee, H. Keller, G. Blatter, B. Janossy, P. H. Kes, T. W. Li, and A. A. Menovsky, Phys. Rev. B **52,** 6913 (1995).

[119] K. H. Bennemann and J. B. Ketterson, *The Physics of Superconductors*, Vol. II (Springer-Verlag, Berlin, 2004).

CHAPTER FOUR: EXPERIMENTAL PROCEDURE AND SAMPLE CHARACTERIZATION

4.1 DC Magnetization Measurement

Two magnetometers were employed to measure the DC magnetic moment of the samples, depending on the required applied magnetic field. They were a Physical Property Measurement System (PPMS-9T) and a Quantum Design Magnetic Property Measurement System (MPMS-5T) [Figure 4.1].

Figure 4. 1 Quantum Design Magnetic Property Measurement System (MPMS-5T): left part comprise the sample chamber and right part includes the control system.

In MPMS the magnetic moment of the sample is not detected directly. Instead, the sample moves through a system of superconducting detection coils, which are connected to the Superconducting Quantum Interference Device (SQUID) with superconducting wires, allowing the current from the detection coils to inductively couple to the SQUID sensor. (The configuration is shown in Figure 4.2) The SQUID electronics produce an output voltage, which is strictly proportional to the current flowing in the SQUID input coil. Hence, the thin film SQUID device, which is below the magnet inside a superconducting shield, essentially functions as an extremely sensitive current-to-voltage converter. A measurement is performed in the MPMS by moving a sample through the superconducting detection coils [inset of Figure (4.2)]. As the sample moves through the coils, the magnetic

moment of the sample induces an electric current in the detection coils. Because the detection coils, the connecting wires, and the SQUID input coil form a closed superconducting loop, any change of magnetic flux in the detection coils produces a change in the persistent current in the detection circuit, which is proportional to the change in magnetic flux.

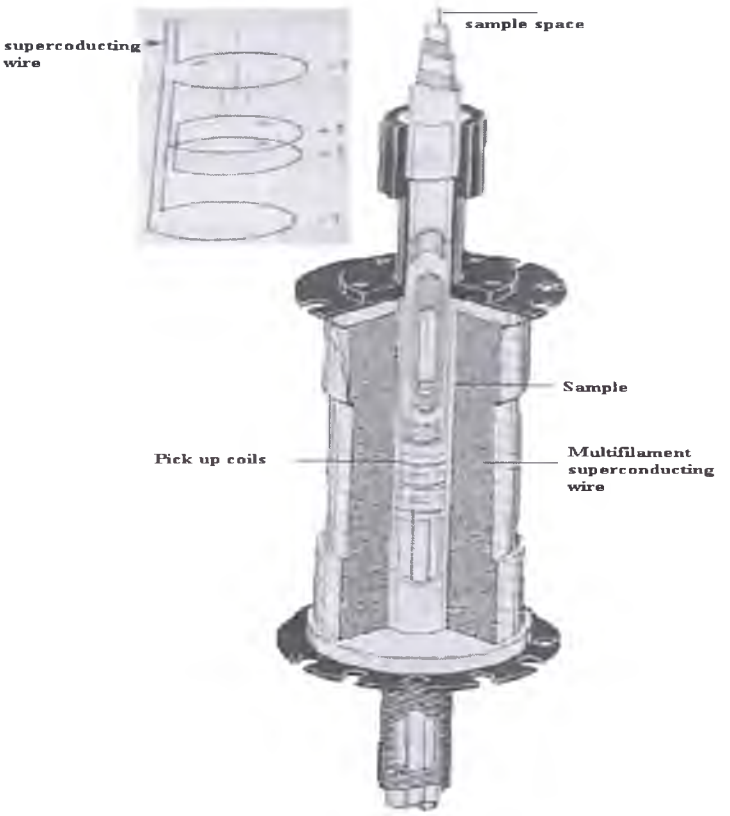

Figure 4. 2 Space and pick up coil locations in MPMS magnetometer (The figure has been taken from MPMS MultiVu Application User's Manual).

The measurement process starts with mounting the sample in the sample holder, placing it in the sample chamber and centring it in an applied field of about 25-50 Oe.

The temperature dependence of the magnetic moment can be measured either by the zero-field-cooled (ZFC) or the field-cooled (FC) method. In the ZFC method, the sample is cooled down from above its T_c to 5K in zero magnetic field. Magnetic field is then applied

and the magnetic moment of the sample is measured as the sample is warmed up. In the FC method, the magnetic field is applied at temperatures higher than T_c. The magnetic moment of the sample is then measured as the sample is cooled down through its superconducting transition. A typical command sequence used in this kind of measurement is shown in *Appendix B*. The merging point of the ZFC and FC curves defines the irreversible temperature corresponding to the applied field. Because the ZFC and FC curves approach each other gradually, determination of the irreversibility temperature in this way is affected by the resolution of the instrument. To avoid the influence of the resolution on the results, the irreversibility temperature is obtained as the temperature for which the difference between the values of magnetic moment for the ZFC and the FC curves falls just below a certain arbitrarily defined value. However, once defined, the same difference in magnetic moment is used for all the measurements. Such measurements for different applied fields give us a line in the field vs. temperature diagram, which is called the irreversibility line.

In addition, the irreversibility line can be obtained by measuring isothermal magnetic hysteresis loops. The hysteresis loops can be measured by cycling the applied magnetic field while simultaneously measuring the resulting magnetic moment of the sample at constant temperature. The superconducting current density that screens the sample is calculated from the width of the hysteresis loop (Δm) using the Bean critical model[1]. From the obtained $J_c(H)$ curves, the irreversibility field is obtained as the field for which the value of J_c just reaches a small value (usually 10 or 100 Am^{-2}). Ideally, this value of J_c should correspond to the difference in the magnetic moments of the ZFC and FC curves that was used to obtain the irreversibility temperature. The measurements are performed for a set of temperatures, which results in an irreversibility line. This

irreversibility line will be different from the one obtained from ZFC and FC measurements if the criteria used to obtain the irreversibility field from $J_c(H)$ and the irreversibility temperature from ZFC and FC measurements are different. In all the above measurements, a scan length of 4cm was selected to avoid effects of sample movement in the slightly inhomogeneous field of the superconducting magnet.

To obtain the angular dependence of the irreversibility line, the hysteresis loops were measured within a 90° range, with a 10° increment. The angle with the highest value of the irreversibility field was considered to correspond to the orientation for which the field is aligned with the *ab*-plane of the crystal. Further measurements around that angle were carried out with a smaller increment (in this case 0.2°), in order to obtain an accurate value of the measured angle for which the field is aligned with the *ab*-plane. The MPMS resolution for this measurement was 0.1°.

In relaxation measurements, in order to avoid any experimental errors, the standard multi-step procedure [2] was adopted: I) The magnetic hysteresis loop at the desired temperature was measured with a specific sweep rate. If SQUID MPMS-5T is used, the sweep rate, unfortunately, is not under the user's control. II) From the virgin magnetization curve (starting from $m = 0$, $H_o = 0$), the field, $H_{minimum}$, corresponding to the minimum magnetic moment was determined. The value of 1.5 times this field was approximately considered as the full penetration field, H_{ful}. III) The reversible component of the magnetic moment, $m_{rev}(H)$, was calculated by averaging the upper and lower branches of the hysteresis loop and subtracting this average magnetization from the measured magnetic moment for each value of the field at which the moment was measured. IV) The sample was cooled from above T_c to the desired temperature, T, at zero applied field (ZFC). At about 600s after the sample's temperature stabilized, a magnetic field higher than H_{ful} was

applied. V) The applied field was decreased to the measurement field. VI) At this stage, collection of magnetic moment data as a function of time was started.

Due to the higher resolution of MPMS, the relaxation measurements were carried out with this machine. Another advantage of MPMS is that the sample scan length can be changed to a desired amount, whereas for PPMS the scan length is not under control. However, since the maximum applied field for MPMS is limited to 5×10^4 Oe, the relaxation data at low temperatures are not trustworthy. This is because the value of H_{ful} is higher than the 5×10^4 Oe available with MPMS. Therefore, the data for low temperatures (mainly below 15K) were disregarded.

The first step before starting magnetic measurement is to check the quality of the samples under investigation. Therefore, in the next section, some experimental techniques necessary to investigate the quality of the samples are introduced to ensure that the samples are single phase and homogeneous and to find out what kind of crystal defects are involved.

4.2 Preparation and Characterization of the Samples

4.2.1 $(Tl,Pb)(Sr,Ba)_2Ca_2Cu_3O_y$ Single Crystal

The $(Tl,Pb)(Sr,Ba)_2Ca_2Cu_3O_y$ single crystal used in this study was grown by the self-flux method by Wang et al. [3,4]. Powders of $(Tl,Pb)(Sr,Ba)_2Ca_2Cu_3O_y$ mixed with extra Tl_2O_3 and PbO in the ratio of Tl : Pb = 6 : 5 were pressed into pellets, wrapped in gold foil to prevent significant loss of Tl and calcined. Alumina crucibles covered in gold foil were used, and the polycrystalline bulks obtained were nearly pure Tl-1223. Crystal growth was carried out in a tube furnace with a large heat gradient under flowing oxygen. The heating sequence was:

$$RT \xrightarrow{400^{\circ}Ch^{-1}} 955\ ^{\circ}C \xrightarrow{0.5h} 955\ ^{\circ}C \xrightarrow{5^{\circ}Ch^{-1}} 900\ ^{\circ}C \xrightarrow{5h} 900\ ^{\circ}C \xrightarrow{turn\ off\ furnace} RT$$

After the growth, the composition of the crystal was checked by x-ray diffraction and energy dispersive spectrometry (EDS) to make sure that the single crystal was Tl-1223 phase. The crystallinity of the single crystal was studied by the x-ray precession technique using Mo Kα radiation. The natural surface of the single crystal was observed with SEM. Although the crystal looked like a platelet, the thickness was not as small as for BiSrCaCuO crystals, which are known to be plate-like and easily cleaved along the *ab* plane. The ratio of the thickness along *c* as compared to the crystal dimensions in the *a* or *b* direction was at least 4 times higher than for BiSrCaCuO. It was not easy to cleave a very thin crystal along its plane. The reason may be that the interaction between the individual crystal cells, which are separated by a single TlO layer, is much stronger than in BiSrCaCuO, where the separation is by double BiO layers. The morphology of the Tl-1223 single crystal is similar to that of YBCO single crystals. The single crystals were cleaved by a mechanical method, and the cleaved surface was scanned by an AFM in contact mode.

X-Ray Diffraction (XRD) pattern: From XRD pattern, (Figure 4.3) it was revealed that the flat surface of the crystal corresponds to the *ab* plane, i.e. the growth direction for each layer is along the *c*-axis. Orientation misfits were absent in the *hk*0 precession photograph. Strong and narrow peaks corresponding to Miller indices (00*l*) with $l = 2, 3, 4,\ldots$, are an indicator of a high degree of preferred orientation of the crystallographic plane.

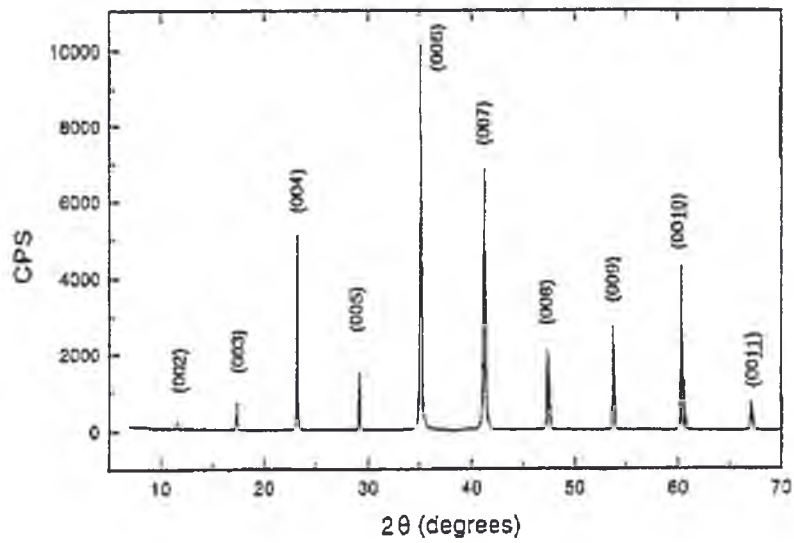

Figure 4. 3 X-ray diffraction pattern of a Tl1223 single crystal recorded with a powder diffractometer. The *ab* plane of the crystal was parallel to the surface of the sample holder. The applied wavelength was 0.154178 nm.

Scanning Electron Microscopy (SEM): The natural surface morphology of an as-grown crystal observed by the SEM technique can provide evidence of the crystal growth mechanism. Figure 4.4 shows the typical line growth steps on the *ab*-plane, implying a layer-by-layer growth mechanism [4].

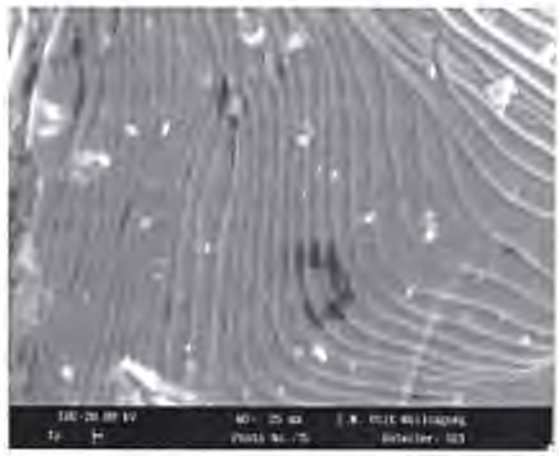

Figure 4. 4 SEM image of line growth steps on ab-plane.

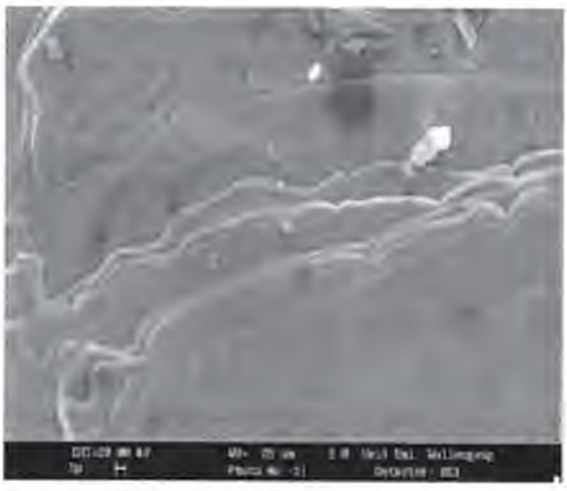

Figure 4. 5 Growth step aggregation observed in a SEM image.

Figure 4.5 shows irregular line steps with large gaps between them, from which the layer structure is more clearly seen. In a local area, the steps show a curved shape, which has occurred when the growth of steps was blocked by an impurity or the exhaustion of solute. This is common in a natural growth system without constant stirring to homogenize the solution. In this pattern, the macro-line steps are formed through the aggregation of the micro-steps. No spiral dislocation has been observed from SEM images [4].

Atomic Force Microscopy (AFM): Figure 4.6 shows a top view image of a $1.5\times1.5\mu m^2$ square area with successive dark and light stripes, which was cut from a larger original area. In Figure 4.7, a three dimensional picture was reconstructed, in which the modulation structure is more clearly shown. From the analysis of Figure 4.6 it can be seen that the unit period is about 200 nm on average and the height of the peak is about 0.7- 0.8 nm. Compared with the parameters ($a = b = 0.38$ nm and $c = 1.55$ nm) of the unit cell of Tl1223 single crystal, the period is about 500 times longer than the a-axis and half the height of the c-axis parameter. The observed surface is a cleaved surface, not a naturally grown surface, so the modulation structure doesn't seem to consist of growth steps. The period of the

modulation structure is larger than those observed in other superconductors, such as Bi2212 [5]. It seems most likely that some kind of structural dislocation formed during the growth.

Figure 4. 6 The periodic modulation structure on newly cleaved c-face observed by AFM.

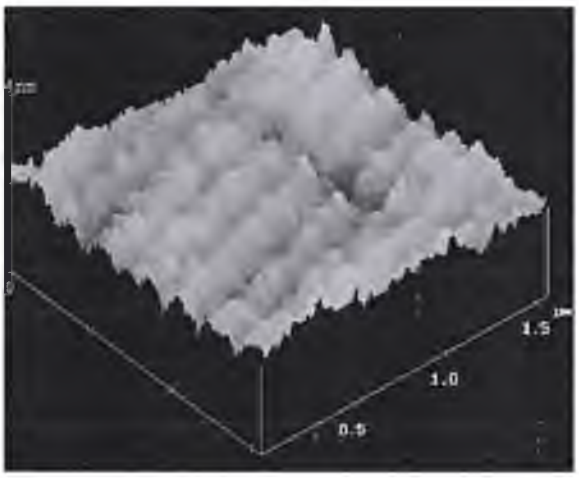

Figure 4. 7 An AFM reconstructed 3D modulation structure.

Superconducting transition: The transition temperature (T_c) of the sample was determined by temperature scanning of the DC magnetic moment. The measurement was performed with the MPMS-5T SQUID magnetometer, with a resolution of up to 10^{-8} emu. A magnetic field of H_o=100 Oe parallel to the *c*-axis (normal to the shiny surface) of the sample was applied. After zero-field cooling the sample and scanning temperature from far below T_c to above T_c, the onset of deviation from the horizontal axis with the criterion of

$\Delta m = 10^{-5}$emu was selected as T_c, which was obtained as 110K. Furthermore, from Figure 4.8(a), it can be seen that the sample lacks an intergrowth of Tl1212 phase (since no additional transition exists). Therefore, the sample is purely single phase.

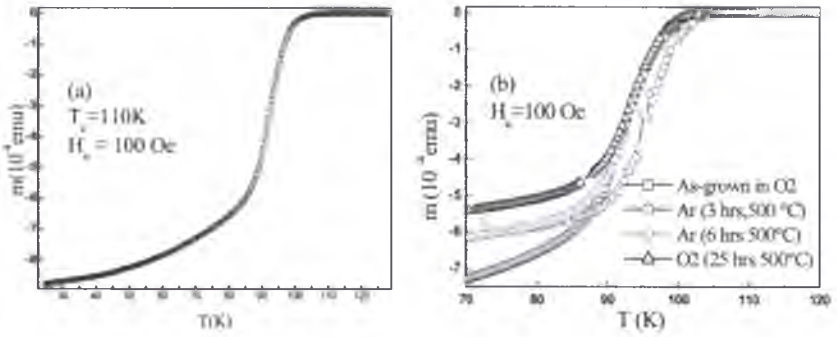

Figure 4. 8(a) The onset of deviation of DC magnetic moment from the m=0 axis was determined as T_c. (b) The effect of heat treatment on the T_c of the samples annealed under different conditions.

Further heat treatment: Whereas the as-grown sample shows T_c = 110K, its heat treatment in pure argon for 3 hours at 500°C led to higher T_c. However, further heat treatment of the sample in pure argon or in pure oxygen for a longer period yielded a lower T_c onset. Figure 4.8(b) shows the heat treatment effects on the T_c of the samples heat-treated under different conditions.

4.2.2 $Sm_{1+x}Ba_{2-x}Cu_3O_{6+y}$ (x = 0.04) Single Crystal

The top-seeded solution growth method was used by Yao et al. to grow single crystal in air [6]. Sm_2O_3 crucibles were used so that the contamination from the crucible could be reduced to a minimum. High-quality Ba-Cu-O powders were used as raw materials for the solvent. Sm was not included in the precursor mixture. Instead, the Sm solute was supplied through the interaction between the molten solvent and the Sm_2O_3 crucible. YBCO thin

film was prepared by the thermal co-evaporation technique on MgO single crystal. This YBCO-deposited MgO crystal was used as a hetero-seed for the SmBCO crystal growth because a homo-seed consisting of SmBCO thin film cannot be prepared by the thermal co-evaporation method due to the phenomenon of Sm sublimation. This YBCO thin film is highly *c*-axis oriented, as shown by its X-ray diffraction (XRD) patterns [6]. The rotation speed and the pulling rate were in the range of 70-120 rpm and 0.10-0.20 mm h^{-1}, respectively. The growth temperature was about 1060 °C, which is higher than the peritectic temperature T_p of YBCO oxide, the seed-film material. The average growth rate is approximately 0.13 mm h^{-1} in the *c*-axis direction, which is higher than in the YBCO system (nearly 0.05 mm h^{-1} in the *c*-axis direction in ambient atmosphere). As-grown SmBaCuO crystal was annealed in a tube furnace at 340 °C for 250 h in an oxygen gas flow.

X-Ray Diffraction (XRD) pattern: X-ray diffraction analysis of the sample (Figure 4.9) resulted in a single-phase spectrum. Strong and narrow peaks correspond to Miller indices (00*l*), with $l = 1, 3, 5, 6, 7$, which is an indicator of a high degree of preferred orientation of the crystallographic plane.

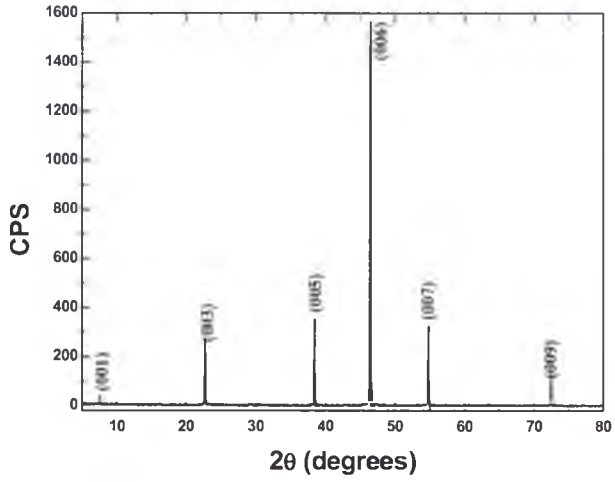

Figure 4. 9 X-ray diffraction pattern of the non-stoichiometric Sm123 single crystal. The applied wavelength was 0.15054 nm.

Optical Light Microscope Observation: Figure 4.10 displays a polarized optical image of the *ab*-plane of the crystal which clearly shows twin structures similar to those of a Y123 or Nd123 crystal in the orthorhombic phase [7,8]. The polarized optical image of the *ab*-plane of the crystal clearly shows the twin planes with a spacing range from a few micrometers up to a few tenths of micrometers.

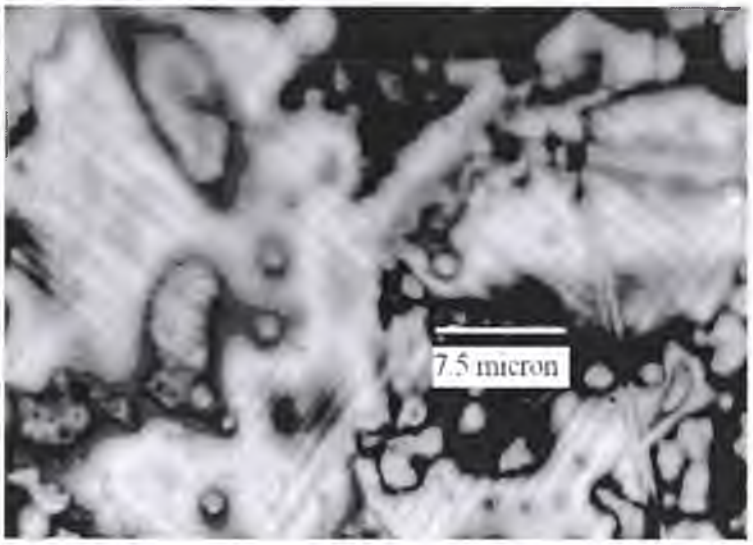

Figure 4. 10 Optical micrograph of Sm123 single crystal, which is highly micro-twinned.

Bright light transmission electron microscope (TEM): From bright light TEM examination a few crystalline defects could be detected, possibly stacking faults. The presence of twins was also confirmed by the bright light TEM technique (arrows in Figure 4.11). From this figure twins with sub-micrometer spacing (that is, as small as 50-60 nm) can be detected. From the energy dispersive X-ray spectroscopy (EDS) map, oxygen distribution was found to be uniform (Figure 4.12). The diffraction pattern of the sample grains was consistent with orthorhombic phase (Figure 4.13), and no other phases, e.g. tetragonal, were detected. From this figure, which is a diffraction pattern of the [001] zone axis - the spots going (roughly) top to bottom to the left side of the line are the spots representing (110) type planes. The central (000) spot is marked. The spot above the (000) spot is (110), then (220), (330) and (440). The splitting of the spot (440) is due to twinning. This implicates that whilst the twin planes were all parallel to the crystal c-axis, they have (110) orientation. From this figure the orthorhombic phase is obviously concluded.

Figure 4. 11 The presence of twins was also confirmed by the bright field TEM technique.

Figure 4. 12 From the EDS map, the distribution of Oxygen atoms was found to be uniform.

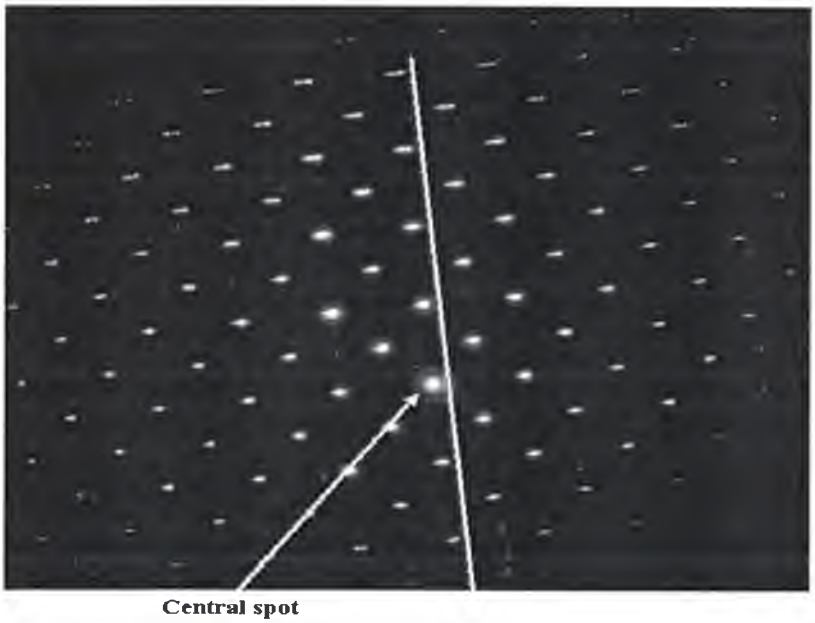

Figure 4. 13 The diffraction pattern of the sample grains was consistent with orthorhombic phase. The spot above the central spot [which is marked by (000)] is (110), then (220), (330) and (440). The splitting of the spot (440) is caused by twinning

Superconducting transition: The transition temperature (T_c) of the sample was determined from the temperature scan of the DC magnetic moment. The measurement was performed with the MPMS-5T SQUID magnetometer. A magnetic field of H_o=20 Oe parallel to the *c*-axis (normal to the shiny surface) of the sample was applied. After zero-

field cooling the sample and scanning the temperature from far below T_c to above T_c, the onset of deviation from zero magnetic moment with an accuracy of $\Delta m = 10^{-5}$emu was selected as T_c, which was obtained to be T_c= 95K, with the transition width ΔT<2K (Figure 4.14). Apart from the sharp transition in this figure no others exist.

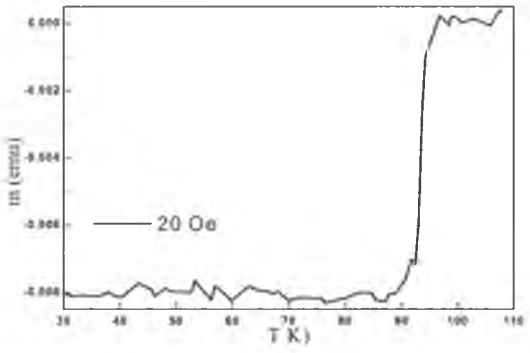

Figure 4. 14 The onset of the transition was determined to be T_c = 95K when a field of 20 Oe was applied.

References

[1] C. P. Bean, Rev. Mod. Phys. 36, 31 (1964).

[2] Y. Yeshurun, A. P. Malozemoff, and A. Shaulov, Rev. Mod. Phys. 68, 911 (1996).

[3] X. L. Wang, X. M. Yang, H. W. Weber, R. Abraham, K. Lebbou, M. T. Cohen-Abad, E. Halwax, and P. Wiede, J. Cryst. Growth 167, 93 (1996).

[4] Z. X. Cheng, X. L. Wang, S. Keshavarzi, M. J. Qin, T. M. Silver, H. K. Liu, H. Kimura, and S. X. Dou, Supercond. Sci. Technol. 17, 696 (2004).

[5] J. M. Perez-Mato, J. Etrillard, J. M. Kiat, B. Liang, and C. T. Lin, Phys. Rev. B 67, 024504 (2003).

[6] X. Yao, T. Izumi, and Y. Shiohara, Supercond. Sci. Technol. 16, L13 (2003).

[7] C. T. Lin, J. Chrosch, Y. Yan, W. Y. Liang, and E. K. H. Salje, Physica C 242, 105 (1995).

[8] M. Nakamura, Y. Yamada, T. Hirayama, Y. Ikuhara, Y. Shiohara, and S. Tanaka, Physica C 259, 295 (1996).

CHAPTER FIVE: EXPERIMENTAL RESULTS AND DISCUSSIONS

In this research, two crystals from the Tl1223 and Sm123 families with the composition $(Tl,Pb)(Sr,Ba)_2Ca_2Cu_3O_y$ and $Sm_{1.04}Ba_{1.96}Cu_3O_y$ have been investigated. The main part of this chapter is allocated to $(Tl,Pb)(Sr,Ba)_2Ca_2Cu_3O_y$ single crystal, followed by the determination technique for measuring the lock-in angle which was examined on the $Sm_{1+x}Ba_{2-x}Cu_3O_y$ crystal with $x = 0.04$.

5.1 $(Tl,Pb)(Sr,Ba)_2Ca_2Cu_3O_y$ Single Crystal

The size of the sample, which will be referred to as Tl1223 from now on, was $154\times650.8\times405.8$ μm^3. For all magnetic measurements, after zero-field cooling, the magnetic field was applied parallel to the *c*-axis of the single crystal.

5.1.1 Magnetic Hysteresis Loop, Critical Current Density and Peak Effect

Figures 5.1.1(a) and (b) show typical magnetic hysteresis loops for different temperatures. This measurement was performed with a *Magnetic Property Measurement System*-5T (MPMS). From this figures the anomalous peak effect can be clearly seen. The peak starts appearing at 15K, and it persists up to about 60K. However, the peak at low temperatures is less pronounced, and it is shallow. (For this reason only a quarter of the peak has been shown to magnify the extent of the peak.) Due to the small size of the sample the loops at temperatures above 60K are accompanied by violent fluctuations so that it is hard to identify any probable peak at those temperatures. As can be seen the peak is displaced to higher fields as a result of decreasing temperature. We therefore, could detect only the onset of the peak at low temperatures since the maximum of the magnetic moment at those temperatures occurs in a field range far beyond the accessible field in this

investigation. From this measurement, the minimum position in the virgin curve at 5K was determined to be about 20000 Oe (not shown here). Then for achieving the full penetration state at this temperature, application of a magnetic field of ~ 6 T is necessary [1], and this means that the maximum accessible field in this investigation was sufficient for achieving full penetration status only for temperatures higher than 10K. For this reason, all temperature data less than 10K are disregarded.

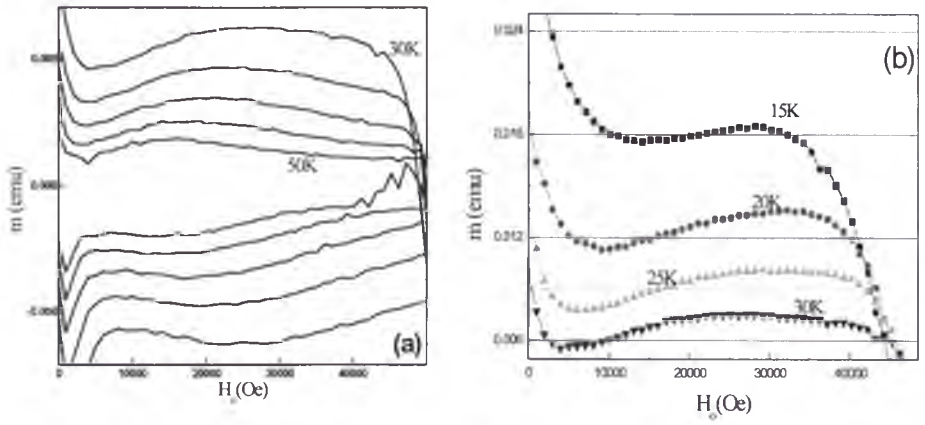

Figure 5.1. 1 Typical magnetic hysteresis loops for temperatures from 30K to 50K, half loop (a) and from 15K to 30K, quarter loop (b). The peak effect is observable at all temperatures but it is less pronounced at low temperatures. The horizontal grid lines in (b) were drawn for better elucidation of the extent of the peak effect.

The symmetric shape of the loops implies that the surface barrier is negligible[1]. Furthermore, due to the almost perfectly symmetric feature of the hysteresis loops, the reversible component of the magnetic moment, defined as $m_{rev} = (m_{up} + m_{down}) / 2$, was obtained to be also negligible. In this relation m_{up} and m_{down} are the upper and lower

branches of the magnetic hysteresis loop, corresponding to decreasing and increasing magnetic field, respectively.

The critical current density shown in Figure 5.1.2 is obtained from the Bean critical state model [2]

$$J = \frac{20}{d(1-d/3b)}\frac{\Delta m}{V} \qquad (5\text{- }1)$$

where Δm is the width of the magnetic hysteresis loop in emu, V is the volume of the sample, b and d are the dimensions (in cm) of the sample in the ab-plane with $b > d$.

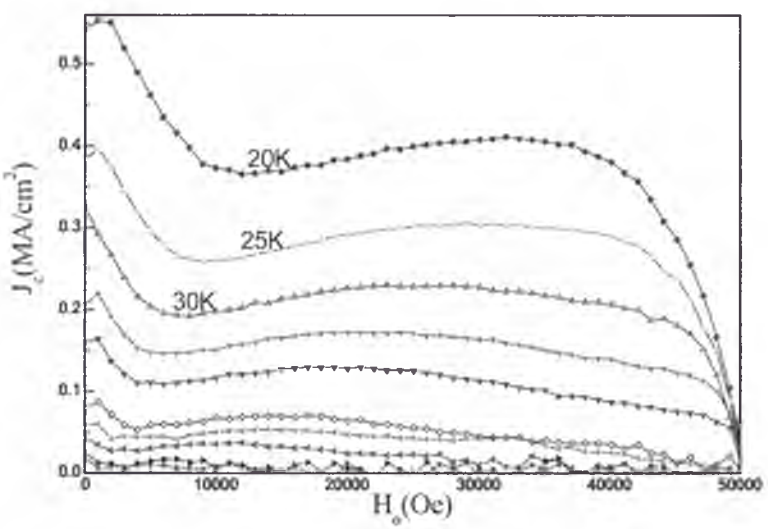

Figure 5.1.2 Field dependence of the critical current density at different temperatures calculated using the Bean critical state model.

The measured critical current density of 0.01 MA/cm^2 at 75K and zero-field in this work is considerably smaller than the intra-grain critical current density of 1.6 MA/cm^2 at 77.3K estimated by List et al. on a polycrystalline Tl1223 sample [3], whereas the difference is less at lower temperature. However, the critical current density for this as-grown sample is either comparable to or higher than silver sheathed Tl1223 tapes made by different

preparation techniques[4]. This significant difference implies that the critical current density is not in the optimum pinning condition. Due to the absence of the weak link problem, a single crystal should show a critical current density comparable to the intra-grain critical current density. However, it has been well established that oxygen vacancies have a significant role as pinning sites in high-T_c superconductors. Heat treatment of an as-grown sample under different circumstances can shed light on the oxygen vacancy role as point pinning disorder.

Further heat treatment: Whereas the as-grown sample shows T_c= 110K, its heat treatment in pure Argon gas for 3 hours at 500°C led to a slightly higher T_c [Figure 4.8 (b)]. However, further heat treatment of the sample in pure Argon or in pure Oxygen gas for a longer period yielded a lower T_c.

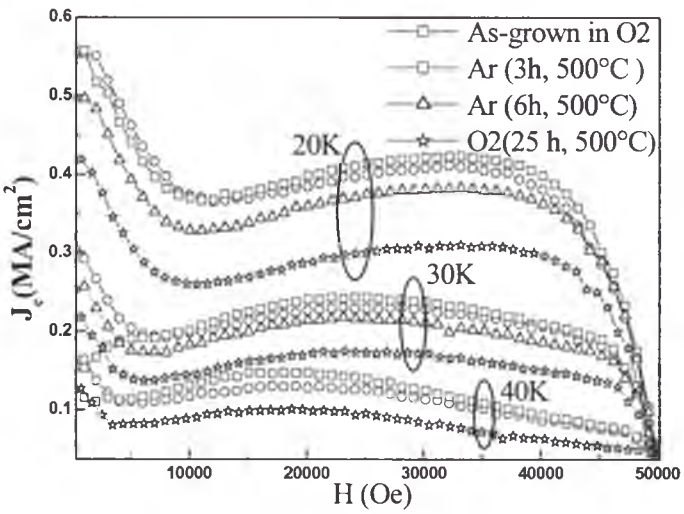

Figure 5.1.3 The effect of heat treatment on J_c of the Tl(1223) single crystal heat treated under different conditions.

Figure 5.1.3 shows the effect of the heat treatment on J_c at temperatures of 20, 30 and 40K. For all cases there is an apparent peak effect. The different heat treatment conditions have little effect on the peak shape and position but do affect the magnitude of the peak. The sample heat treated in pure Argon gas for 3 hours shows the highest J_c compared with the original sample. Heat treatment of the sample after embedding in PbO at 500°C for 30 hours led to higher critical current density[5] over a wide temperature range (Figure 5.1.4). For example, at 20K, current density was increased by 27%, as compared with the heat treatment just in argon gas [5]. This treatment even led to a significant improvement in the irreversibility field.

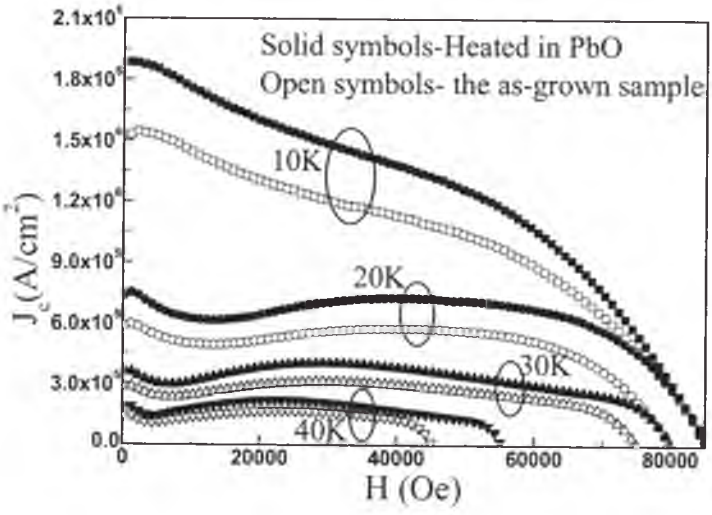

Figure 5.1.4 J_c is increased by heat treatment of the Tl(1223) single crystal embedded in PbO at 500°C.

The hysteresis loops and current densities in Figures 5.1.1- 5.1.4 show different characteristics; a relatively pronounced peak effect can be seen at high temperatures which is absent at low temperatures below 15K. Several reasons can be proposed for the absence of the peak at low temperatures: i) The peak occurs at higher magnetic fields beyond the highest accessible field in this investigation, since from those figures it can be seen that the

peak position is highly temperature dependent and it shifts to higher fields with falling temperature while getting broader at the same time. That is, the peak effect should be very broad and shallow at low temperatures (below 20K). This behaviour has been frequently observed for other superconductors with low anisotropy such as Y(123)[6,7] and Tl(1223) thin film[8]. Even if we assume that the peak occurs at a very high field range and is very broadened, this suggests that at low and intermediate fields and low temperatures no significant change in vortex dynamics occurs. In these circumstances where the vortices are far apart from each other, the pinning parameters are determined by only the longitudinal collective pinning length, L_c, which is field independent, and therefore no significant change in current density is expected. ii) The oxygen content is not in an optimum state. Heat treatment of the sample in different circumstances showed that the shape of the hysteresis loops at lower temperatures is preserved (see Figure 5.1.3). That is, the shape of the loops is independent of the oxygen content at low temperatures, while with increasing temperature the shape of the loop slightly changes. This means that the oxygen content doesn't have a crucial influence on the dynamics of vortices at low temperatures and its influence changes gradually with increasing temperature as the melting line is approached. iii) The time scale of measurement is not long enough to be able to discriminate between different vortex regimes with different relaxation time scales. For example, Krusin-Elbaum et al.[6] ascribe the occurrence of the peak effect to the crossover between two regimes of collective vortex creep, that is from single vortex creep to collective vortex creep[6]. The independence of the magnetic moment from the applied field for low temperature isothermal loops is interpreted by them as the single vortex regime[6] over the entire field. They believe that the peak effect is not likely to be observed on very short time scales due

to the fact that the relaxation is much faster in the single vortex regime than in the collective bundle vortex creep regime. However, in a pulsed field technique, which is a very short time scale measurement, it has been revealed that the peak effect is present even for very short time scales [9]. Yeshurun et al. also assigned dynamical characteristics to the appearance of the peak effect. In magnetic hysteresis loop measurements, there is a waiting time between establishing the *dc* field and the time when the magnetic moment measurement is recorded. It has been shown that the peak effect disappears with increased waiting time at relatively high temperature, while it is strengthened with increased waiting time at relatively low temperatures[10]. In the *dc* measurements this can practically be examined either via using a different magnetic field sweep rate for the hysteresis loop measurements or via relaxation measurements. Performing the second alternative showed that even at a longer time window no new observable behaviour such as the peak effect emerged at low temperatures. From the present investigation we will see that, despite the presence of the peak effect within the entire time window, the vortex behaviour across the peak position has dynamical roots, and no phase transition can be assigned to the changes across the peak. However, the rising magnetic moment at the onset of the peak effect will be interpreted on the basis of a phase transition from a quasi-lattice, ordered, vortex ensemble to an entangled vortex glass status in which this entanglement become more intense while crossing the peak effect line. No long-range order is preserved in the latter phase.

The appearance of the peak at intermediate and high temperatures is an indicator of the enhancement of vortex pinning. This feature of Tl(1223) single crystal has been observed by another group as well[11]. Several hypotheses have been proposed to explain the

peak effect. In many such investigations the influence of oxygen content on the peak behaviour is discussed[12,13]. For example Zhukov et al[12] found that the peak effect was present at high temperatures for all oxygen contents, however the peak's height takes the smallest value for the state closest to stoichiometric status, which means that oxygen deficiency is necessary for achieving greater pinning and therefore higher critical current density. This fact is partially confirmed by the data obtained in this investigation. In Figure 5.1.3 we can see that fully oxygenating the sample led to the lowest critical current density, and de-oxygenating the sample to a certain level of oxygen content led to the improvement of the critical current density. Consequently, point disorder, and oxygen vacancies in particular, have a leading role in the vortex dynamics in Tl(1223).

In some cases a correlation between the peak effect and the oxygen concentration is found to be the source of peak effect. For example, in extremely pure YBCO single crystals it was shown that the peak effect can be reversibly suppressed by full oxygenation under high pressure[14]. In the view of Däumeling et al. [15] a field-induced pinning enhancement in oxygen-deficient regions is assumed to be the source of the peak effect. They proposed that oxygen-deficient areas had become normal as the field was increased, as a result of their lower T_c and H_{c2}. These areas thus become new pinning centres. Therefore any change in oxygen content or distribution should lead to suppression or appearance of the peak effect. In contrast to all the above-mentioned works suggesting that oxygen deficiency is a key factor in the appearance of the peak effect, there are some other experiments indicating that oxygen deficiency doesn't play a leading role. For instance, from Wisniewski et al.'s[16] work it was concluded that other types of defects such as impurities or structural defects like dislocations or stacking faults might be responsible for the peak effect. The significant

change in current density of the Tl1223 sample in Figure 5.1.4 as a result of heat treatment in PbO, shows that impurity and substitution has a considerable contribution in the enhancement of the critical current density and appearance of the peak effect as well. That is, the oxygen vacancy is not the only source of peak formation, and other types of point disorder also might have considerable impact on vortex dynamics. For example, Tl/Pb or Ba/Sr substitutions can influence the pinning strength via lowering the anisotropy parameter. The smaller size of Sr^{+2} than Ba^{+2} leads to a shrinkage of the copper oxide layer spacing and consequently to smaller anisotropy[17]. With partial substitution of Tl by Pb, Kim et al.[18] showed that not only does the screening current density stabilize, but also a higher irreversibility line is achieved. That is, pinning strength can be promoted via Tl/Pb substitution that could originate from the shrinkage of the longitudinal lattice structure. This is more severe for Tl because of its high degree of volatility, which may lead to the reduction of Tl content as a result of the heat treatment. Enhancement of current density and the irreversibility field in Figure 5.1.4 confirms that with further Pb addition either more pinning centres are introduced into the system or the anisotropy is reduced. Heavy Pb-doping of Bi2212 single crystal is believed to decrease the anisotropy parameter by siting the Pb ions between the copper oxide planes, which leads to enhancement of *c*-axis conductivity[19].

In a quite different model, the peak effect is considered as a result of the matching effect[20] where matching of the vortex lattice with the defect structure leads to pinning enhancement. At a dilute field where the number of vortex lines is much fewer than the number of pinning centres, they can easily wander around due to the presence of many equi-energetic positions. At higher fields in which the number of vortex lines is

comparable with the pinning centres (in other words, the vortex lattice parameter is equal to the mean pinning centre spacing) they have less mobility and therefore more severe pinning status. The temperature-dependent nature of the peak effect in the present sample strongly rules out the matching effect as the origin of the peak effect. If the matching effect was responsible for the peak effect, the peak position would be temperature independent and only spatial distribution of the defect would be the determining factor in the occurrence of the peak.

Another feature associated with the magnetic hysteresis loops which could hold some information about the mechanism involved in vortex dynamics are the characteristic fields H^* (corresponding to a steep change in the magnetic moment on the low-field side of the hysteresis loop) and H_{min} (associated with the minimum in magnetic moment for fields smaller than H^*). Due to the broadness of the peak effect, H^* can only be located by calculating the maximum of the derivative of magnetic moment vs. applied magnetic field, that is dm/dH. Giller et al. assign this field (H^*) to the order-disorder transition of the vortex lattice (section 3.2.6) in $Nd_{1.85}Ce_{0.15}CuO_{4-\delta}$ and untwinned $YBa_2Cu_3O_{7-\delta}$ crystals[21,22]. In order to investigate the cause of the rise in magnetic moment (peak effect) all these characteristic fields were extracted from the hysteresis loops. Shown in Figure 5.1.5 is the temperature dependence of H^* and H_{min} in addition to the irreversibility and the peak effect lines related to the as-grown sample. The irreversibility line was determined from the merging point of the FC and ZFC curves (Chapter 4) and has been drawn with two different scales. As can be seen, the irreversibility line can be best fitted by a quadratic function of $(1-T/T_c)$ within the field range $0 - 3.5\times10^4$ Oe. (The solid line associated to the top axis is a quadratic curve function.) To determine the field at which the second peak appears for an

isothermal magnetic hysteresis loop, a second order polynomial fit to the data around the peak has been employed.

In what follows it is shown that H^* is the so-called order-disorder field. Part of the discussion will be justified in following section using relaxation data.

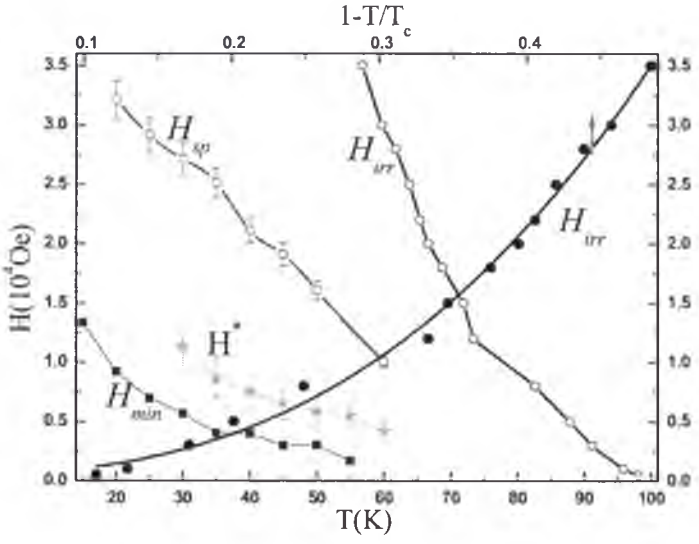

Figure 5.1.5 Phase diagram of $(Tl,Pb)(Sr,Ba)_2Ca_2Cu_3O_y$ Single Crystal. $H^*(T)$ line (star symbols) corresponds to a steep change in the low-field side of the peak effect (where the derivative dm/dH of the loop becomes maximum) for the different isotherm loops. The H_{min} is the minimum in the magnetic moment on the low-field side of the peak effect where the derivative dm/dH becomes zero. Open and solid circles are the same irreversibility line on two different scales. This line was determined from the merging point of the FC and ZFC curves. The solid curve is the best fit to irreversibility data and shows that the irreversibility line is a quadratic function of $(1-T/T_c)$.

According to the theory of the order-disorder transition quantified by G. M. Mikitik and E. H. Brandt et al.[23], depending on the type of pinning, the order-disorder transition field can be either an ascending or descending function of temperature. For example, as a result of their calculation in the single vortex regime for δl-pinning (caused by spatial variations of the electron mean free path) and δT_c-pinning (caused by spatial variations of the transition

temperature), the temperature dependence of the transition field is as $H_{dis}(T) \propto \xi(T)$ and $H_{dis}(T) \propto \xi(T)^{-3}$, respectively. In these expressions ξ is the superconducting coherence length in the *ab*-plane and it changes as $\xi \propto (1-T/T_c)^{-1/2}$. That is, for δT_c-pinning we have

$$H_{dis}(T) = H_{dis}(0)\,(1-T/T_c)^{3/2}$$

Similar results can be obtained by phenomenological approach of Ertas[24] and Vinokur[25] et al. The data in Figure 5.1.5 clearly show that both $H^*(T)$ and $H_{min}(T)$ are decreasing functions of temperature and therefore only the δT_c-pinning formula can explain the data properly. The $H^*(T)$ is believed to be the order-disorder line which discriminates a weakly disordered quasi-lattice (the Bragg Glass phase) from a highly disordered solid phase (entangled solid, or Vortex Glass phase). In order to obtain a quantitative insight into the solid entangled line, an attempt has been made to calculate the relevant energies, which are the pinning and elastic energies of the vortex system. To be able to use the relation (3-40) to calculate the pinning energy and consequently use the relation (3-44) we must first examine if the collective pinning length L_c is smaller than the size of the elastic cell (or longitudinal elastic fluctuations) L_o. The size of the collective pinning length is

$$L_c=(\Gamma^4\varepsilon_o^2\xi^2/\gamma)^{1/3}=\Gamma\xi(J_o/J_c)^{1/2}$$

whereas J_o is the de-pairing current defined as

$$J_o= 4\Phi_o/[3\sqrt{3}\xi(4\pi\lambda)^2].$$

Using characteristic factors for the sample, such as $\lambda \approx 1900$ Å, $\xi \approx 20$ Å [26-28], the critical current density $J_c(0K) \approx 3\times10^6$ A/cm^2 (which has been obtained from extrapolation of the $J(T)$ at $H_o = 0T$, taking a 10% relaxation into account), and anisotropy factor $\Gamma^{-1} \approx 13$(measured in a later section), the two lengths L_c and L_o are calculated to be

$L_c \approx 55.69$ Å,

$L_o \approx 69.9$ Å.

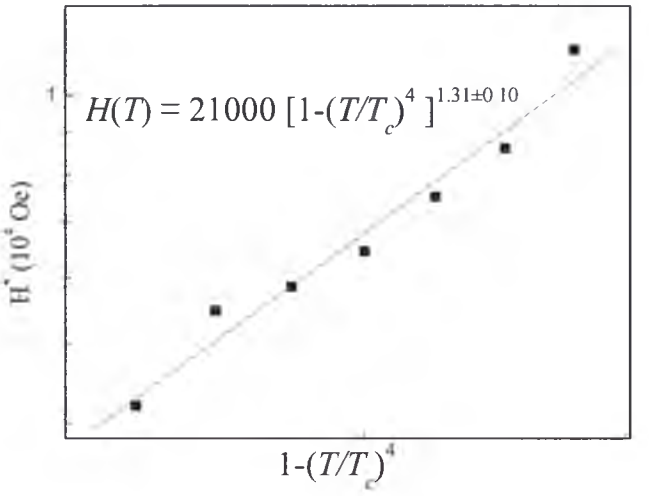

Figure 5.1. 6 The square symbols are H* data obtained from figure 5.1.5, which have been redrawn in a new scale to fit the data with relation (5-3). The solid line is the result of the fit.

Furthermore with the interlayer spacing of $d \approx 9.55$ Å [29] we will be able to use relation (3-44) to obtain the entangled line $H_{en}(T)$. For the single vortex regime where $\zeta=3/5$, relation (3-44) becomes

$$H_{en}=H_o(U_o/U_c)^3 \qquad (5\text{-}2)$$

with $H_o=c^2\Phi_o/\xi^2$, $U_o=c\Gamma\varepsilon_o\xi/2$, and the collective pinning energy $U_c=(\gamma\Gamma^2\varepsilon_o\xi^4)^{1/3}$. Substituting all these quantities into relation (5-2) and considering the functional form of the disorder parameter for δT_c-pinning, $\gamma \propto \lambda^{-4}$, [30] we arrive at the following expression

$$H_m = \frac{c^5\Phi_0\Gamma\varepsilon_0^2}{8\gamma\xi^3} \propto \frac{c_L^5\Gamma\lambda^{-4}}{8\lambda^{-4}\xi^3} \propto \xi^{-3} \propto \left\{\xi(0)\left[1-(T/T_c)^4\right]^{1/2}\right\}^{-3}.$$

In this relation, the expression $\xi(0)\left[1-(T/T_c)^4\right]^{-1/2}$ has been used for the temperature dependence of the superconducting coherence length. That is, the entanglement line should satisfy the following dependence on temperature

$$H_{en} \propto \left[1-(T/T_c)^4\right]^{3/2} . \qquad (5\text{-}3)$$

Shown in Figure 5.1.6 is the H^* in Figure 5.1.5 which has been re-drawn in another scale to show the quality of fit to relation (5-3). Considering the amount of uncertainty in the position of the maximum in dm/dH [denoted in Figure 5.1.5 with vertical error bars], the quality of the fit is satisfying. In this way the maxima in dm/dH , denoted by $H^*(T)$, can be considered as the entanglement line, that is $H^*(T) = H_{en}(T)$. As can be seen from the figure, the proportionality factor is $H_{en}(0) = 2.1\times10^4$ T. Similar fitting for $H_{min}(T)$ was not possible, and therefore $H_{min}(T)$ can not be the entanglement line.

In order to obtain more insight into the mechanism involved in the appearance of the peak, magnetic relaxation measurements could provide us with some complementary evidence, similar to what can be obtained from the hysteresis loop measurements by using different field sweep rates. In the SQUID magnetometer-5T employed in this work the magnetic field sweep rate is not under the user's control, and therefore magnetic relaxation measurement is exploited to extract the current density, and the field and temperature dependence of the effective activation energy.

5.1.2 Relaxation of Magnetic moment and Normalized Relaxation Rate

The magnitude of the magnetic moment of high-temperature superconductors is observed to decrease with time, in an approximately logarithmic way. The measured magnetic relaxation can be thought of as being caused by the spontaneous motion of flux lines out of

their pinning sites. Such a motion usually arises from thermal activation, but it can also arise from quantum tunnelling or other external activation, such as mechanical vibrations.

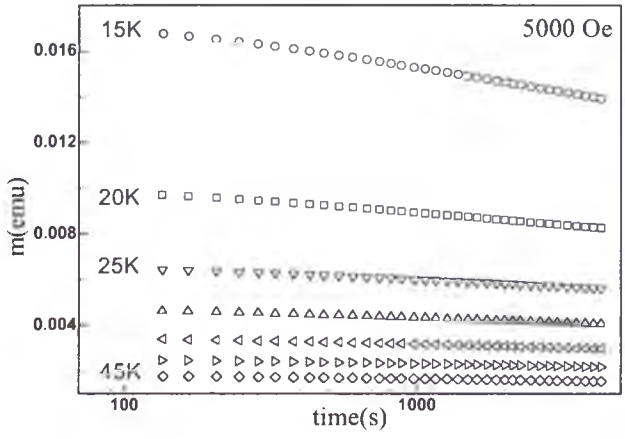

Figure 5.1.7 Typical decay of magnetic moment at 5000 Oe and at different temperatures shows logarithmic behaviour after 150 sec.

The effects of magnetic field and temperature on magnetic relaxation give us some evidence that can help to establish the theoretical foundations of superconductivity or confirm the existing theories and meanwhile lead us to a better understanding of the magnetic phase diagram and pinning mechanism.

Decay of magnetic moment can be measured by first zero-field cooling the sample to the desired temperature and then increasing the field up to a high field (a maximum field of 5×10^4 Oe for the SQUID magnetometer MPMS), which makes the field fully penetrate the sample, followed by a decrease to the measurement field. Due to the transient redistribution of magnetic flux over the sample cross-section [31], it took about 150 - 200s for the magnetic moment to show a logarithmic decay. This non-logarithmic stage duration is determined by the sample size, flux creep rate and the rate of change of the magnetic field.

Figure 5.1.7 shows typical relaxation data for an applied field of 5000 Oe. The time evolution of $m(H, T)$ was recorded during times $100 < t < 4300$ sec from the upper branch of the hysteresis loop. From the Anderson-Kim model a logarithmic behaviour for decay of magnetic moment is expected. However, this prediction can only be satisfied for conventional low-T_c superconductors, and deviation from this logarithmic decay has frequently been seen in high-T_c superconductors[32]. The data in Figure 5.1.7 show logarithmic decay after the initial stage transient time. The reason for the logarithmic decay is the selection of a short time window of about 70 minutes. In measurements with a time window of several hours this non-logarithmic decay can be clearly detected[32]. In what follows, due to incomplete penetration of magnetic field into the sample for $T<10$K, the measurements for this temperature range were disregarded. Similar measurements as in Figure 5.1.7 were performed at fields of 1×10^4, 2×10^4 and 4.6×10^4 Oe (including a few more measurements at 3.5×10^4 and 4×10^4 Oe, which haven't been shown here).

Sometimes, relaxation data related to an isothermal hysteresis loop can hold interesting information on the vortex dynamics of the sample under consideration. Figure 5.1.8 shows the relaxation data for three temperatures, 30, 35, and 40K. From these data also, the peak effect can clearly be seen, which shifts to lower field with increasing temperature. From the magnetic decay data, the normalized relaxation rate S is calculated via relation $S = -d\ln m/d\ln t$. In Figure 5.1.9, the field dependence of S is shown for different temperatures. Following a minimum at low field, this figure shows a monotonic increase of the normalized relaxation rate at 30, 35 and 40K between 1.5×10^4 and 3×10^4 Oe.

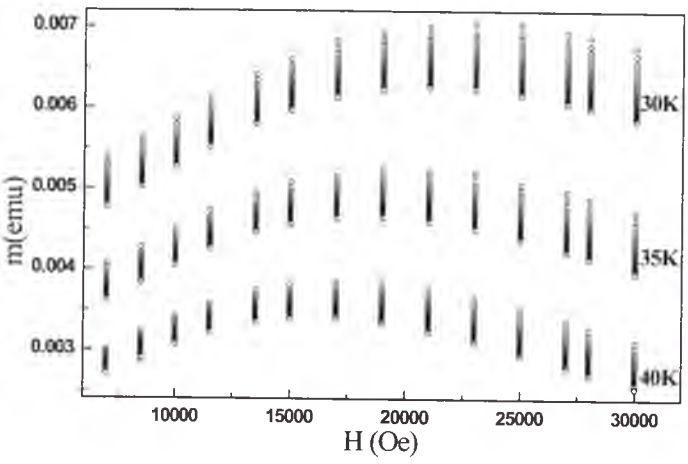

Figure 5.1. 8 Relaxation of magnetic moment for different fields at three different temperatures: 30, 35 and 40K. The shift of the peak to lower fields with increasing temperature is clearly seen.

The field dependence of the normalized relaxation rate S shows a similar pattern for all temperatures 30, 35 and 40K (Figure 5.1.9). It first decreases with field and then increases. The field and temperature dependencies of the minimum in $S(H)$ and the peak in the hysteresis loop follow qualitatively the same trend, that is, they shift to lower field with increasing temperature. This indicates that there is a correspondence between the vortex dynamics and the occurrence of the peak effect. In this figure the position of the characteristic field H^* has been extracted from the maximum of the derivative dm/dH, which is associated with a steep change on the low-field side of the peak in a loop, while the other set of arrows demonstrate the position of the peak in the magnetic hysteresis loop. In order to depict the above-mentioned situation, the derivative dm/dH and the normalized relaxation rate have been both drawn in Figure 5.1.9. As can be seen, the maximum in dm/dH coincides with the end point of the descending part of the normalized relaxation rate. That is, the minimum in $S(H)$ is a representative of a crossover or transition. It is worth noting that the normalized relaxation rate did not change across the peak position

(since the slope of $S(H)$ in Figure 5.1.9 is the same before and after the peak). This means that passing through the peak effect is unlikely to be associated with a phase transition in the vortex system structure.

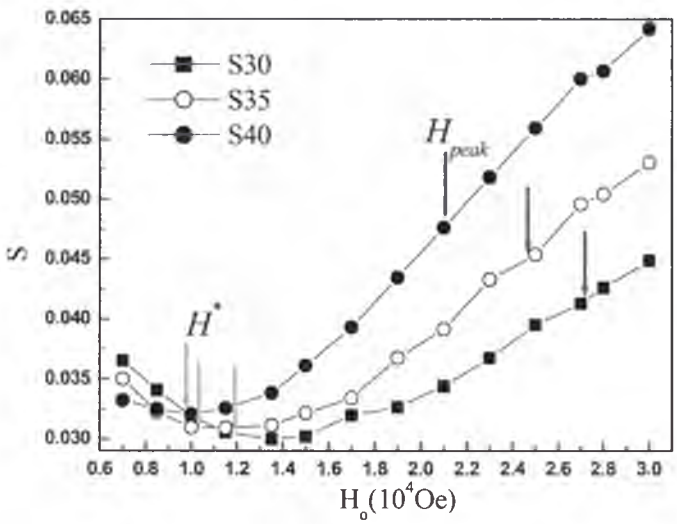

Figure 5.1. 9 Field dependence of the normalized relaxation rate at three temperatures. The field at the minimum corresponds to a steep change on the low field side of the hysteresis loop (H^*). The peak positions (H_{peak}) have also been located for the three 30, 35 and 40K temperatures.

This is in agreement with the time dependence of the peak position in Figure 5.1.11. This figure shows the decay of magnetic moment with time at various applied magnetic fields, that is $m(H,t)$ with T=40K. At each field the crystal was prepared (after zero-field cooling) in a fully penetrated state by first increasing the field to the maximum of 5T and then reducing it to the target value. Then the magnetic moment was recorded. The collection of data points within a given time interval (here 850 sec) at each field forms vertical traces shown in Figure 5.1.11—the length of each trace indicates the decay in m. As can be seen,

the decay is not monotonic at various fields, that is the segment lengths are longer at high fields above the peak, which has been reflected in higher normalized relaxation rates in Figure 5.1.9.

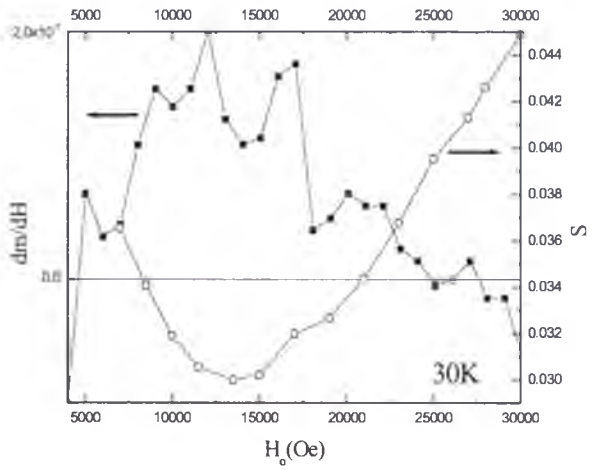

Figure 5.1. 10 The maximum in d*m*/d*H* coincides with the end point of the descending part in *S*(*H*), where the minimum in *S*(*H*) represents the onset of a new regime in vortex ensemble structure.

As a result of this non-monotonic behaviour, the peak position shifts to lower field with elapsed time (see the position of arrows in Figure 5.1.11). Of course, if a longer time window than 850 sec had been selected, the shift would be more obvious. From this measurement it is concluded that the maximum position in *m*(*H*) (in other words, the peak location) has dynamical roots. The frequency dependence of the peak position in an *ac*-susceptibility measurement can yield the same information as the relaxation *dc* measurement, and similar behaviour has already been reported [33]. From this report, with reduced frequency (which is equivalent to increasing the time window), the peak shifts to smaller fields. Both the time and the frequency dependence of the peak position vs. field are demonstrators of the dissipative nature of the behaviour around the peak position. It is

believed that the displacement of the peak to lower field with time elapsed is a signature of plastic vortex creep[33].

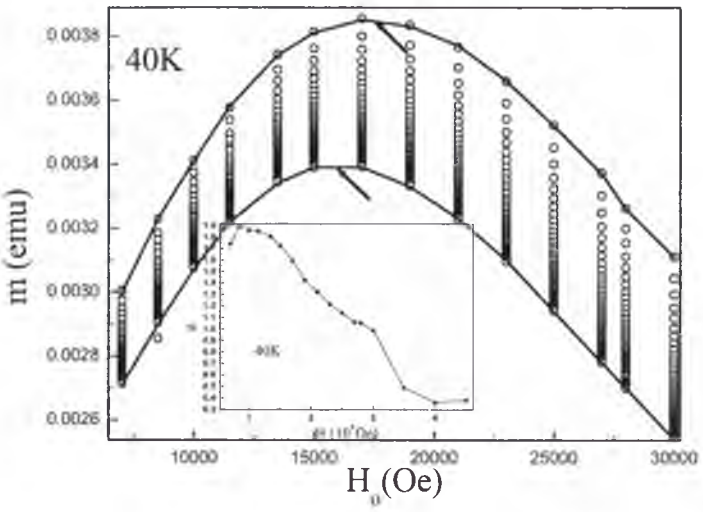

Figure 5.1. 11 The peak field, B_p, decreases with elapsed time as shown by the arrows. The time sequence is 8, 14, 21, 30, 40 and 65 minutes for the curves from top to bottom.

In order to proceed with this dynamical behaviour we need more information to understand the mechanism involved in vortex creep. For this purpose calculation of the vortex-creep activation energy can provide us with some useful and reliable results. Therefore in next section, using the commonly-used method of Maley[34], the activation energy for different fields and temperatures are extracted from the magnetic relaxation data.

5.1.3 Activation Energy and the Critical Exponent

Using Maley's method [34] and the relaxation data from section 5.1.2, one can generate plots of $-k_B T \ln|dM_{irr}/dt|$ vs. M_{irr} at different temperatures for a given applied field. In Maley's method, the decay of magnetic moment is translated to effective activation energy using

$$U_{eff}(M_{irr} \propto J) = -k_B T \ln\left|\frac{dM_{irr}}{dt}\right| + k_B T \ln\left(\frac{H_o x_o \omega}{l\pi}\right), \quad M_{irr} = \frac{m_{irr}}{V} \qquad (5\text{-}4)$$

where $C = \ln(H_o x_o \omega / l\pi)$ is a fitting constant needed to achieve alignment of isothermal data and l, x_o and ω are the thickness of the sample, the flux bundle hopping distance and the attempt frequency, respectively. In the above relation V is the volume of the superconductor. The isotherm plots can be made to form a pseudo-smooth curve by using the additive constant CT. The parameter C, which is assumed to be temperature independent, is determined by the condition that all data set points for the different temperatures have to lie on one smooth curve. Smoothness can only be attained in the low-temperature region, because at higher temperatures a change in the pinning well height has to be taken into account. The obtained C value in Table 5.1.1 ($C \approx 16\text{-}22$) is in the same range as the one for LaSCO [35] and YBCO [36].

For achieving further smoothness in the data, Tinkham's suggestion for the temperature dependence of the activation energy, as $g(t) \sim (1\text{-}t^2)$ with $t = T/T_c$ [37], has been frequently used [37]. However, this method still did not provide perfect alignment of the data in $-k_B T \ln|dM_{irr}/dt| + CT$ vs. M_{irr} plots. Because of this, the van der Beek approach [38] was used in this thesis, which treats $g(T)$ as a fitting function that provides perfect alignment of the data in the $U(M_{irr})$ plot of Figure 5.1.13. Perfect alignment of the isotherms has been achieved by using this correction procedure[38]. The values of $g(T)$ were chosen so that a perfectly smooth $-k_B T \ln|dM_{irr}/dt| + CT$ vs. M_{irr} was obtained, regardless of the temperature at which the measurements were performed [38]. The resultant temperature scaling has been plotted in Figure 5.1.12. The uncertainty in the data is limited to the symbol sizes. Since M_{irr} is

proportional to the current density J, the U_{eff} vs. M_{irr} plots represent the dependence of U_{eff} on the screening current density.

In Figure 5.1.13(a) the calculated activation energy for applied fields of 5000 and 10000 Oe (the inset) is shown on a double logarithmic scale. As can be seen, the data for the applied field 5000 Oe follow a power law function (linear in the log-log plot) with critical exponent $\mu \simeq 0.94$ for the entire temperature range. With increasing applied field, the power law is maintained up to 55K, and a new regime for temperatures above 55K appears [inset of Figure 5.1.13(a)].

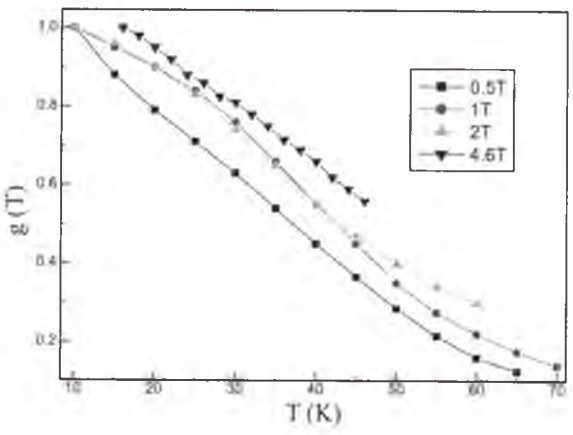

Figure 5.1. 12 Temperature dependence of the effective activation energy as determined from the corrected scaling following adjustment of the C parameter.

This new regime has a smaller critical exponent ($\mu = 0.56923 \pm 0.0061$) in comparison to the corresponding data at 0.5×10^4 Oe. With further increases in the applied field, the extent of the new regime increases whilst the value of the corresponding μ decreases. In Figure 5.1.13(b) and its inset, the data has been presented for fields of 2×10^4 Oe and 4.6×10^4 Oe and a different temperature range.

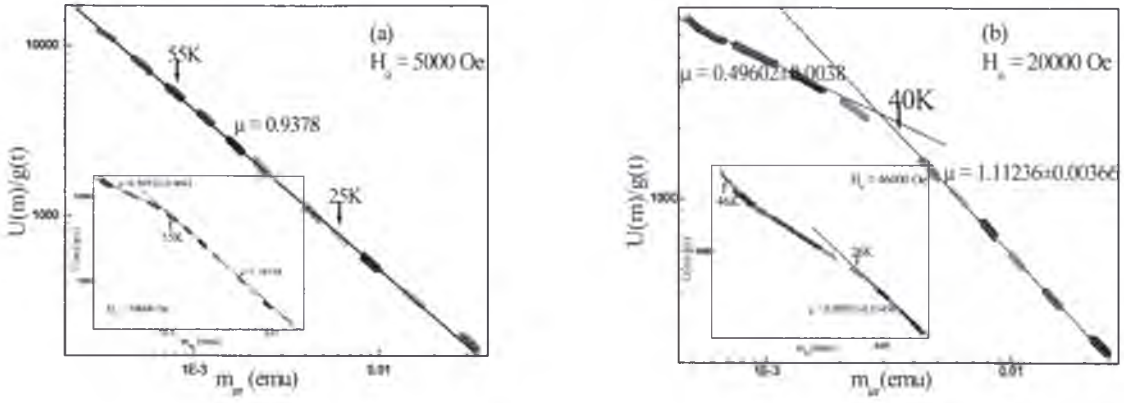

Figure 5.1. 13 Effective activation energy for applied fields plotted in log-log scale: (a) for 0. 5×10^4 Oe the activation energy follows the power law functional with critical exponent $\mu \simeq 0.94$. The inset: at higher field (1×10^4 Oe) the uniformity is not maintained and a new regime appears at temperatures higher than 55K. (b) The extent of the new regime broadens with increasing applied field to 2×10^4 Oe and 4.6×10^4 Oe (the inset).

It must be noted that an upward curvature is associated with the new regime. The accessible temperature for the highest applied field is limited to a maximum of 46K.

Furthermore the data analysis showed that the value of C is an increasing function of the applied field. The values of C and the critical exponent μ for different fields have been tabulated in Table 5.1.1. From the findings in this table it can be seen that the value of μ for high current density (or high m_{irr}) is almost constant, that is 1± 0.1, but at low current density the exponent decreases with increasing applied field.

In collective creep theory, the dependence of $U_{eff}(J)$ reflects the change in the size and the jumping width of the collectively hopping part of the flux line lattice with current. For the 3D, as well as the 2D case, power law behaviour of $U_{eff}(J)$ is predicted and given by equation (3-32), with the characteristic critical exponent μ. In the case of 3D pinning,

which is appropriate for the Tl1223 system, μ = 1/7, 5/2, and 7/9 are proposed for the pinning of single vortices, of small flux bundles, and of large flux bundles, respectively.

Table 5-1- 1 The value of critical exponent μ and parameter C for different applied fields.

Parameters → / Applied field (Oe)	C	Critical exponent μ	
		Low m (or J)	High m (or J)
0.5×10^4	16±1	0.9387±0.01	0.9387±0.01
1×10^4	18±1	0.5692±0.006	1.107±0.01
2×10^4	20±1	0.4960±0.004	1.112±0.004
4.6×10^4	22±1	----	0.905±0.014

In this approach, an interpolation formula as in (3-32) is used. From the functional form of this formula, it can be seen that if the U(J) curve is linearized on a double logarithmic scale, the exponent μ appears as the gradient of the straight line in this double logarithmic representation. A possible transition of μ between two different values results in a deviation from linearity. It must be noted that this method is applicable for the cases where the current density is much smaller than the critical current density, which is usually fulfilled for HTS.

In Figure 5.1.13(a) the double logarithmic plot of $U(m_{irr} \propto J)$ is shown. For 5000 Oe, a straight line with gradient ~ 0.94 fits the data for nearly the whole measured temperature range. At such a low magnetic field the exponent ~ 0.94 is far from the expectation of the collective creep theory, since in this dilute field the interaction between vortices is negligible and an exponent of as small as ~ 1/7 or 0.14 is expected. However, if we compare the temperature range of 10K to 60K and field of 0.5×10^4 Oe in the phase

diagram 5.1.5, we see that these data correspond to the Bragg Glass phase, to which the collective creep theory is not applicable. On progressively increasing the applied field it can be seen that the exponent ~ 1 is preserved for the temperature range below the entanglement line (that is, in the Bragg Glass phase). This result consistently shows that as long as the vortex structure is below the entanglement line no significant change in the vortex system occurs. However, with crossing the entanglement line a new feature in the effective activation energy starts to appear. That is, the critical exponent μ for the temperature and field ranges above the entanglement line, given in the first column of Table 5.1.1, decreases with increasing applied field in agreement with the collective vortex creep theory. From this data, we see that the vortex structure starts with the small bundle regime, which is followed by the large bundle regime. This result once again confirms the results obtained in the previous section, demonstrating that the transition from a quasi-lattice to an amorphous Vortex Glass phase is responsible for the rise of the magnetic moment and appearance of the peak effect.

Due to the restriction on applied field in the MPMS, data above 4.6×10^4 Oe is not accessible, as is shown in Table 5.1.1, and it is not clear whether the critical exponent μ would increase or decrease with further increases in applied magnetic field. That is, from the above data the vortex structure above the peak effect is not accessible. In order to investigate the vortex structure above the peak and compare it with the structure below the peak, the relaxation measurements were performed on an isothermal hysteresis loop at a suitable temperature at which the entire feature of the peak effect is measurable. Figure 5.1.8 shows a typical measurement for three isothermal loops conducted across the peak effect. This feature has been further magnified in Figure 5.1.11. In this part an attempt is

made to understand the mechanisms involved across the peak effect. According to the thermally activated flux motion theory, over the pinning barrier, $U(J)$ can be written as relation (5-4). On manipulating this relation, it can be re-written as

$$U_{eff}(J) = -k_B T \ln\left|\frac{l\pi}{H_o x_o \omega}\frac{dM_{irr}}{dt}\right| \propto -k_B T \ln\left|\frac{1}{H_o}\frac{dM_{irr}}{dt}\right|. \qquad (5\text{-}5)$$

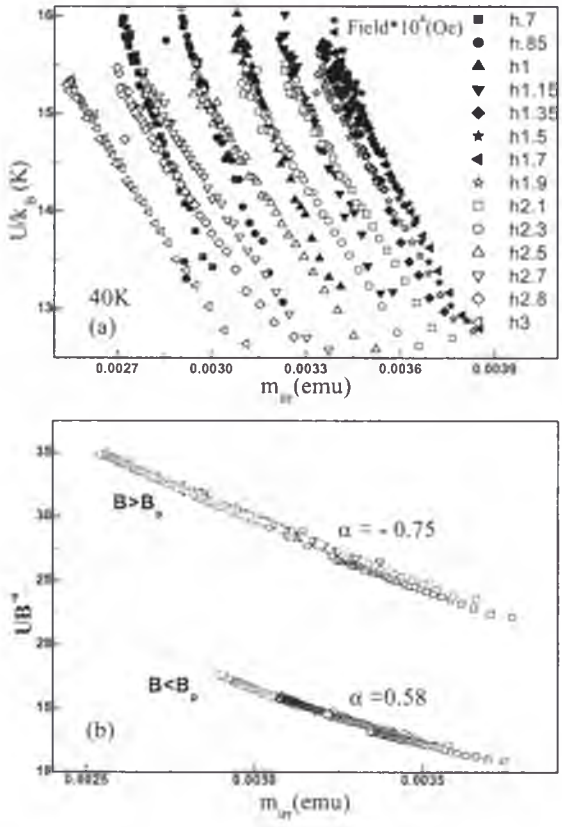

Figure 5.1. 14(a) Activation energy U/k_B versus the magnetic moment for field range $(0.7 - 3) \times 10^4$ Oe at 40K. Note the change in the slope $\partial U/\partial m$ above and below the peak field $H_{peak} \approx 1.7 \times 10^4$ Oe. (b) Scaling of $U(m, H)$ curves below and above the peak. Above the peak $U \propto H^{-0.75}$, and below the peak $U \propto H^{-0.58}$.

Figure 5.1.14(a) shows the effective activation energy as a function of magnetic moment for applied fields in the range of $(0.7 - 3)\times10^4$ Oe at 40K calculated from the above equation. This figure shows a pronounced crossover in the slope $\partial U/\partial m$ around H_{peak} (from the magnetic hysteresis loop $H_{peak} \approx 1.7\times10^4$ Oe at 40K). Following the previous part, we assume that the governing mechanism of vortex dynamics is supplied by the collective vortex creep theory, and then we use the interpolation formula (3- 32) to extract the critical exponent, μ. The inset of Figure 5.1.11 demonstrates the extracted critical exponent using the above assumption. From this figure it can be seen that the critical exponent first increases to a value of 1.9, and then it starts to decrease with further increases in applied magnetic field to the value of about 0.35 at $H_o = 4.6\times10^4$ Oe . Whereas the initial behaviour at low fields below the peak is consistent with the collective vortex creep theory the final value of 0.35 for this exponent at fields above the peak is not. From the observed trend in this figure, further decreases in μ are expected, since it is less likely that it suddenly jumps to higher values. To tackle this behaviour, a field scaling approach on the data in Figure 5.1.14(a) was used to further discriminate and explain the observed behaviour. According to the collective vortex creep theory[30,39], the activation barrier for $J \ll J_c$ (equation (3-32)) can be written as

$$U(H, J) = U_o(H) (J_c / J)^{\mu} \propto H^{\alpha} J^{-\mu}.$$

According to this theory the activation energy $U_o(H)$ must increase with H, which means that the exponent α must be positive[12,40,41]. Figure 5.1.14(b) shows the result of the field scaling of the related data in Figure 5.1.14(a). As can be seen two different exponents with opposite sign are needed to scale the data. Whereas the data below the peak are scaled with

a positive exponent (+0.58) the data above the peak are scaled with a negative exponent (-0.75). Therefore to obtain the function $U_o(H)$ above the peak position, a suitable current dependence functional other than the power law dependence must be used for the data above the peak effect. A "plastic creep model based on dislocation mediated motion of vortices similar to diffusion of dislocations in an atomic solid[42]" has been shown to be a successful model in explaining the data above the peak effect[43]. According to this model the current dependency of the activation energy is described by a finite functional rather than a diverging functional. From the dislocation theory of atomic solids the current dependence of the activation energy can be written as

$$U_{pl}(H, J) = U_{pl}(H)[1-(J/J_c^{pl})^{1/2}]. \qquad (5\text{-}6)$$

Using this relation the field dependence of the activation energy for zero current, that is, $U_{pl}(H)$, can be obtained. Figure 5.1.15 is the result of the fit to relation (5-6).

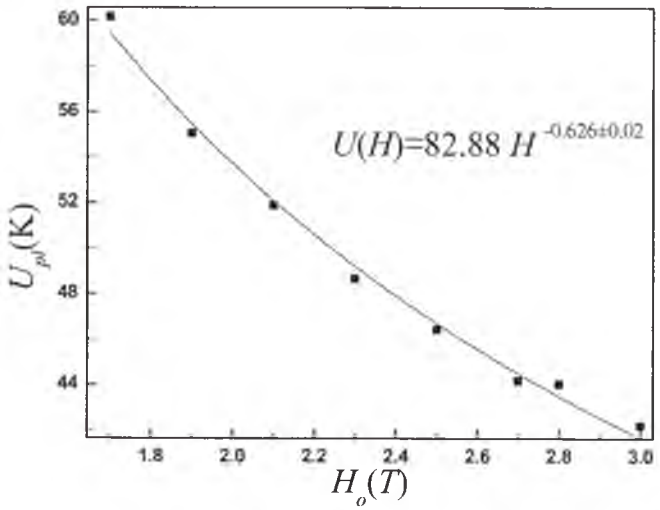

Figure 5.1. 15 Magnetic field dependence of the effective activation energy for zero-current density at 40K. The symbols are the experimental data obtained from Figure (5.1.14)(a) using relation (5-6). The solid line is the best fit to a power law functional, which has been represented on the diagram.

A notable point is the exponent in the field dependence functional, which has been obtained to be $\alpha = -0.62 \pm 0.02$. From plastic shear deformation in relation (3-35), $U_{pl} \simeq \Gamma \varepsilon_o a_o \propto (T_c - T)/\sqrt{H}$, the exponent is $\alpha = -0.5$. Although there is no theory determining the exponent α in H^{α} above the peak, an interpolation formula between the above formula and that introduced by Yeshurun and Malozemoff [37,44,45] leads to

$$U_{pl} \simeq \Gamma \varepsilon_o a_o (a_o / \xi)^{\sigma} \qquad (5\text{-}7)$$

where $0 < \sigma < 1$ and ξ is the in-plane coherence length. Whereas in the Yeshurun-Malozemoff formula $\sigma = 1$, in Geshkenbein theory it takes the value 0. However, from the above interpolation formula, and using $a_o \propto (\Phi_o / H)^{1/2}$, we have $-(1+\sigma)/2 = \alpha$, and in this way α can take values from -0.5 to -1. The calculated exponent -0.62 is, therefore, within an acceptable range from the one introduced by theory, and thus the proximity of the measured exponent to the theoretical exponent is a fingerprint of plastic vortex creep above the peak effect which coincides with the findings in previous parts. It is worth mentioning a few interesting consequences of the theory. Firstly, from this theory, the time dependence of the peak position can be explained. Despite of presence of plastic barriers at low fields, elastic barriers are the governing barriers. With increasing applied field, the plastic barriers start to decrease, and at the peak position they become comparable with elastic barriers. At higher fields at which the plastic barriers fall below the elastic barriers, they start governing the vortex structure, and shear deformations occur. Therefore, at the peak position we can write $U_{el} = U_{pl}$. On the other hand, from the logarithmic solution of classical vortex creep, relation (3-13), elastic barriers are as $U_{el} = k_B T \ln(t/t_o)$. Note that this logarithmic dependency can be investigated experimentally. Shown in Figure 5.1.16 is time dependence of the activation energy on a semi-logarithmic scale. As can be seen the data after about

100 sec show a linear behaviour, which is in accordance with relation (3-13). Equating these two barriers, $U_{pl} = \Gamma\varepsilon_o\, a_o \propto 1/\sqrt{H}$ and $U_{el} = k_B T\ln(t/t_o)$, in the peak position and a given temperature we reach

$H_{peak} \propto [\ln(t/t_o)]^{-2}$

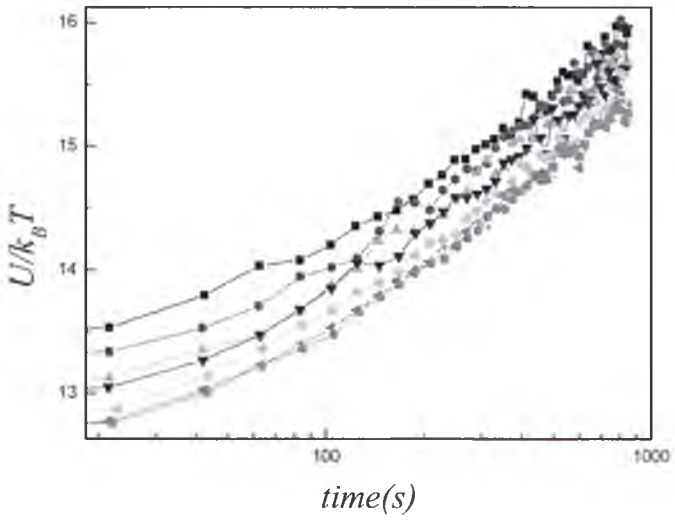

Figure 5.1. 16 Time dependence of the activation energy for different applied fields in a semi-logarithmic scale. The data clearly show a linear behaviour on this scale after about 100 s, which confirms the relation (3-13).

From this relation we see that with passing time the peak position tends to move towards smaller fields, which is consistent with the observed behaviour in Figure 5.1.11. Secondly, from the equality between the elastic and plastic barriers within a given time window the peak position is obtained to be a function of the anisotropy factor, that is, $H_{peak} \propto \Gamma^{-2}$. This relation means that the peak effect in highly anisotropic superconductors must occurs at very low fields whereas for superconductors with 3D structure it should occur at high fields. This finding is also consistent with experimental results. For example, it is well-known that in highly anisotropic Tl(2212) [46] and Bi(2212) [47] structures the peak effect

occurs at low fields whilst for Y(123) [48,49], MgB_2[50,51] and all RE(123) [52-54] superconductors with low anisotropy factors (3D structure) it happens at high fields. Thirdly, the temperature dependence of the peak effect line, $H_{peak}(T)$, can be extracted within the above context. According to the above equations we have $H_{peak} \propto \varepsilon_o^2 \propto \lambda_L^{-4}$. In this relation, the expression $\varepsilon_o = (\Phi_o/4\pi\lambda_L)^2$ has been used. Then the temperature dependence of the peak effect line, $H_{peak}(T)$, is determined through the temperature dependence of the magnetic penetration depth, $\lambda_L(T)$. Using the temperature dependence of $\lambda_L(T)=\lambda_L(0)[1-(t)]^{-1/2}$, where $t = T/T_c$, shows the best fit to the peak position data. The temperature dependence of the peak position is, then, found to be as $H_{peak}(T) = H(0)[1- (T/T_c)]^2$. Figure 5.1.17 is the temperature dependence of the peak position on a double logarithmic scale. As can be seen in this figure, the data satisfactorily show a linear behaviour. That is, the obtained exponent of 1.934 is very close to the theoretical prediction, 2.

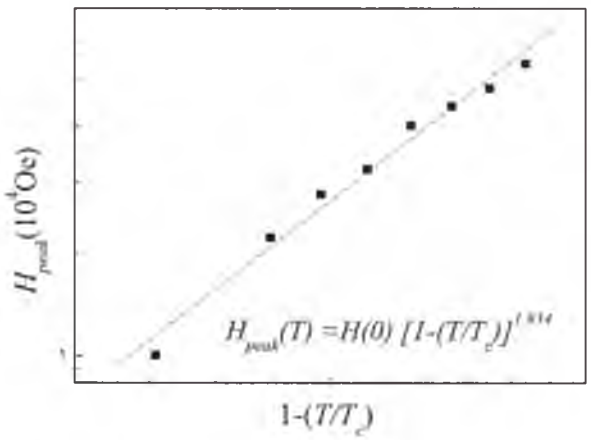

Figure 5.1. 17 Temperature dependence of the peak effect on a log-log scale. The symbols are experimental results and the solid line is a fit to the relation $H_{peak}(T) = H(0)[1- (T/T_c)]^2$.

The quadratic dependence of not only the peak effect line, but also the irreversibility line, on temperature seems to be consistent with the idea of considering the peak effect as a precursory phenomenon for melting of the vortex structure. Since from the melting theory and using the *Lindeman* criterion, $u \approx ca_o$, a quadratic functional on temperature is obtained for the melting line[30]. Therefore, it is unlikely that this quadratic functional for both lines is co-incidental.

5.1.7Anisotropy Factor and the E(*J*) Characteristics

Tackling the vortex dynamics of a material necessitates that we have some information about the structural properties. In the previous section we frequently used an anisotropy factor of 13. The common and usual technique to calculate this factor is to calculate the ratio of the upper critical fields for two principal directions. In this investigation, due to the small size of the sample, calculation of the upper critical field using *dc* magnetization $m(T)$ measurements were accompanied by strong fluctuations preventing the calculation of H_{c2}. The lower critical fields ratio $\Gamma^{-1} = H_{c1}^{c} / H_{\perp 1}^{ab}$, therefore, was measured to gain some idea of the extent of the anisotropy of the sample. Figure 5.1.18 presents the virgin curve $m(H)$ measured at 5K for the two principal directions, that is along the *c*-axis and the *ab*-plane. It should be noted that this measurement was performed after the PPMS was quenched to avoid any remanent magnetic field. Furthermore, in order to minimize the effect of any probable remanence in comparison to the principal signal, the temperature of 5K was chosen. The employed sweep rate was 10 Oe/s. The field at which the deviation from linearity occurred was designated as H. Correcting this field by the demagnetisation factor[55], the values of H_{c1} for two principal directions were determined. The ratio of the values of H_{c1} for the two directions of the

external field in regard to the crystal gave an anisotropy factor of $\Gamma^{-1} \approx 13$. Under some circumstances in a layered superconductor a vortex line can be considered as consisting of two dimensional pancake vortices confined in CuO layers (section 3.1.2). The condition for an intrinsically anisotropic superconductor like Bi(2212) can feasibly be satisfied[56]. However, this condition for a moderately anisotropic superconductor like Tl(1223) family is not so clear. Enhancing the applied field or temperature may lead to the weakening of the Josephson and magnetic coupling between the layers and consequently a decoupling transition known as dimensional crossover might occur even in the latter family. This possibility must be examined, especially when it seems that some of the obtained constants or quantities are consistent with this crossover. In 2D collective vortex creep theory, for instance, the exponents $\mu = 9/8$ and 1/2 are assigned to single and collective pancake vortex creep, respectively. Coincidence of the experimentally determined exponents 1.1 and 0.5 in Table 5.1.1 with the above exponents might be interpreted as an indication of 3D to 2D dimensional crossover rather than elastic to plastic crossover as a result of increasing temperature and field. In order to examine this possibility, application of vortex glass theory characterized by a glass transition temperature T_g might be a clarifying treatment. However, application of this theory using the temperature $T_g = 0$ and various scaling parameters defined in this theory did not result in any convincing scaling.

In an alternative approach Dekker et al. [57] reported that the non-linear transport characteristics of a strongly layered superconductor in a high field could be rather different from those at zero field and from those in a bulk (3D) system in high fields. Their findings provide experimental evidence for the existence of a finite 2D vortex glass correlation length, which diverges at $T_{g,2D} = 0$ K with a scaling law,

$$\frac{E}{J}\exp\left[\left(\frac{T_o}{T}\right)^p\right]=g\left(\frac{J}{T^{1+\upsilon_{2D}}}\right) \qquad (5\text{-}8)$$

where T_o is a field dependent characteristic temperature and the dimensionless parameter $p \leq 1$ for the thermally activated flux creep regime [58]. In order to investigate the dimensional structure of the vortex lattice, a scaling analysis of the $E(J)$ characteristics using the above equation needs to be performed. For this purpose the magnetic relaxation data obtained from a contactless induction measurement was translated into the voltage - current (or equivalently electric field - current density) characteristics.

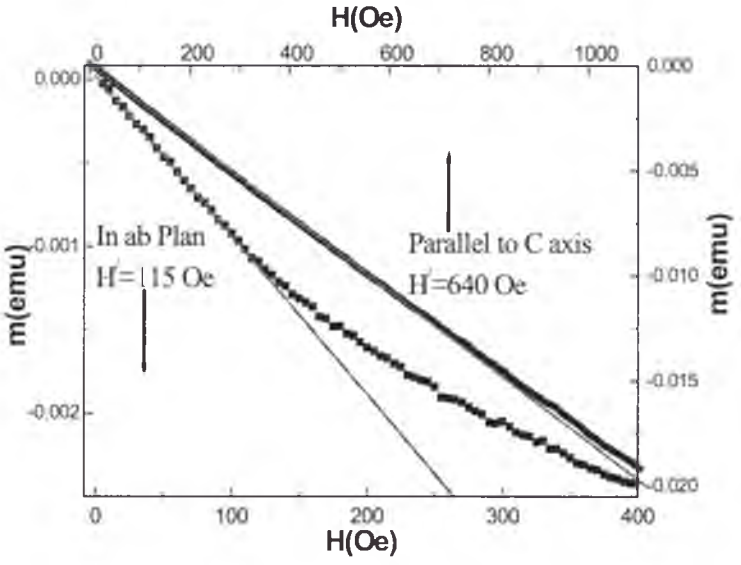

Figure 5.1. 18 Virgin curves in the two principal directions, that is, along the *c*-axis and *ab*-plane. H′ is the field corresponding to the onset of the deviation of magnetic moment data from linearity. After applying the demagnetisation factor, the ratio of the two lower critical fields was determined to be about 13.

For pursuing this, sample geometry effects must be taken into account. From the Bean critical state model (relation (5-1)) magnetic moment is converted into current density. (It must be kept in mind that the value of magnetic moment in this equation must be halved for

relaxation data.) Meanwhile, from Faraday's induction law and for a constant applied magnetic field we have

$$E = -\alpha\mu_o\left[\frac{\partial M_{irr}}{\partial t} + \frac{\partial H_a}{\partial t}\right] = -\alpha\mu_o \frac{\partial M_{irr}}{\partial t} \qquad (5\text{-}9)$$

where $\alpha \equiv bd / (2b+2d)$ [7] is an approximate value for rectangular shaped samples. This is derived from Maxwell's equations and M_{irr} is the irreversible component of the magnetization. The second term in the above relation has been put zero, since the applied magnetic field is constant. Figure 5.1.19 shows typical E - J characteristics on a double logarithmic scale calculated at 4.6×10^4 Oe for different temperatures between 16 - 46K with an increment of 2K.

Two-dimensional vortex glass scaling, equation (5- 9), with different parameters, also did not map the data onto a smooth curve. From Figure 5.1.19, which has emerged from the best parameters examined, the existence of the 2D vortex state is not conclusive for the data sets, which are above the peak position. However, a similar scaling for strongly layered $Tl_2Ba_2CaCu_2O_8$ performed by Wen et al. led to a well-aligned curve [59], showing that in the highly anisotropic 2212 structure dimensional crossover is likely as a result of enhancing field or temperature. The possibility of this crossover in the Tl1223 sample can be investigated by further calculation of the necessary field value to destroy the electromagnetic coupling between the layers. According to the theory the dimensional crossover field is predicted to be $H_{cr} \approx \Phi_o \Gamma^2 d^{-2}$ [60], where d is the distance between CuO_2 planes.

By noticing that $d = 9.55$ Å [29], considering the obtained range $\Gamma^{-1} \simeq 13$, H_{cr} is obtained to be above 7×10^4 Oe, which is higher than the applied fields in this work. This result shows

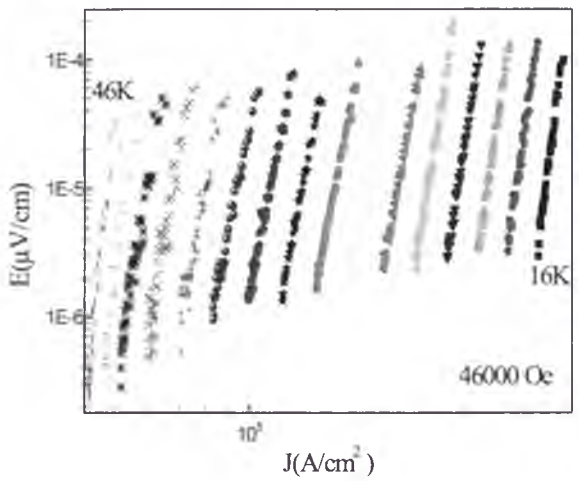

Figure 5.1. 19 The *E* - *J* characteristics in a double logarithmic plot determined at 4.6×10^4 Oe. Each curve is an isotherm, ranging from 16 to 46K (right to left) with an increment of 2K.

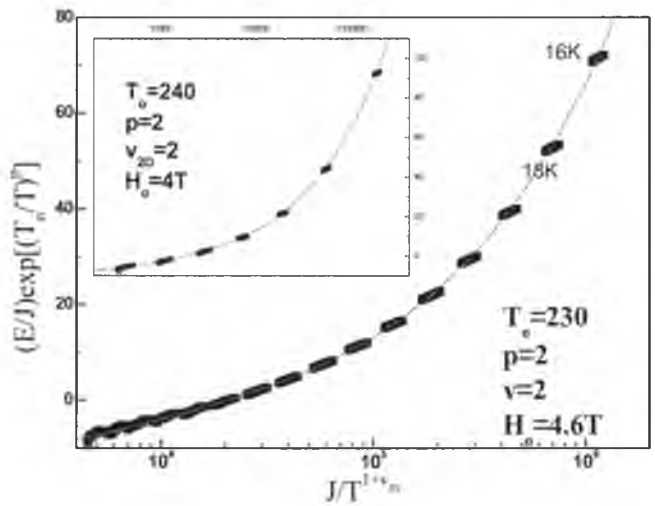

Figure 5.1. 20 Scaling analysis of the data in Fig. 5.1.18 for Tl1223 sample using 2D vortex glass theory (Equation (5-8)) with a characteristic temperature T_o = 230K, and p = 2 ± 0.1, v = 2 ± 0.2 for H_o = 4.6×10^4 Oe. The inset shows the same scaling for a field of 4×10^4 Oe. From the lack of scaling for the data above the peak position (the lowest part of the curves), the possibility of dimensional crossover is ruled out.

that the applied fields in this work are not able to remove the strong Josephson coupling and magnetic attraction between the layers, and thus dimensional crossover is not plausible. In this way the idea of the occurrence of plastic shear deformations at high field above the peak effect rather than the decoupling of the layers and dimensional crossover is more reinforced.

5.2 $Sm_{1+x}Ba_{2-x}Cu_3O_{6+y}$ (x = 0.04) Single Crystal

The size of the sample with almost rectangular geometry that was studied was $0.514\times1.773\times2.101$ mm^3. All of the measurement trends and techniques are almost the same as for the Tl(1223) sample, unless otherwise stated. As was investigated in section 4.2.2 the sample is highly twinned.

Due to the complexity of twin plane behaviour in different temperatures, fields, and orientations, dealing with a topic related to twin planes is not an easy task. This complexity has led the researcher to sometimes contradictory conclusions about the twin plane influence on pinning and consequently on current density. For example, in contrast to Duran et al. [61] who found the twin planes to be channels that ease the flow of vortices, Vlasko Vlasov et al. [62] found them to be barriers. Kwok et al. found the twin planes to promote the effect of pinning [63]. However, the effect of the pinning of the twin planes has been found to be temperature dependent[64-66]. In the following section an alternative technique taking the emerging features into account is introduced for finding the so-called lock-in angle from the angular dependence of the hysteresis loop.

5.2.1 Magnetic Hysteresis Loop and Temperature Dependence of Magnetic Moment

Figure 5.2.1 demonstrates the temperature dependence of the magnetic moment data collected through Field-Cooled (FC) and Zero-Field-Cooled (ZFC) processes for the case where the applied magnetic field is parallel to *c*-axis. From this type of measurement two quantities of the upper critical field and irreversibility field can be determined. From these

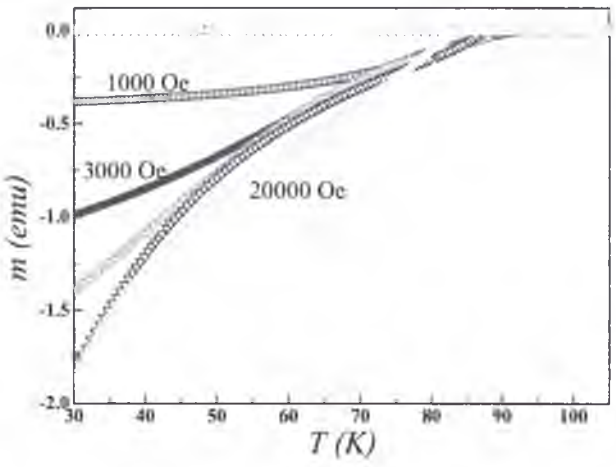

Figure 5.2. 1 $m(T)$ data for the twinned $Sm_{1.04}Ba_{1.96}Cu_3O_{6+y}$ single crystal collected through a ZFC-FC process at different applied fields for H_o||c-axis.

data, the onset of deviation from the magnetic moment value above T_c with the criterion $\Delta m = 5\times10^{-4}$ *emu* was selected to determine the upper critical field. The merging point of the ZFC and FC curves with the same criterion of the upper critical field was used to obtain the irreversibility field.

Similar measurements were performed for the case where the applied magnetic field was parallel to the *ab*-plane. Figure 5.2.2 shows the temperature dependence of the upper critical field and the irreversibility line for the two principal directions. The ratio of the two upper critical fields is obtained to be ~10, which is of the same order as the anisotropy parameter for Y(123) [67] and Tl(1223) in the previous section.

The irreversibility line for the case H_o||c-axis was found to change as $(1- T/T_c)^n$, where $n = 1.49$, which is of the same order as what was found for $Nd_{1+x}Ba_{2-x}Cu_3O_{6+y}$ single crystal by Pradhan et al. ($n = 1.46\pm0.16$) using ac-susceptibility measurements[54]. The irreversibility line in their recent report is believed to be a solid/liquid transition line.

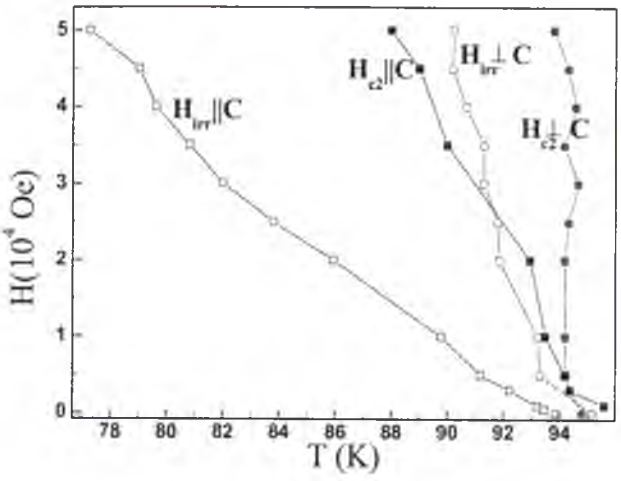

Figure 5.2. 2 Temperature dependence of the irreversibility field, $H_{irr}(T)$, and the upper critical field, $H_{c2}(T)$, in the two principal directions for $Sm_{1.04}Ba_{1.96}Cu_3O_{6+y}$ single crystal.

The irreversibility line might be under the influence of several factors such as the anisotropy and the Ginzburg-Landau parameter[30]. Oxygen reduction, for instance, changes these properties. In this way the exponent *n* depends on the oxygen content of the sample. The value of this exponent in reference [54] has been assigned to the vortex glass regime. Correlated disorder such as columnar defects[68,69] and twin planes[70] (which will be investigated in later sections) also can have a considerable influence on the irreversibility line.

Using a 9T PPMS-magnetometer, the hysteresis loop was measured from 5K up to 90K (Figure 5.2.3) with an increment of 5K (not all shown here). This measurement was performed with a sweep rate of 50Oe/s, and for each loop, before starting the data collection, a maximum field of 8.5×10^4 Oe was applied to ensure that the sample was fully penetrated by the field. From these data, the second peak effect can be detected from 25K and persists up to 85K. (Since the peak effect at temperatures between 25-50K is too broad

and due to the employed scale for a group of loops, the peak effect is not so obvious for those temperature in this Figure. However, it can be detected at each isothermal if it is looked at individually under magnification.) This peak shifts to lower field with increasing temperature.

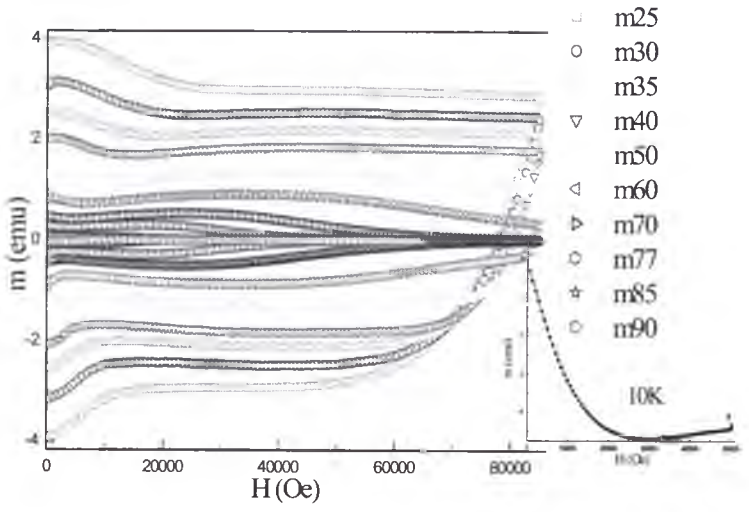

Figure 5.2. 3 $m(H)$ loops measured from 25K to 90K with an increment of 5K for H || c-axis for highly micro-twinned Sm123 single crystal. The second peak effect at 77 and 85K is clearly seen. The inset: the virgin curve at 10K. The minimum occurs at around 3×10^4 Oe, so for achieving full penetration, application of a field of about 9×10^4 Oe is necessary.

Despite the accessibility of magnetic field up to 8.5×10^4 Oe, full penetration status is not achieved at low temperatures up to 10K. In order to determine the full penetration field, the virgin curve was measured at 10K. From this measurement (the inset of Figure 5.2.3) the minimum in $m(H)$ occurs at about 3×10^4 Oe, and therefore the full penetration field, which depends on the sample size and should be three times of the minimum field[1], was determined to be about 9×10^4 Oe.

Since extended defects are directional pinning centres, the dominant defect structure can be determined by changing the angle between the applied field and the extended defects [71]. Figure 5.2.4 shows the magnetic hysteresis (*m-H*) loops recorded with the applied field (H_o) inclined at various angles φ (measured relative to the *c*-axis) at 89.5 K.

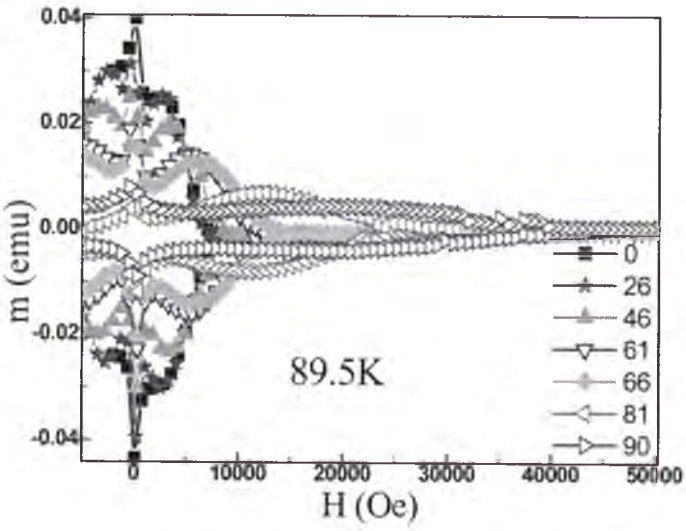

Figure 5.2. 4 Angular dependence of hysteresis loop at 89.5K. The angle between H_o and the c-axis varied between 0° and 90°.

Due to lack of the angular-dependent-measurement accessory in PPMS this measurement was performed with MPMS, in which the maximum accessible field is 5×10^4 Oe. The temperature of 89.5 K was the lowest temperature for which the closure of the loop for φ = 90° for the highest accessible field (5×10^4 Oe) was possible. Finding the closure status was necessary to be able to calibrate the angular dependency accessory. It can be seen that the *m-H* loops display the second peak effect over the entire angular range of $0° < \varphi \leq 90°$.

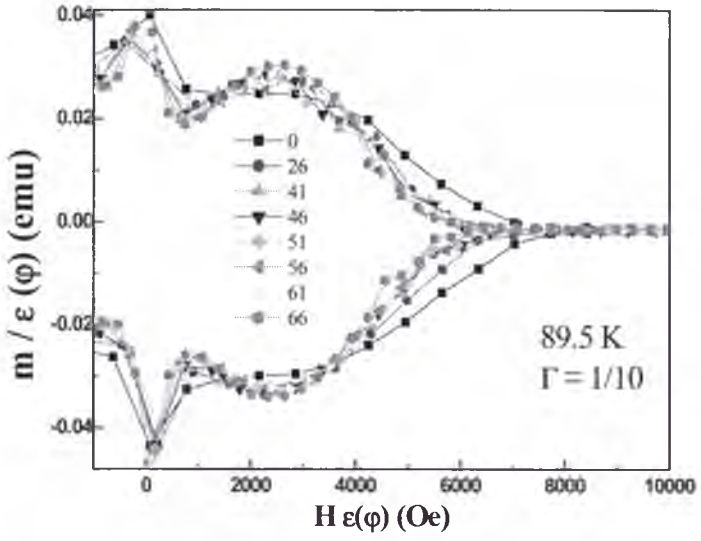

Figure 5.2. 5 Scaling of the data in Figure (5.2.4) from 0° to 66° revealed that the loops for angle 0° and close to it (not shown here) cannot be scaled with other loops.

Since the investigation of disorder and in particular twin planes in HTSs is always accompanied by some intrinsic anisotropic properties related to their layered structure, the analysis of these systems must be carried out with care. In order that these intrinsic properties are not confused with the effects of twin boundaries, their effect must be taken into account. Using Blatter's approach [72], an anisotropic superconductor can be mapped onto an isotropic superconductor using a scaling method which was explained in Chapter 3. In this approach, the measured hysteresis loop must be scaled using $H\varepsilon(\varphi)$ and $m/\varepsilon(\varphi)$, where $\varepsilon^2(\varphi) = \cos^2\varphi + \Gamma^2\sin^2\varphi$, where Γ is the anisotropy parameter, which from the previous part was determined to be $\Gamma^{-1} \approx 10$ for the present sample. Using this scaling approach they were scaled as in Figure 5.2.5. The results of the scaling for angles from 0° to 90° showed that all loops except for the ones close to $\varphi = 0°$and 90° are well scaled (For clarity the loops for angles close to 90° haven't been shown.). It is said that for twinned

superconductors the vortex dynamics for angles above a particular value called the *lock-in angle*, φ_L, assumes a zigzag shaped pattern (kinked vortices) up to the so-called *trapping angle*, φ_t [30]. Oussena et al. showed that for angles below the trapping angle vortices are trapped at the twin planes with the vortex system forming a Bose glass phase, while with increasing angle vortices are liberated from the twin planes and point disorder becomes the dominant type of pinning site, and therefore a transition to the vortex glass regime occurs [73]. The overlap of the scaled hysteresis loops (Figure 5.2.5) for the angles φ between $\varphi = 0°$ and 90° (but not close to these angles) shows that the isotropic point disorder has the dominant role in governing the vortex dynamics in this angle range. On the other hand, the twin and CuO_2 planes determine the vortex dynamics for the extreme cases of $\varphi \approx 0°$and 90°, respectively. It must be borne in mind that the concentration in this work is on the twin planes, and the effect of the CuO_2 planes is not investigated.

Correlated disorder such as twin planes transforms the irreversibility transition into a Bose-glass transition with a cusp-like maximum of $H_{irr}(\varphi)$ at $\varphi = 0°$, whilst in a twin-free sample the irreversibility field has a minimum at $\varphi = 0°$ and the field increases toward $\varphi = 90°$. The cusp appears around $\varphi = 0°$, within the angular range φ_L [53,74,75]. The measurement of the angular dependence of H_{irr} has been the principal method used to study the locking of magnetic vortices by twin planes and the determination of φ_L. However, due to the high irreversibility field of 123 systems, such measurements could be conducted only at high temperatures, close to T_c, at which the irreversibility field is subject to a high degree of uncertainty. Further, H_{irr} is defined by an arbitrary value of magnetization, at which the ascending and descending branches of the magnetic hysteresis loop, or the ZFC and FC

branches of the temperature dependence of the magnetization, are seen to merge. Because of this, it is highly desirable to develop a new method for obtaining $\varphi_{\perp}$ that relies on universal physical principles instead of arbitrary definitions. Such a method is presented in this work.

The angular dependence of the irreversibility field was determined according to the method outlined in section 4.1 using the hysteresis loop data from Figure 5.2.4. Figure 5.2.6 shows the results of this measurement, which was carried out at 89.5K. For angles close to 0° and in the range dominated by the twin planes the loop measurements were perform with smaller angle increments to extract any probable cusp-like dependence of the irreversibility field on angle. Despite the presence of a high density of twin planes (refer to Figure 4.10) no cusp-like feature could be isolated due to strong noise close to the irreversibility field. The inset, which is the enlarged part around the angle $\varphi = 0°$, clearly shows no cusp like feature.

In order to investigate the lock-in transition for twin boundaries in the sample, several hysteresis loops for angles between 0° to 16° with a 0.5° increment were measured. (For angles close to 0°, the increment 0.2° was employed.) Figure 5.2.7 is the result of these measurements. Despite the presence of some irregularities around the irreversibility field, there is an interesting trend around the peak effect and the field below the peak effect that appears on changing the angle. This feature has been magnified in the inset of Figure 5.2.7. From this figure two opposite trends on two sides of the convergence point are observed around 0.18T. With further inclination towards the *c*-axis, the peak effect is gradually suppressed and, in contrast, the minimum in the magnetic moment at fields lower than H_{peak} gradually eliminates.

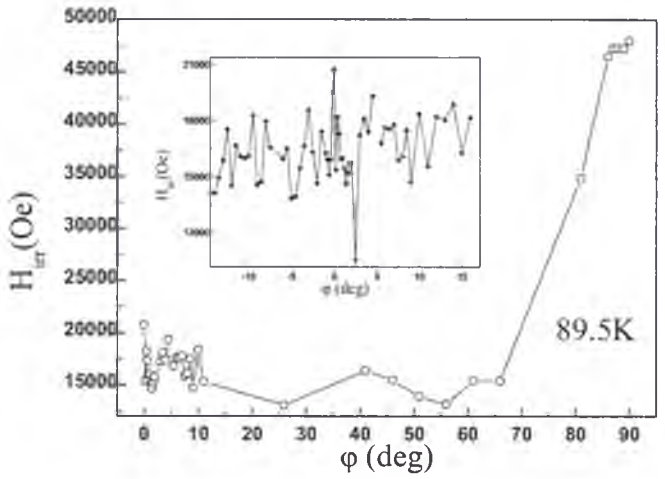

Figure 5.2. 6 Angular dependence of the irreversibility field at 89.5K. No cusp-like dependence of the irreversibility field at φ = 0° could be detected. The inset shows the angles close to φ = 0° on a magnified scale.

In what follows it is shown that despite the gradual and smooth change in loops with angle, they are separated via a scaling process similar to what was performed in Figure 5.2.5, and they form two distinct groups. Formation of these two distinct groups is representative of the presence of two different mechanisms involved in the pinning of vortices. Figure 5.2.8 shows (which is the major and new result of the second section of this chapter) a similar scaling as what was performed on loops - for different angles from 0° to 66°- in Figure 5.2.5.

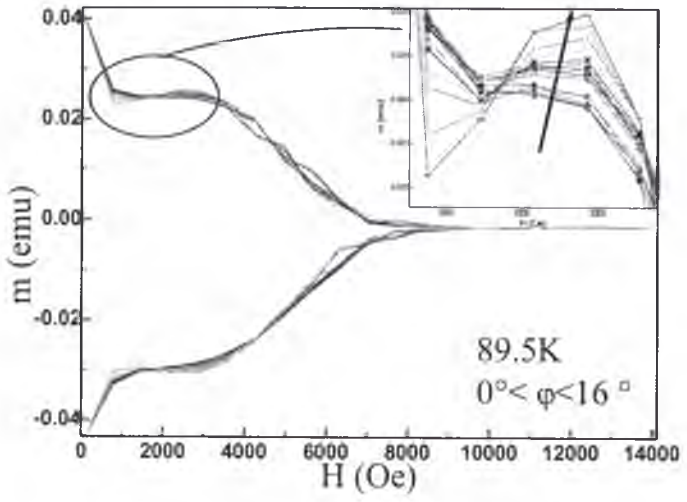

Figure 5.2. 7 Angular dependence of hysteresis loops for angles 0° < φ <16° with 0.5° angular increment. The angle is measured relative to the c-axis. For angles close to 0° the increment is 0.2°. The inset: enlarged scale of the marked area. The arrow direction points out the increase of angle from 0° to 16°. Whereas the peak effect is suppressed with further inclination towards the c-axis the minimum in *m* at low fields is smoothly eliminated.

The scaling on these loops gives rise to two groups, those for φ between 0° and 6° and those for φ above 6°. Whereas the minimum at low fields and the maximum (i.e. the peak effect) are clearly seen for the latter group, the former group does not exhibit a pronounced anomalous peak effect. Because the scaling divides the hysteresis into two groups and the loops are angle independent within each of the groups, two separate mechanisms are responsible for the observed hysteresis loops. Disappearance of the minimum for fields smaller than H_{peak} at φ<6° (in Figure 5.2.7) confirms that the twin planes are effective pinning centers at low fields and high temperatures when the twin spacing matches the mean vortex distance.

Disappearance of the low-field minimum at φ < 6°, in Figure 5.2.8, might be a confirmation of the twin planes as effective pinning centers at low fields, when the twin

spacing matches the mean vortex distance (matching effect) [54]. The vortex lattice parameter can be calculated via $a = (\Phi_o/H)^{1/2}$, where Φ_o is the magnetic flux quantum with value 2.07 $\times 10^{-7}$ Oe cm^{-2}. For fields between 700-1800 Oe, the parameter is obtained to be $\leq$ 17 μm, which is among the measured twin plane spacings (section 4.2.2). A low-field peak in the double peak structure of a defect-free $Nd_{1+x}Ba_{2-x}Cu_3O_{7-\delta}$ single crystal is ascribed to the matching effect by twin planes by Pradhan et al. and Jirsa et al. [54,76,77], however, for the sample under investigation in this work, the effect of the twin planes does not appear as an extra peak but as the elimination of the observed minimum in the very low field region.

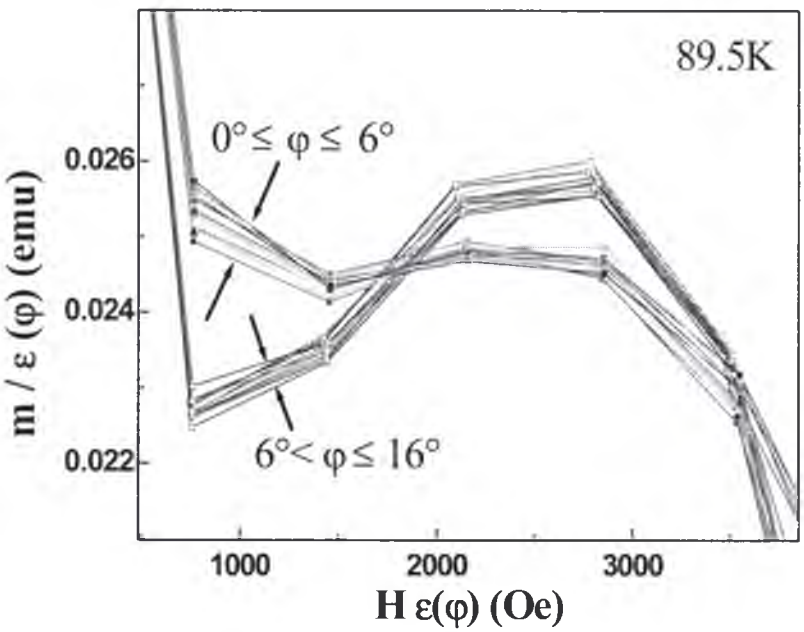

Figure 5.2. 8 The scaled magnetic hysteresis loops around the peak effect for angles from 0° to 16° with 0.2° increment. From the scaling of the loops in Figure (5.2.7) they were divided into two scaled groups; from 0° to 6° and from 6° to 16°.

The reason for the suppression of the peak effect within the lock-in angle range, which has also been observed by others[77], is not still quite clear. Some researchers believe

that it is a result of channeling or shearing of vortices along the twin walls [74,78-80]. Alternatively, redistribution of the critical current pattern in the sample is proposed as the mechanism responsible for reduction of the critical current density around the peak effect [77].

The important result of the scaling performed on the hysteresis loops measured at different values of φ is that the value of the lock-in angle was determined to be $6°\pm0.1°$. For angles far above $\varphi \sim 6°$, the pinning is dominated by the isotropic point disorder, resulting in the vortex glass structure. In this way, a new method is established to determine the lock-in angle. The main advantage of this method, due to the sharp transition in the hysteresis loop feature, is that the uncertainty in determining the lock-in angle is lower than with the conventional applied method using the angular dependence of the irreversibility field. This method for obtaining φ_L was performed with a scaling based on the anisotropy factor (Γ), which was determined by the ratio of the two upper critical fields. These fields are themselves defined by an arbitrary criterion. However the splitting of the scaled hysteresis loops into two groups occurred at the same value of φ_L, regardless of the criterion employed for H_{c2}. It should be noted that the twin planes are effective pinning centres at high temperatures [62,66,81]. Therefore, the method we have presented for obtaining φ_L can be used only at temperatures relatively close to T_c, which is actually an advantage for this method, since at high temperatures we always face significant noise, which makes the determination of the lock-in angle by other methods a non-trivial task.

The Bose-glass theory predicts a cusp-like dependence of the irreversibility field on the angle φ with a maximum at $\varphi = 0°$ to be a signature of the second order two-dimensional melting of the Bose glass [13,53,79]. However the strength of the cusp itself

depends on the properties of the twins and on the strength of the uncorrelated defect structure. For example, oxygen reduction or the presence of impurity content might lead to formation of defects on the twin wall which destroys the perfection of the twin planes. Due to the large experimental uncertainty in determining the merging point of the upper and lower branches of the hysteresis loops in Figure 5.2.4, accurate determination of H_{irr} was not possible. In addition, the superposition of the effect of a massive amount of twins and type of twins that makes them to act in a somewhat incoherent way may be responsible for weakening the cusp, so that it is not detectable.

References

1 Y. Yeshurun, A. P. Malozemoff, and A. Shaulov, Rev. Mod. Phys. **68,** 911 (1996).

2 C. P. Bean, Rev. Mod. Phys. **36,** 31 (1964).

3 F. A. List, D. M. Kroeger, and V. Selvamanickam, Physica C: Superconductivity **275,** 220-230 (1997).

4 B. A. Glowacki, Cryogenics **37,** 609-613 (1997).

5 Z. X. Cheng, X. L. Wang, S. Keshavarzi, M. J. Qin, T. M. Silver, H. K. Liu, H. Kimura, and S. X. Dou, Supercond. Sci. Technol. **17,** 696 (2004).

6 L. Krusin-Elbaum, L. Civale, V. M. Vinokur, and F. Holtzberg, Phys. Rev. Lett. **69,** 2280 (1992).

7 M. J. Qin, A. W. Kaiser, and H. J. Bornemann, Physica C **311,** 280 (1999).

8 T. Nabatame, Y. Saito, K. Aihara, T. Kamo, and S. Matsuda, Supercond. Sci. Technol. **9,** 17 (1996).

9 W. Harneit, T. Klein, C. Escribe-Filippini, R. H., J. M. Broto, A. Sulpice, R. Buder, J. Marcus, and W. Shmidbauer, Physica C **267,** 270 (1996).

10 Y. Yeshurun, N. Bontemps, L. Burlachkov, and A. Kapitulnik, Phys. Rev. B **49,** 1548 (1994).

11 D. N. Zheng, A. R. Johnson, J. D. Campbell, A. M. Liang, T. Doi, M. Okada, and K. Higashyama, J. Appl. Phys. **77,** 5287 (1995).

12 A. A. Zhukov, H. Küpfer, G. Perkins, L. F. Cohen, A. D. Caplin, S. A. Klestov, H. Claus, V. I. Voronkova, T. Wolf, and H. Wühl, Phys. Rev. B **51,** 12704 (1995).

13 H. Küpfer, T. Wolf, C. Lessing, A. A. Zhukov, X. Lancon, R. Meier-Himer, W. Schauer, and H. Wuhl, Phys. Rev. B **58,** 2886 (1998).

[14] A. Erb, J.-Y. Genoud, F. Marti, M. Däumling, E. Walker, and R. Flükiger, J. Low Temp. Phys. **105,** 1023 (1996).

[15] M. Däumling, J. M. Seuntjens, and D. C. Larbalestier, Nature **346,** 332 (1990).

[16] A. Wisniewski, R. Szymczak, R. Puzniak, M. Baran, J. Karpinski, and H. Schwer, Czech. J. Phys. **46,** 1651 (1996).

[17] W. Mexner, J. Hoffmann, S. Heede, K. Heinemann, H. C. Freyhardt, F. Ladenberger, and E. Schwarzmann, Z. Phys. B **101,** 181 (1996).

[18] Y. C. Kim, J. R. Thompson, D. K. Christen, M. Paranthaman, and E. D. Specht, Physica C **253,** 357 (1995).

[19] K. K. Uprety, J. Horvat, X. L. Wang, M. Ionescu, H. K. Liu, S. X. Dou, and E. H. Brandt, Phys. Rev. B **65,** 224501 (2002).

[20] G. Yang, P. Shang, S. D. Sutton, I. P. Jones, J. S. Abell, and C. E. Gough, Phys. Rev. B **48,** 4054 (1993).

[21] D. Giller, A. Shaulov, R. Prozorov, Y. Abulafia, Y. Wolfus, L. Burlachkov, Y. Yeshurun, E. Zeldov, V. M. Vinokur, J. L. Peng, and R. L. Greene, Phys. Rev. Lett **79,** 2542 (1997).

[22] D. Giller, A. Shaulov, Y. Yeshurun, and J. Giapintzakis, Phys. Rev. B **60,** 106 (1999).

[23] G. P. Mikitik and E. H. Brandt, Phys. Rev. B **64,** 184514 (2001).

[24] D. Ertas and D. R. Nelson, Physica C **272,** 79 (1996).

[25] V. M. Vinokur, B. Khaykovich, E. Zeldov, M. Konczykowaski, R. A. Doyle, and P. H. Kes, Physica C **295,** 209 (1998).

[26] V. Hardy, A. Wahl, A. Ruyter, A. Maignan, C. Martin, L. Coudrier, J. Provost, and C. Simon, Physica C **232,** 347 (1994).

[27] A. Wahl, V. Hardy, J. Provost, A. Buzdin, and C. Simon, Physica C: Superconductivity **250,** 163-169 (1995).

[28] A. Wahl, A. Maignan, V. Hardy, J. Provost, C. Simon, and B. Raveau, Physica C: Superconductivity **244,** 341-348 (1995).

[29] A. Maignan, C. Martin, V. Hardy, and C. Simon, Physica C **228,** 323 (1994).

[30] G. Blatter, M. V. Feigel'man, V. B. Geshkenbein, A. I. Larkin, and V. M. Vinokur, Rev. Mod. Phys. **66,** 1125 (1994).

[31] A. Gurevich and H. Küpfer, Phys. Rev. B **48,** 6477 (1993).

[32] J. R. Thompson and Y. R. Sun, Phy. Rev. B **49,** 13287 (1994).

[33] T. Aouaroun and C. Simon, Phys. Rev. B **58,** 11692 (1998).

[34] M. P. Maley, J. O. Willis, H. Lessure, and M. E. McHenry, Phys. Rev. B **42,** 2639 (1990).

[35] M. E. McHenry, S. Simizu, H. Lessure, M. P. Maley, J. Y. Coulter, I. Tanaka, and H. Kojima, Phys. Rev. B **44,** 7614 (1991).

[36] J. R. Thompson, L. Krusin-Elbaum, L. Civale, G. Blatter, and C. Feild, Phys. Rev. Lett. **78,** 3181 (1997).

[37] M. Tinkham, Phy. Rev. Lett. **61,** 1658 (1988).

[38] C. J. van der Beek, P. H. Kes, M. P. Maley, M. J. V. Menken, and A. A. Menovsky, Physica C **195,** 307 (1992).

[39] M. V. Feigel'man, V. B. Geshkenbein, A. I. Larkin, and V. M. Vinokur, Phys. Rev. Lett. **63,** 2303 (1989).

[40] H. Küpfer, S. N. Gordeev, W. Jahn, R. Kresse, R. Meier-Himer, D. Wolf, A. A. Zhukov, K. Salama, and D. Lee, Phys. Rev. B **50,** 7016 (1994).

[41] G. K. Perkins and F. Cohen, Phy. Rev. B **51,** 8513 (1995).

[42] J. P. Hirth and J. Lothe, *Theory of Dislocations* (John Wiley & Sons, New York, 1982).

[43] Y. Abulafia, A. Shaulov, Y. Wolfus, R. Prozorov, L. Burlachkov, Y. Yeshurun, E. Zeldov, V. M. Vinokur, J. L. Peng, and R. L. Greene, Phys. Rev. Lett. **77,** 1596 (1996).

[44] Y. Yeshurun and A. P. Malozemoff, Phys. Rev. Lett. **60,** 2202 (1988).

[45] T. Aouaroun, V. Hardy, and C. Simon, Physica C **294,** 42 (1998).

[46] P. Chowdhury, H. J. Kim, W. N. Kang, D. J. Zang, S. I. Lee, and D. H. Kim, Phys. Rev. B **68,** 134413 (2003).

[47] M. Baziljevich, D. Giller, M. McElfresh, Y. Abulafia, Y. Radzyner, T. Schneck, T. H. Johansen, and Y. Yeshurun, Phys. Rev. B **62,** 4058 (2000).

[48] H. Küpfer, T. Wolf, R. Meier-Himer, and A. A. Zhukov, Physica C **332,** 80 (2000).

[49] T. Nishizaki, K. Shibata, M. Maki, and N. Kobayashi, J. Low Temp. Phys. **131,** 931 (2003).

[50] M. Pissas, S. Lee, A. Yamamoto, and S. Tajima, Phys. Rev. Lett **89,** 7002 (2002).

[51] M. Pissas, D. Stamopoulos, S. Lee, and S. Tajima, Phys. Rev. B **70,** 134503 (2004).

[52] T. Matsushita, E. S. Otabe, H. Wada, Y. Takahama, and H. Yamauchi, Physica C **397,** 38 (2003).

[53] H. Küpfer, T. Wolf, A. A. Zhukov, and R. Meier-Himer, Phys. Rev. B **60,** 7631 (1999).

[54] A. K. Pradhan, B. Chen, W. Ting, K. Kuroda, K. Nakao, and N. Koshizuka, Supercond. Sci. Technol. **11,** 408 (1998).

[55] V. F. Matyuk and A. A. Osipov, Russian J. Nondestructive Testing **36,** 27 (2000).

[56] A. K. Pradhan, S. B. Roy, P. Chaddah, C. Chen, and B. M. Wanklyn, Phys. Rev. B **49,** 12984 (1994).

[57] C. Dekker, P. J. M. Woltgens, R. H. Koch, B. W. Hussey, and A. Gupta, Phys. Rev. Lett. **69,** 2717 (1992).

[58] M. Fisher, P.A., Phys. Rev. Lett **62,** 1415 (1989).

[59] H. H. Wen, H. A. Radovan, F. M. Kamm, P. Ziemann, S. L. Yan, L. Fang, and M. S. Si, Phys. Rev. Lett **80,** 3859 (1998).

[60] L. I. Glazman and A. E. Koshelev, Phys. Rev. B **43,** 2835 (1991).

[61] C. A. Duran, Nature (London) **357,** 474 (1992).

[62] V. K. Vlasko-Vlasov, L. A. Dorosinskii, A. A. Polyanskii, V. I. Nikitenko, U. Welp, B. W. Veal, and G. W. Crabtree, Phys. Rev. Lett **72,** 3246 (1994).

[63] W. K. Kwok, U. Welp, G. W. Crabtree, K. G. Vandervoort, R. Hulscher, and J. Z. Liu, Phys. Rev. Lett **64,** 966 (1990).

[64] L. A. Dorosinskii, V. I. Nikitenko, A. A. Polianskii, and V. K. Vlasko-Vlasov, Physica C **219,** 81 (1994).

[65] L. A. Dorosinskii, V. I. Nikitenko, A. A. Polyanskii, and V. K. Vlasko-Vlasov, J. Mag. Mag. Mater. **140-144,** 1303 (1995).

[66] L. A. Dorosinskii, V. I. Nikitenko, A. A. Polyanskii, and V. K. Vlasko-Vlasov, Physica C **246,** 283 (1995).

[67] U. Welp, W. K. Kwok, G. W. Crabtree, K. G. Vandervoort, and J. Z. Liu, Phys. Rev. Lett **62,** 1908 (1989).

[68] W. Jiang, N.-C. Yeh, D. S. Reed, U. Kriplani, D. A. Beam, M. Konczykowaski, T. A. Tombrello, and F. Holtzberg, Phys. Rev. Lett. **72,** 550 (1994).

69 M. Konczykowaski, N. Chikumoto, V. M. Vinokur, and M. V. Feigel'man, Phys. Rev. B **51,** 3957 (1995).

70 H. Küpfer, A. A. Zhukov, A. Will, W. Jahn, R. Meier-Himer, T. Wolf, V. I. Voronkova, M. Kläser, and K. Saito, Phys. Rev. B **54,** 644 (1996).

71 T. Hwa, D. R. Nelson, and V. M. Vinokur, Phys. Rev. B **48,** 1167 (1993).

72 G. Blatter, V. B. Geshkenbein, and A. I. Larkin, Phys. Rev. Lett. **68,** 875 (1992).

73 M. Oussena, P. A. J. de Groot, K. Deligiannis, A. V. Volkozub, R. Gagnon, and L. Taillefer, Phys. Rev. Lett **76,** 2559 (1996).

74 T. Wolf, A.-C. Bornarel, H. Küpfer, R. Meier-Himer, and B. Obst, Phys. Rev. B **56,** 6308 (1997).

75 D. R. Nelson and V. M. Vinokur, Phys. Rev. B **48,** 13060 (1993).

76 A. K. Pradhan, K. Kuroda, B. Chen, and N. Koshizuka, Phys. Rev. B **58,** 9498 (1998).

77 M. Jirsa, M. R. Koblischka, T. Higuchi, and M. Murakami, Phys. Rev. B **58,** R14771 (1998).

78 A. A. Zhukov, H. Küpfer, H. Claus, H. Wühl, M. Kläser, and G. Müller-Vogt, Phys. Rev. B **52,** R9871 (1995).

79 H. Küpfer, A. A. Zhukov, A. Will, W. Jahn, R. Meier-Himer, T. Wolf, V. I. Voronkova, M. Klaser, and K. Saito, Phys. Rev. B **54,** 644 (1996).

80 M. Oussena, P. A. J. de Groot, S. J. Porter, R. Gagnon, and L. Taillefer, Phys. Rev. B **51,** 1389 (1995).

81 G. W. Crabtree, J. Z. Liu, A. Umezawa, W. K. Kwok, C. H. Sowers, S. K. Malik, B. W. Veal, D. J. Lam, M. B. Brodsky, and J. W. Downey, Phys. Rev. B **36,** 4021 (1987).

CHAPTER SIX: CONCLUDING REMARKS AND FUTURE PLAN PERSPECTIVE

6.1 $(Tl,Pb)(Sr,Ba)_2Ca_2Cu_3O_y$ Single Crystal

Magnetic *dc* measurements were performed on a sample of the high-T_c superconductor $(Tl,Pb)(Sr,Ba)_2Ca_2Cu_3O_y$. This sample was grown by the self-flux method [1,2]. The quality of the crystal was investigated with the help of X-ray diffraction (XRD) [Figure (4.3)], Scanning Electron Microscopy (SEM) [Figures (4.4) and (4.5)] and Atomic Force Microscopy (AFM) [Figures (4.6) and (4.7)]. The critical temperature, T_c, was determined using *dc* magnetic moment measurements to be 110K in a 100 Oe field parallel to the c-axis [Figure (4.8)(a)]. From these sets of measurement the quality of the sample was determined to be single phase with a high degree of crystallinity (single crystal). SEM images indicate that the growth mechanism is layer-by-layer with some irregularities between steps. From these images no spiral dislocations could be detected. From the AFM images, which have been done on a cleaved surface, the formation of structural dislocations seem possible.

From *dc* magnetization measurements a broad second magnetization peak was observed at low temperatures and for fields parallel to the *c*-axis, which is intensified and shifted to lower field with rising temperature. Heat treatment of the sample in different conditions showed that oxygen vacancies have a considerable role in critical current density; however, due to the broadness of the peak at low temperature the effect of oxygen vacancies on the shaping of the peak is not clearly conclusive. Further annealing of the sample in PbO powder showed significant progress not only in the critical current density but also in the irreversibility field. Since the irreversibility field has an inverse relation to the anisotropy of a superconductor, it seems that doping with Pb, which might be sited between the CuO_2 layers, led to the reduction of the anisotropy of the sample, and therefore the 3D structure of the sample is more reinforced. Furthermore, the substitution of Pb in the

Tl site (which is highly volatile) can be considered as a type of pinning site. From the ratio of the lower critical fields in the two principal directions the anisotropy factor was obtained to be $\Gamma^{-1} \approx 13$ which indicates a 3D lattice structure. This value of the anisotropy factor is of the same order as the one for Y(123). Of course, for a Tl(1223) family superconductor with a single Tl-O layer, the obtained value of the anisotropy factor is not far from what is expected.

The analysis of the magnetic hysteresis loops data for different temperatures and low fields using the Ertas et al.[3], Vinokur et al.[4] and Mikitik et al.[5] approaches, showed that the order-disorder transition is the source of emergence of the peak effect[6-8]. This conclusion was further reinforced by the magnetic relaxation measurements via calculating the normalized relaxation rate and the effective activation energy. From the calculation of the effective activation energy across the peak effect, the elastic to plastic crossover [9-11] was found to be the leading phenomenon in the halting of the rise of the magnetic moment and in further reducing the magnetic moment with increasing applied magnetic field.

From the relaxation data and using the two dimensional (2D) Vortex Glass scaling, it was found that no 2D scaling could describe the data, and in this way any possibility for the occurrence of dimensional crossover was ruled out.

In view of the fact that there are fewer investigation of the vortex dynamics of the Tl(1223) compounds than of the Tl(2212) and Tl(2223) compounds, it is worthwhile that this complex be investigated to a greater extent than in this research. For example, due to the technical limitations in the present work, only a small portion of the phase diagram for this complex with its fairly high irreversibility line $H_{irr}(T)$ was investigated. Thus

investigation of the vortex dynamics for fields greater than 5×10^4 Oe can shed light on the solid phase state of the phase diagram.

Furthermore, the investigation of the vortex dynamics was limited to the solid state phase of the vortex system, which makes it impossible to present even a full picture of the vortex dynamics, even within the accessible applied field range. That is, the investigation of the vortex dynamics between the irreversibility line and the upper critical field line is missing. A reliable investigation in this region can be carried out using some transport measurements, and in particular, measurements of resistivity as a function of field and temperature. By means of these types of measurements a judgement about the extent of the liquid phase and the order of the melting transition, which is claimed from the Bragg Glass phase to be a first order transition, is possible.

In addition to the above plans, the presented work in this thesis was performed only on a sample with one fixed oxygen content. Experimental results presented by Küpfer et al. [12] show that if the oxygen content of material, is changed the extent of the Bragg Glass will change, and therefore the phase diagram would alter. In this way we can obtain a deeper understanding and more extensive knowledge about the role of point disorder in creating the peak effect. Meanwhile, investigation of other alternative sources of point disorder such as Pb or other elements as promising candidates to enhance the pinning strength could be part of a potentially interesting research program which could have positive industrial consequence as well.

6.2 $Sm_{1+x}Ba_{2-x}Cu_3O_{6+y}$ (x = 0.04) Single Crystal

The top-seeded solution growth method was used to grow this single crystal in air [13]. The quality of the crystal was checked with the help of X-ray diffraction (XRD) [Figure (4.9)], Optical Light Microscopy [Figure (4.10)] and bright light Transmission Electron Microscopy (TEM) [Figure (4.11)]. From optical light microscopy, the sample was found to be highly twinned, with spacings from a few micrometers down to a few tenths of a micrometer (as small as 50-60 nm). The sample's critical temperature was measured to be 95K at a *dc*-applied field of 20 Oe [Figure (4.14)].

As a result of *dc* magnetic measurements the peak effect could be identified in this sample as well as in the Tl(1223) sample. The peak in the magnetic hysteresis loop starts from 15K, and it persists up to 85K [Figure (5.2.3)]. From the merging point of the ascending and descending branches of the hysteresis loops, on the basis of a given criterion, the irreversibly line was determined for two principal directions [Figure (5.2.2)]. The feature of the peak effect at high temperature could provide us with a guide for finding the so called lock-in angle in twinned superconductors. Meanwhile, from the measurement of the magnetic moment as a function of temperature, $m(T)$, at different applied fields the upper critical fields in the two principal direction were measured [Figure (5.2.2)], and thereby the anisotropy factor Γ^{-1} was obtained to be ~10.

From the change in the shape of the hysteresis loop on changing the sample direction relative to the applied field, a new technique was implemented for determining the lock-in angle φ_L for pinning of the vortices on extended defects, i.e. twin planes. One of the advantages of this technique is that the lock-in angle is determined without using any pre-assumed criterion for defining φ_L. As the reader may know, the common method for

finding the lock-in angle comes from the measurement of the irreversibility field as a function of angle[10]. When the direction of the applied magnetic field approaches the *c*-axis of the material a cusp like feature in the irreversibility field appears. This cusp like feature is used to determine the lock-in angle. In this method the irreversibility field is criterion dependent, and the uncertainty in the lock-in angle is relatively high.

In the present work, an appropriate scaling of the hysteresis loops for different angles close to the *c*-axis led to a clear discrimination between the two vortex dynamics regimes: one of them is governed by isotropic point disorder ($\varphi > 6°$) and the other one by the twin planes ($\varphi < 6°$) [Figure (5.2.8)]. For the angles within the lock-in angle range ($\varphi < 6°$) no peak effect occurred. The feature in Figure (5.2.8) can be used as a common technique to determine the lock-in angle for all twinned superconductors. The major advantage of this technique is that it can be done at high temperatures where the irreversibility field of a material might be accompanied by severe thermal fluctuation and determination of the irreversibility field is not feasible.

References:

1 X. L. Wang, X. M. Yang, H. W. Weber, R. Abraham, K. Lebbou, M. T. Cohen-Abad, E. Halwax, and P. Wiede, J. Cryst. Growth **167,** 93 (1996).

2 Z. X. Cheng, X. L. Wang, S. Keshavarzi, M. J. Qin, T. M. Silver, H. K. Liu, H. Kimura, and S. X. Dou, Supercond. Sci. Technol. **17,** 696 (2004).

3 D. Ertas and D. R. Nelson, Physica C **272,** 79 (1996).

4 V. M. Vinokur, B. Khaykovich, E. Zeldov, M. Konczykowaski, R. A. Doyle, and P. H. Kes, Physica C **295,** 209 (1998).

5 G. P. Mikitik and E. H. Brandt, Phys. Rev. B **64,** 184514 (2001).

6 D. Giller, Y. Abulafia, and R. Prozorov, Physica C **282,** 2209 (1997).

7 D. Giller, A. Shaulov, R. Prozorov, Y. Abulafia, Y. Wolfus, L. Burlachkov, Y. Yeshurun, E. Zeldov, V. M. Vinokur, J. L. Peng, and R. L. Greene, Phys. Rev. Lett **79,** 2542 (1997).

8 D. Giller, A. Shaulov, Y. Yeshurun, and J. Giapintzakis, Phys. Rev. B **60,** 106 (1999).

9 Y. Abulafia, A. Shaulov, Y. Wolfus, R. Prozorov, L. Burlachkov, Y. Yeshurun, E. Zeldov, V. M. Vinokur, J. L. Peng, and R. L. Greene, Phys. Rev. Lett. **77,** 1596 (1996).

10 H. Küpfer, T. Wolf, A. A. Zhukov, and R. Meier-Himer, Phys. Rev. B **60,** 7631 (1999).

11 S. Keshavarzi, M. J. Qin, X. L. Wang, H. K. Liu, and S. X. Dou, Physica C **399,** 15 (2003).

12 H. Küpfer, T. Wolf, R. Meier-Himer, and A. A. Zhukov, Physica C **332,** 80 (2000).

13 X. Yao, T. Izumi, and Y. Shiohara, Supercond. Sci. Technol. **16,** L13 (2003).

Appendix A

Magnetization for a full Critical State established in the samples indicated for different applied filed directions.

Sample Shape and field orientation M($A.m^{-1}$)

- Cylinder, diameter $2a$

_ B || axis $\frac{J_c a}{3}$

_ B ⊥ axis $\frac{4J_c a}{3\pi}$

- Infinite slab, thickness d

_ B || face $\frac{J_c d}{2}$

- Square section bar (d × d)

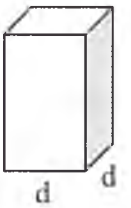

_ B || axis $\frac{J_c d}{6}$

_ B ⊥ axis $\frac{J_c d}{4}$

- Sphere, radius a

$\frac{3\pi J_c a}{32}$

- Disk, diameter $2a$, thickness d

_B ⊥ face $\frac{J_c a}{3}$

- Rectangular section bar (b × d with b > d)

$J_c d\frac{3b-d}{12b}$

Reference: Evetts, Handbook of Applied Superconductivity, iop.1999.

Appendix B

1- Hysteresis Loop

Typical sequence for measurement of a half-hysteresis loop at 20K. The highest accessible magnetic field –50000 Oe is applied first to ensure for full penetration status. The scan length is 4cm.

Set Temperature 20.000K at 10.000K/min.
Wait for Temp: Stable Delay: 600secs
Set Magnetic Field –50000.00 Oe, Hysteresis Mode,
Wait for Field Stable Delay: 10secs
Set Magnetic Field –2000.00 Oe, Hysteresis Mode,
Scan Field from –2000.00 Oe to 50000.00 Oe in 1000.00 Oe increments (53 steps) Hysteresis Mode,
Measure DC: 4.00 cm, 24pts, 2 scans, AutoRng, Long, Iterative Reg, track: No, raw: No, diag: No
End Scan
Scan Field from 50000.00 Oe to –2000.00 Oe in –1000.00 Oe increments (53 steps) Hysteresis Mode,
Measure DC: 4.00 cm, 24pts, 2 scans, AutoRng, Long, Iterative Reg, track: No, raw: No, diag: No
End Scan

2 - Relaxation

Typical sequence for measuring the decay of magnetic moment (relaxation): after zero-field cooling the sample, the highest accessible field is applied to ensure full penetration of the sample and the field is decreased to the measurement field. first points are collected in short time window (10s) due to fast decay of magnetic moment, afterward this window is increased depend on the rate of decay.

Set Temperature 100.000K at 10.000K/min
Set Magnetic Field 0.00 Oe, Oscillate, Hi Res Enabled
Wait for Temp: Stable Field: Stable Delay: 100secs
Set Temperature 10.000K at 10.000K/min
Wait for Temp: Stable Delay: 600secs
Set Magnetic Field 50000.00 Oe, Hysteresis Mode,
Wait for Field: Stable Delay: 10secs
Set Magnetic Field –40000.00 Oe, No Overshoot, Hi Res Enabled
Measure DC: 4.00 cm, 24 pts, 1scans, AutoRang, Long, Iterative Reg., track:No, raw: No, diag: No
Wait for Delay: 10 secs
Measure DC: 4.00 cm, 24 pts, 1 scans, AutoRang, Long, Iterative Reg., track:No, raw: No, diag: No
Wait for Delay: 10 secs

Measure DC: 4.00 cm, 24 pts, 1 scans, AutoRang, Long, Iterative Reg., track:No, raw: No, diag: No
Wait for Delay: 50 secs

.
.
.

Measure DC: 4.00 cm, 24 pts, 1 scans, AutoRang, Long, Iterative Reg., track:No, raw: No, diag: No
Wait for Delay: 100 secs

3 - m(T) in ZFC-FC

Typical sequence for measuring temperature dependence of magnetic moment m(T) either in applied field or without field. At first the sample is cooled down without any applied field (ZFC), after that a field of 50 Oe is applied and the data are collected. In the second part whilst a field is applied the data are collection in a cooling down process (FC).

Set Temperature 100.000K at 10.000K/min
Set Magnetic Field 0.00 Oe, Oscillate, Hi Res Enabled
Wait for Temp: Stable Field: Stable Delay: 100secs
Set Temperature 5.000K at 10.000K/min
Wait for Temp: Stable Delay: 100secs
Set Magnetic Field 50.00 Oe, No Overshoot, Hi Res Enabled
Wait for Field: Stable Delay: 10secs
Scan Temp from 5.000K to 300.0K at 0.500K/min in 0.5K increments (591 steps) Sweep
Measure DC: 4.00 cm, 24 pts, 2 scans, AutoRang, Long, Iterative Reg., track:No, raw: No, diag: No
End Scan
Scan Temp from 300.0K to 5.000K at –0.500K/min in 0.5K increments (591 steps) Sweep
Measure DC: 4.00 cm, 24 pts, 2 scans, AutoRang, Long, Iterative Reg., track:No, raw: No, diag: No
End Scan